UNIVERSITY OF CALIFORNIA, SAN DIEGO

SAN DIEGO STATE UNIVERSITY

Uptake, Localization, and Speciation of Iron and Boron in the Brown Algae *Ectocarpus siliculosus* and *Macrocystis pyrifera*

A dissertation submitted in partial satisfaction of the

requirements for the degree Doctor of Philosophy

in

Chemistry

by

Eric Paul Miller

Committee in charge:

University of California, San Diego

Professor Katja Lindenberg
Professor Arnold Rheingold

San Diego State University

Professor Carl Carrano, Chair
Professor Miriam Bennett
Professor Matthew Edwards

2015

The Dissertation of Eric Paul Miller is approved and it is acceptable in quality and form for publication on microfilm and electronically.

Chair

University of California, San Diego

San Diego State University

2015

DEDICATION

To my family

TABLE OF CONTENTS

LIST OF FIGURES

LIST OF TABLES

ACKNOWLEDGEMENTS

I would like to acknowledge the people who were instrumental to my success in the Ph.D. program. In no particular order:

My mother, for her love, encouragement, and patience.

My father, for his love, support, and pragmatism.

My stepmother, for her love, support, and enthusiasm.

My grandmother, for her love, kindness, and generosity.

Steve Barlow, for his expertise, dedication, and helpfulness.

Youxian, for his time, effort, and collaboration.

Berthold, for being such a strong mentor, both scientifically and culturally.

Frithjof, for his friendship, enthusiasm, and collaboration.

Lars for his help, training, and hospitality.

Hendrik, for his knowledge, expertise, and friendship.

Volker, for his hospitality, kindness, and brilliant work.

Leeroy for his instruction, troubleshooting, and patience.

Professor Peter van der Geer, for inspiring me and his recommendation for the graduate program.

Professor Dave Pullman for his training, suggestions, and assistance with Raman microscopy.

Professor Matt Edwards for his collaboration, kelp harvesting, and culturing assistance.

Breckie, for help with harvesting kelp and motivating me to SCUBA dive.

Christian, for his collaboration and travel companionship.

The Barbeau group for inviting me to conduct research in their laboratory

My lab mates Teresa T., Kyoko Y., Ryan B., Ryan F., Ashtian H., Chris T., Geri P., Jerrell T., Jennifer G., and Nicole D. It was a pleasure working with all of you.

My colleagues and friends Caline, Jenny, Patrick, Nobu, Bob, Brent, Jayneil, Josh, Eric, Haley, David, Arielle, Theresa, Simon, Chris, and John.

To my collaborators whom I have not met in person: Professor Al Crumbliss, Wolfram, and Aruna.

Mary for creating an organized, efficient, and extremely pleasant work environment.

Professor Carl Carrano for his support as my PhD advisor. Through your outstanding mentorship, I was able to reach my full potential as a scholar and researcher. I am eternally grateful to you for making my graduate experience one that I will always remember fondly.

Chapter I, in part, is a reprint of the material as it appears in the Journal of Experimental Botany, 2012, Böttger, Lars H.; Miller, Eric P.; Andresen, Christian; Matzanke, Berthold F.; Küpper, Frithjof C.; Carrano, Carl J. The dissertation author was the second author of this paper.

Chapter I, in part, is a reprint of the material as it appears in the Journal of Experimental Botany, 2014, Miller, Eric P.; Böttger, Lars H.; Weerasinghe, Aruna J.; Crumbliss, Alvin L.; Matzanke, Berthold F.; Meyer-Klaucke, Wolfram; Küpper, Frithjof C.; Carrano, Carl J. The dissertation author was the primary investigator and author of this paper.

Chapter II, in full, has been submitted for publication of the material as it may appear in New Phytologist, 2015, Miller, Eric P.; Wu, Youxian; Carrano, Carl J. The dissertation author was the primary investigator and author of this paper.

VITA

Education

2015	Ph.D., Chemistry,University of California, San Diego, CA/ San Diego State University, CA
2015	M.A., Chemistry, San Diego State University, CA
2001	B.S., Bioengineering, Arizona State University, Tempe, AZ

Awards

2015	CSU COAST Graduate Student Research Scholarship
2014	Harry E. Hamber Memorial Scholarship
2013	Paul G. and Margaret F. Peninger Memorial Scholarship
2013	Brenda and Dave Rickey Foundation Study Abroad Scholarship
2010	Associated Students Graduate Student Travel Scholarship

Publications

Miller, E.P., Wu, Y., and Carrano, C.J. Boron uptake, localization, and speciation in marine brown algae. (Submitted 2015) *New Phytologist*.

Miller, E., Böttger, L., et al. (2014). Surface bound iron: A metal ion buffer in the marine brown alga *Ectocarpus siliculosus*. *J. Exp. Bot.* 65. 585-594.

Böttger, L., Miller, E., et al. (2012). Atypical iron storage in marine brown algae: A multidisciplinary study of iron transport and storage in *Ectocarpus siliculosus*. *J. Exp. Bot*.63.5763-5772.

ABSTRACT OF THE DISSERTATION

Uptake, Localization, and Speciation of Iron and Boron in the Brown Algae *Ectocarpus siliculosus* and *Macrocystis pyrifera*

by

Eric Paul Miller

Doctor of Philosophy in Chemistry

University of California, San Diego, 2015

San Diego State University, 2015

Professor Carl Carrano, Chair

This work is divided into two parts: (I) cell surface binding, uptake, and storage of iron in brown algae, and (II) boron uptake, localization, and speciation in brown algae.

Iron is an essential element for all living organisms due to its ubiquitous role in redox and other enzymes, especially in the context of respiration and photosynthesis. Although the iron uptake and storage mechanisms of terrestrial/higher plants have been well-studied, the corresponding systems in marine algae have received far less attention. Chapter I focuses on these mechanisms in two brown seaweeds: *Ectocarpus siliculosus* and *Macrocystis pyrifera.* Through the course of experiments, it was found that a

significant amount of iron was bound extracellularly. While this phenomenon is widely recognized and has prompted the development of experimental protocols to eliminate its contribution to iron uptake studies, its potential biological significance as a concentrated iron source for marine algae is only now being recognized. In this study, using an interdisciplinary array of techniques, we explore the nature of the extensive and powerful iron binding on the surface of both laboratory and environmental samples of *Ectocarpus* and *Macrocystis.* We propose that the surface binding properties of *Ectocarpus* and *Macrocystis* allow it to function as a quasi-biological metal ion "buffer" facilitating iron uptake under the widely varying external iron concentrations found in coastal marine environments. Short-term radiolabeled iron uptake studies verified that iron is taken up in a time- and concentration-dependent manner consistent with an active transport process. Using a combination of Mössbauer and XAS spectroscopies, a mineral core has been identified as the likely storage form. Genomic and microscopic analyses indicate that this iron store is more likely vacuolar-based than of protein origin.

In chapter II, I describe boron uptake, speciation, localization and possible biological function in *Macrocystis* and *Ectocarpus*. In contrast to the generally boron-poor terrestrial environment, the concentration of boron in the marine environment is relatively high (0.4 mM) and while there has been extensive interest in its use as a surrogate of pH in paleoclimate studies in the context of climate change-related questions, the relatively depth independent, and the generally non-nutrient-like concentration profile of this element have led to boron being neglected as a potentially biologically relevant element in the ocean. Results herein indicate that boron is taken up by a facilitated diffusion mechanism against a considerable concentration gradient.

Furthermore, in both *Ectocarpus* and *Macrocystis* some boron is most likely bound to the cell wall constituent alginate and the photoassimilate mannitol located in sieve cells. These results indicate possible biological roles for boron as an osmoprotectant and/or metabolite transporter.

I. Cell Surface Binding, Uptake, and Storage of Iron in Brown Algae

I.1. Introduction

Iron is an essential element for all living organisms due to its ubiquitous role in redox and other enzymes, especially in the context of respiration and photosynthesis. The iron uptake and storage systems of terrestrial/higher plants are now reasonably well understood with two basic strategies for iron uptake being distinguished: Strategy I plants, mainly dicotyledons, use a mechanism involving soil acidification and induction of Fe(III)-chelate reductase (ferrireductase) and Fe(II) transporter proteins (Moog and Bruggemann, 1994; Robinson et al., 1999). Strategy II plants (in particular, monocotyledons/grasses) have evolved sophisticated systems, similar to those of bacteria and fungi, based on high-affinity, iron specific, binding compounds called phytosiderophores (Romheld and Marschner, 1986).

In contrast, there is little knowledge about the corresponding systems in marine, plant-like lineages; particularly the multicellular macroalgae (seaweeds). This is important as the iron level in ocean waters is even lower than in most terrestrial environments due both to the low solubility of Fe(III) in oxic seawater and the fact that a large fraction of the limited iron available is already tightly complexed (Bruland et al., 1991). Indeed, iron availability is now well known to limit primary productivity in certain oceanic regimes (Martin and Fitzwater, 1988). While there is some evidence that marine algae produce siderophore-like molecules (Trick et al., 1983; Naito et al., 2001), as of this date, not a single extracellular metal chelator produced by eukaryotic algae has been characterized, and ambiguity remains about whether the siderophore-like molecules

purported to be isolated from cultures of eukaryotic algae are actually produced by the algae themselves or by associated bacteria.

While it seems likely that the iron many marine algae take up from the environment, irrespective of its detailed internalization mechanism, arrives at the cell surface by diffusion, there is growing evidence for more "active" means of concentrating this element prior to uptake. It has been well established in both laboratory and environmentally derived samples, that a large amount of iron can be "non-specifically" adsorbed to the surface of marine algae (Hutchins et al., 1999). This surface bound iron may derive from simple electrostatic attraction between colloidal iron hydroxide particles and the cell surface, from de novo precipitation of iron hydroxo polymers from equilibrium solutions at the cell surface due to the increased surface pH relative to bulk seawater, or possibly from other mechanisms (Milligan et al., 2009). While this surface adsorption phenomenon is widely recognized and has prompted the development of experimental protocols to eliminate its contribution to iron uptake studies, its potential exploitation as a concentrated iron source for marine algae is only now being recognized (Hudson and Morel, 1989; Tovar-Sanchez et al., 2003). The extraordinary swarming behavior of the related cyanobacterium *Trichodesmium* when confronted with particulate, iron-containing dust, is a spectacular example of active surface concentration of iron prior to actual uptake (Rubin et al., 2011). More recent examples of possible surface concentration of iron come from the diatoms, the Alveolate *Chromera velia*, and others where in some cases there is evidence that the surface bound iron is ultimately internalized (Sutak et al., 2010; Sutak et al., 2012; Sutak et al., 2012).

Since the cell wall of the brown algae is largely composed of anionic alginate

polysaccharides, which account for 20 – 40% of their dry mass (Mabeau, 1987), it is scarcely surprising that the surface of these organisms should have considerable metal binding properties. Sulfated polysaccharides are another structural polymer common to brown algae with metal-binding anionic functional groups. Indeed, brown algae have been widely discussed for their potential in heavy metal biosorption applications (Davis et al., 2003). In laboratory studies, rigorous washing procedures have been described to eliminate this "artifact" of non-specifically adsorbed iron on the cell surface. However, one must acknowledge the possibility of a biological function given the strength of this iron adsorption phenomena. The characterization of this cell surface binding of iron by brown algae is one investigation comprising this body of work.

While efficient transport mechanisms for iron uptake are an essential element in all pro- and eukaryotic cells, its intracellular availability and storage has to be tightly regulated, not only to buffer supply and demand, but also to prevent cell damage from undesirable reactions of free radicals, formed catalytically by free Fe ions. Ferritin represents the most common form of iron storage in all domains of life. This water-soluble protein is composed of a tetraeicosameric shell built up by polypeptide subunits and a microcrystalline core of ferrihydrite within the protein cavity. A general structural model of ferritins has been derived from X-ray diffraction studies (Ford et al., 1984; Harrison and Lilley, 1989; Lawson et al., 1991; Frolow et al., 1994; Trikha et al., 1994). Although the general topology of most ferritins is similar, a remarkable heterogeneity of the ferritin subunits is observed which is the basis of different classes of ferritins including various types of bacterial ferritins *i.e.* heme containing bacterioferritins (Bfr), non-heme bacterial ferritins Ftn1 and Ftn2, "miniferritins" (exhibiting a dodecahedral

peptide assembly), and various animal and plant "maxiferritins". Numerous functions have been attributed to these ferritins. One function is associated with "true" iron storage. Under iron-rich growth conditions the metal is accumulated in order to provide an iron pool sufficiently high to prevent growth limitation effects in an iron-deficient environment. A second function is associated with the potentially harmful role iron can play in cell physiology by generating $OH^{\bullet}$ and other oxygen radicals (Haber-Weiss-Fenton reaction cycle (Winkelmann and Carrano, 1997). These oxygen radicals and in particular OH* may cause cellular oxidative damage and therefore participate in ageing processes and carcinogenesis (Halliwell and Gutteridge, 2007). A role for ferritin against oxidative stress has been shown in *Arabidopsis thaliania* (Ravet et al., 2009).

Brown algae (Phaeophyta) belong to a lineage that has been evolving independently of other major photosynthetic lineages, such as green plants (Chlorophyta) and red algae (Rhodophyta). Instead, they are classified within the Stramenopiles and Chromalveolates together with diatoms, golden-brown algae and oomycetes (Baldauf, 2003). As a consequence of this singular evolutionary history, brown algae exhibit many unusual, and often unique, features. These features are adaptations to the marine coastal environments in which brown algae are usually the dominant organisms in terms of biomass, especially in terms of the extensive kelp forests. Other types of brown algae (ie. filamentous seaweeds) are closely related to kelp but morphologically distinct. Their minimally differentiated tissue offer many research opportunities and thus serve as a model for highly evolved seaweeds such as giant kelp.

The key role of brown algae, effectively constituting an interface between the ocean, the atmosphere and land masses, in the biogeochemical cycle of halogens is well

established (Küpper et al., 2008). However, the role of trace metals in brown algal-dominated ecosystems is poorly understood (as is brown algal trace metal metabolism), contrasting with the intense research interest which pelagic systems have received. This lack of knowledge is surprising in view of the fact that the industrial exploitation of brown algae is expanding partially due to interest in their use for production of alginate, fucans etc., but increasingly for their potential as biofuel where they have the advantage of high productivity without competing with terrestrial crops for farmland. *Ectocarpus* is a filamentous brown alga with a worldwide distribution along temperate coastlines, and is a nuisance as a "fouling" organism on many man-made surfaces in the sea. It has some significant advantages as an experimental model and constitutes one of the best-studied seaweeds (Peters et al., 2004; Charrier et al., 2008). It can easily be cultivated in small volumes of seawater media both axenically and with associated bacteria, its entire, well-known life cycle can be completed within a few months in culture (Müller et al., 2008), and many molecular tools are available, including mutant collections, microarrays and proteomics data. It has also recently become the first seaweed of which the entire genome has been sequenced and thus offers unprecedented opportunities for study (Cock et al., 2010).

While modern spectroscopic techniques such as Mössbauer and X-ray absorption spectroscopy (XAS) have played a major role in our understanding of iron uptake and storage in many terrestrial microorganisms (Winkler et al., 1994; Sch?nemann and Winkler, 2000), they have been little utilized in marine algal systems. Such spectroscopic techniques are powerful, non-invasive tools for the determination of both the *in vivo* redox, spin state and coordination environment of iron, as well as for isolated biological

(macro)molecules. Transmission Mössbauer spectroscopy (TMS) is valuable as it is specific for ^{57}Fe and thus no other transition metal obscures the experimental results. Due to the low natural abundance of the isotope (2%), ^{57}Fe-enrichment is essential for almost any biological sample. This potential disadvantage, however, can be successfully exploited for iron uptake analyses since a sample prior to uptake typically exhibits ^{57}Fe in quantities below the detection limit of conventional Mössbauer spectroscopy. Thus only labelled newly acquired Fe is visible. XAS confirms and broadens the information obtained by Mössbauer. From XANES the average oxidation state of the metal center and the metal ligand coordination geometry can be derived. EXAFS analysis provides metal ligand bond distances at a high accuracy (±0.02 Å), metal-ligand type and coordination number of the complex (albeit with lower accuracy, i.e. error bars of at least ±0.5). Herein, the first ever study of the iron uptake, surface-binding, and storage mechanisms in the brown alga *Ectocarpus* is reported using such spectroscopic techniques in concert with more conventional radio-labeled uptake studies. Previous studies have shown that *Macrocystis* acquires iron through a Strategy I cell surface reductase mechanism. However, knowledge is lacking as to the affinity of the cell surface for binding iron. In this chapter, cell surface binding and storage of *Macrocystis* are investigated using a parallel methodology when available and feasible.

I.2. Cell Surface Binding, Uptake, and Storage of Iron in *Ectocarpus siliculosus*

I.2.1. Cell Surface Binding

I.2.1.1. Results

I.2.1.1.1. Kinetics and thermodynamics of surface-bound iron

Previous studies indicate that iron is internalized by *Ectocarpus* from FeEDTA in a time- and concentration-dependent manner with the soluble Fe(III) species known as Fe(III)' as the likely biological substrate as opposed to the intact Fe(III)-EDTA complex (see Section I.2.2). Internal iron was determinable only after extensive washing of the cells with the Ti(III)-citrate-EDTA (see section I.4 for reagent preparation details) reagent described by Hudson and Morel (Hudson and Morel, 1989), as unwashed cells were found to bind a large amount of iron but in a time independent manner indicative of rapid surface binding (Fig. I.2.1.1). The amount of surface binding as compared to internalization was at least a hundred fold higher.

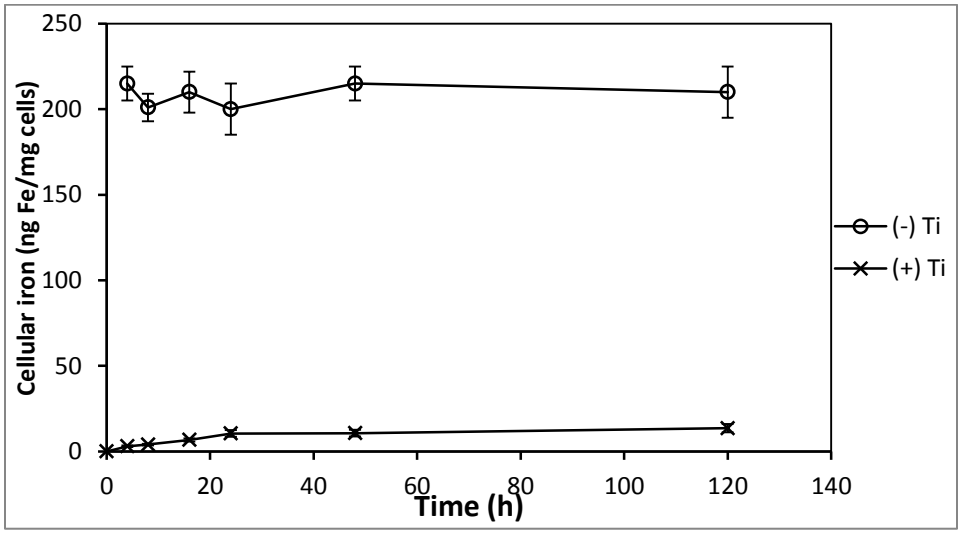

Figure I.2.1.1. Uptake of ^{55}Fe by *Ectocarpus*. Incubation in 30 µM $^{55/56}$FeEDTA as a function of time in samples washed or not washed in Ti(III)-citrate-EDTA reagent. Data are mean ± standard deviation of triplicate measurements.

While this surface binding of iron was not unexpected, it was initially dismissed as nonspecific and an experimental nuisance. However upon further examination it was found that the high level of surface binding persisted even when the iron in the growth media was presented in the form of highly stable EDTA or other chelates, inconsistent with weak nonspecific binding. Indeed surface binding was not eliminated until the EDTA to Fe concentration approached 100:1 indicating that the stability of the Fe-surface interaction had to be greater than that of Fe-EDTA itself (Fig. 1.2.1.2). Measuring the surface binding from a solution of fixed [^{55}Fe] (1 µM) as a

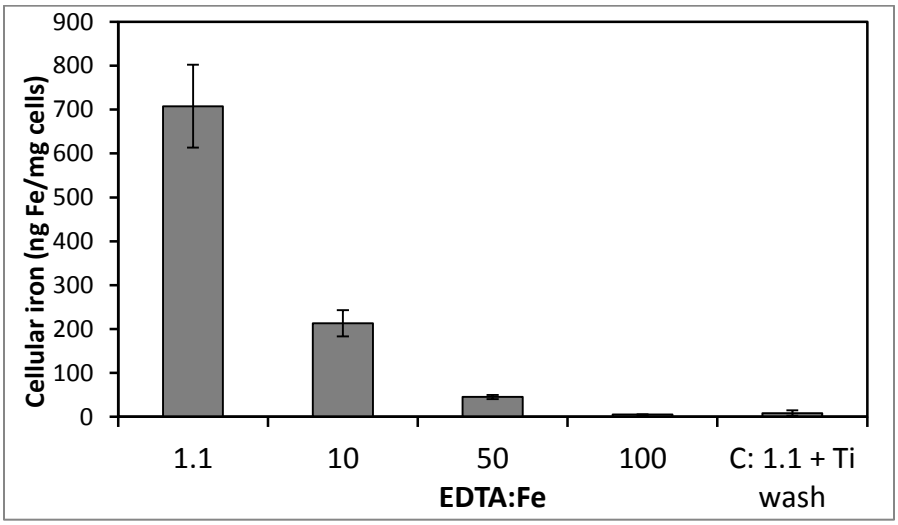

Figure I.2.1.2. *Ectocarpus* cellular surface-bound ^{55}Fe as a function of excess EDTA in the media containing 30 µM Fe(III). Error bars are mean ± standard deviation of triplicate measurements.

function of [EDTA] and pH allowed us to estimate an effective surface binding constant K'_{eff}. The values obtained were relatively constant (K'_{eff} = 3 – 29 x 10^{21} M^{-1}) over a wide range (33 – 1500 µM) of excess EDTA, confirming a uniform binding and the

reliability of the data set. At high pH (8.6 – 8.8), iron binding is very strong (log K'_{eff} = 21 – 22) while at acidic pH (4.8) the binding constant is drastically reduced (log K'_{eff} = 14) presumably due to protonation of the alginate carboxylate groups thought to be the major iron binding moieties (*vide infra*).

While it was clear that iron binds to the surface of *Ectocarpus* with high thermodynamic stability, its kinetic stability was undetermined. ^{55}Fe pulse experiments were thus conducted to investigate the effect on uptake after initial binding at the cell surface. Pulse-labeling the cell surface with ^{55}Fe followed by replacement of the media with "iron free" media (oligotrophic open ocean water with a sub-nM concentration of iron) showed that approximately 50% of the surface-bound iron quickly reenters solution while intracellular iron continued to increase with time (Fig I.2.1.3). However, ambiguity

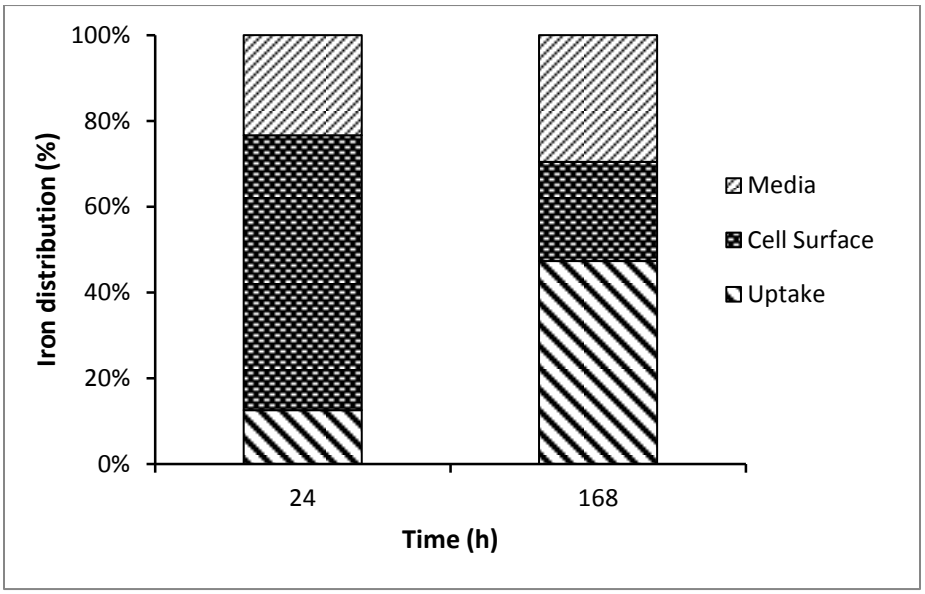

Figure I.2.1.3. Distribution of ^{55}Fe after exposure of *Ectocarpus* to a 30 µM solution of EDTA for 6 hours, followed by resuspension of cells in iron-free media for either 24 or 168 hours. Cell-surface iron represents the difference between samples before (total Fe) and after washing (internalized Fe) with the Ti(III)-citrate-EDTA reagent. Data represent mean of three determinations.

remains as to whether the increasing intracellular iron derives directly from the surface-bound iron or from surface bound iron that re-entered the solution before being taken up. The latter possibility was tested by a pulse-chase experiment in which an initial ^{55}FeEDTA pulse was followed by a chase of "cold" ^{56}FeEDTA. Continued ^{55}Fe uptake following the ^{56}Fe chase would suggest that the Fe^{3+} taken up (internalized) is bound very tightly to the surface, and does not reenter the solution (and hence is unaffected by isotopic dilution). This, however, is not the case as can be seen in Figures I.2.1.4 and I.2.1.5 for Ti(III) washed and unwashed samples respectively. The complete cessation of ^{55}Fe uptake upon isotopic dilution implies that surface bound iron is not internalized directly; rather it reenters the bulk solution.

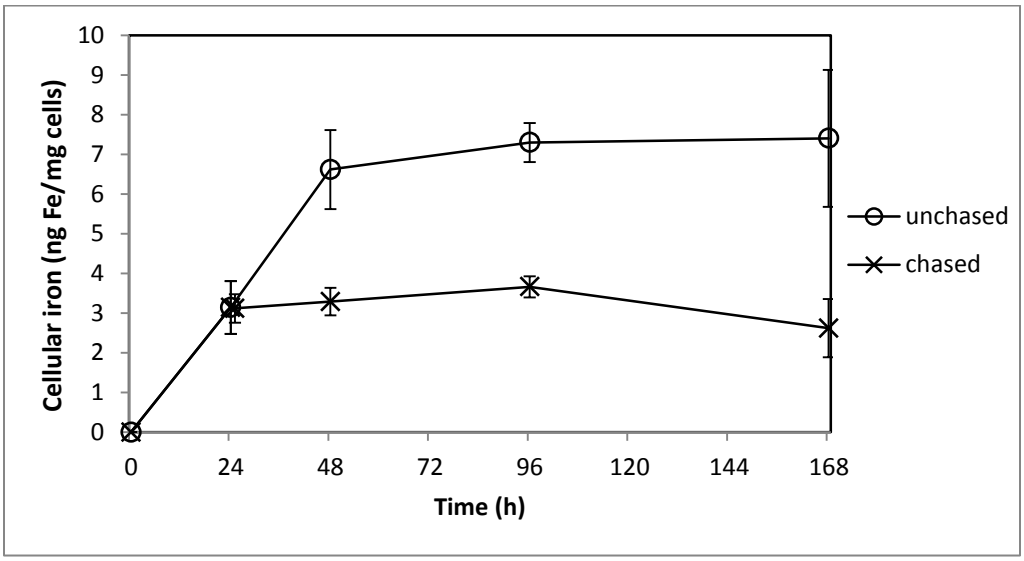

Figure I.2.1.4. ^{55}Fe pulse-chase experiment with Ti(III) wash. ^{55}Fe uptake (internalized Fe) after washing with Ti(III) reagent as a function of time by *Ectocarpus* treated with 30 µM ^{55}FeEDTA or following a chase of 30 µM ^{56}FeEDTA. The chase was added at the 24 hr time point. Data are mean ± standard deviation of triplicate measurements.

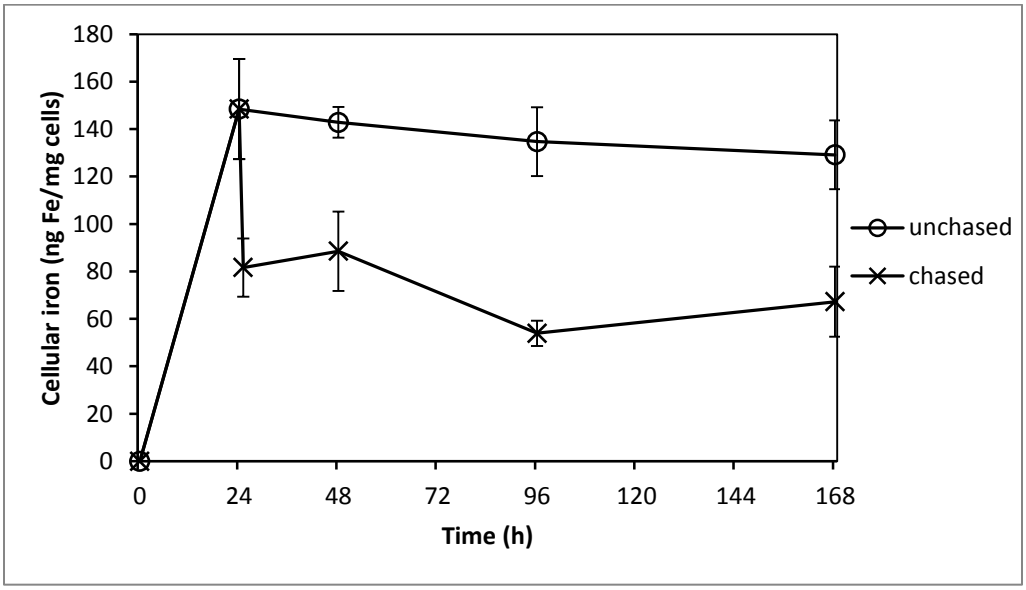

Figure I.2.1.5. ^{55}Fe pulse-chase experiment without Ti(III) wash. Total cellular iron as a function of time by *Ectocarpus* treated with 30 µM ^{55}FeEDTA or following a chase of 30 µM ^{56}FeEDTA. The chase was added at the 24 hr time point. Data are mean ± standard deviation of triplicate measurements.

I.2.1.1.2. Localization of iron on the surface

Microscopic analyses were performed on environmental samples to investigate the spatial distribution and uniformity of iron bound to the cell surface. The iron-specific stain ferrocyanide was lacking in intensity for optical microscopic analysis so the enhancing agent 3,3-diaminobenzidine (DAB) was used in conjunction with ferrocyanide (see section 1.2.1.2.6). This proved effective for detecting extracellular as well as intracellular iron (Fig. I.2.1.6). It is clear that the majority of the iron in samples not washed with the Ti(III)-citrate-EDTA reagent is present on the surface with internal iron

only visible in washed samples.

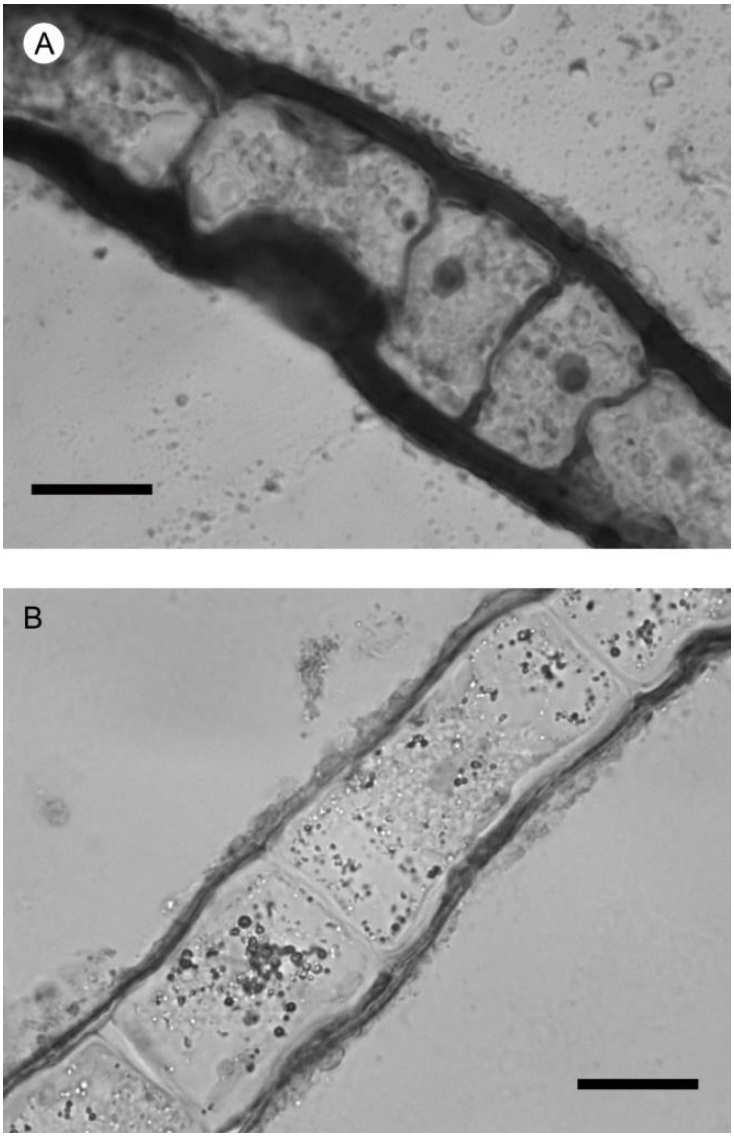

Figure I.2.1.6. Light micrographs of *Ectocarpus* stained with the ferrocyanide-DAB procedure. (A) Environmental *Ectocarpus* sample without Ti(III)-citrate-EDTA wash. (B) Long-term laboratory Ectocarpus sample grown on iron-enriched culture medium followed by Ti(III)-citrate-EDTA wash. Dark areas indicate high concentrations of iron. Bars, 10 µm).

The preponderance of surface bound iron in unwashed samples is corroborated by energy dispersive X-ray spectroscopy (EDS). Figure 2.7A depicts a scanning electron

micrograph of an *Ectocarpus* cell alongside the corresponding EDS spectrum at transect point C located on the cell wall (Fig. I.2.1.7C).

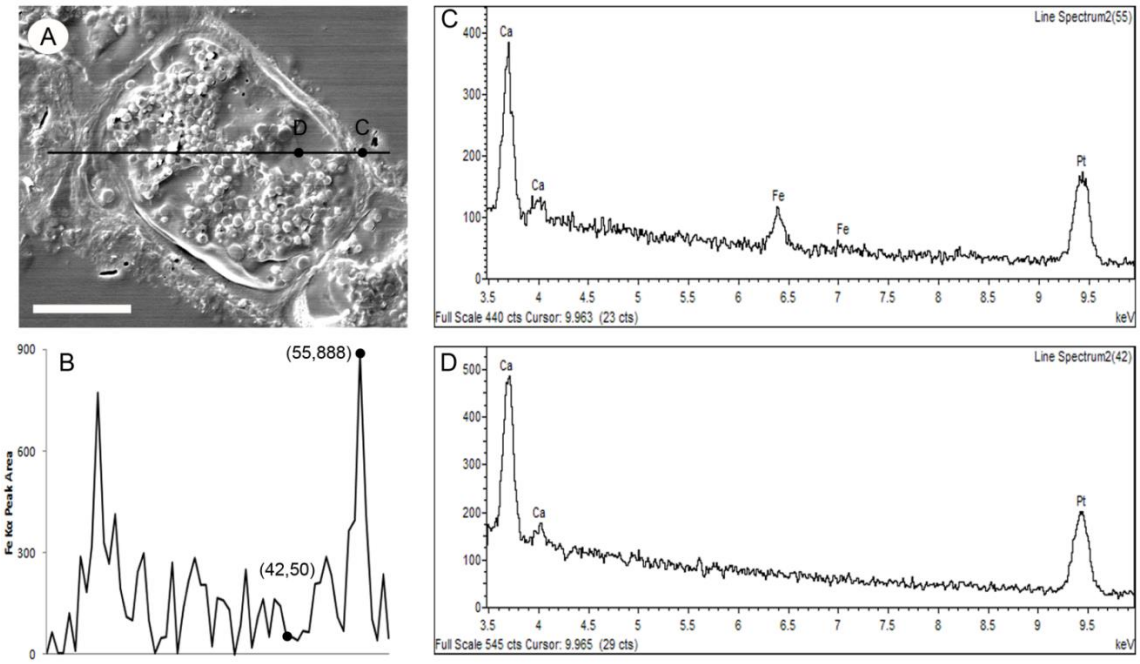

Figure I.2.1.7. SEM and EDS of *Ectocarpus*. (A) Scanning electron micrograph of environmental *Ectocarpus* sample without Ti(III)-citrate-EDTA wash: black line depicts the transect for EDS with two points. (C and D) selected for accompanied spectra (white bar, 10 µm). (B) Fe K_α peak areas of 60 points along the full transect, scaled to fit the line in (A). (C and D) Energy-dispersive spectra of points C and D from the transect in (A).

I.2.1.1.3. Nature of the surface bound iron

Transmission Mössbauer spectroscopy (TMS) and X-ray absorbance spectroscopy (XAS) were used to determine more precise details of the surface iron and its surrounding ligands. The TMS spectra of a sample of *Ectocarpus* grown for 48 hr exposed to 30 µM ^{57}FeEDTA and either washed with Ti(III)-citrate-EDTA reagent or unwashed can be seen in Figures I.2.1.8B and I.2.1.8A respectively. Essentially no signal is detectable in the

washed sample indicating that, as expected (Böttger et al., 2012), the amount of iron internalized after short term incubation is below the TMS detection limit. Therefore the entire signal seen in the unwashed sample represents external or surface bound iron.

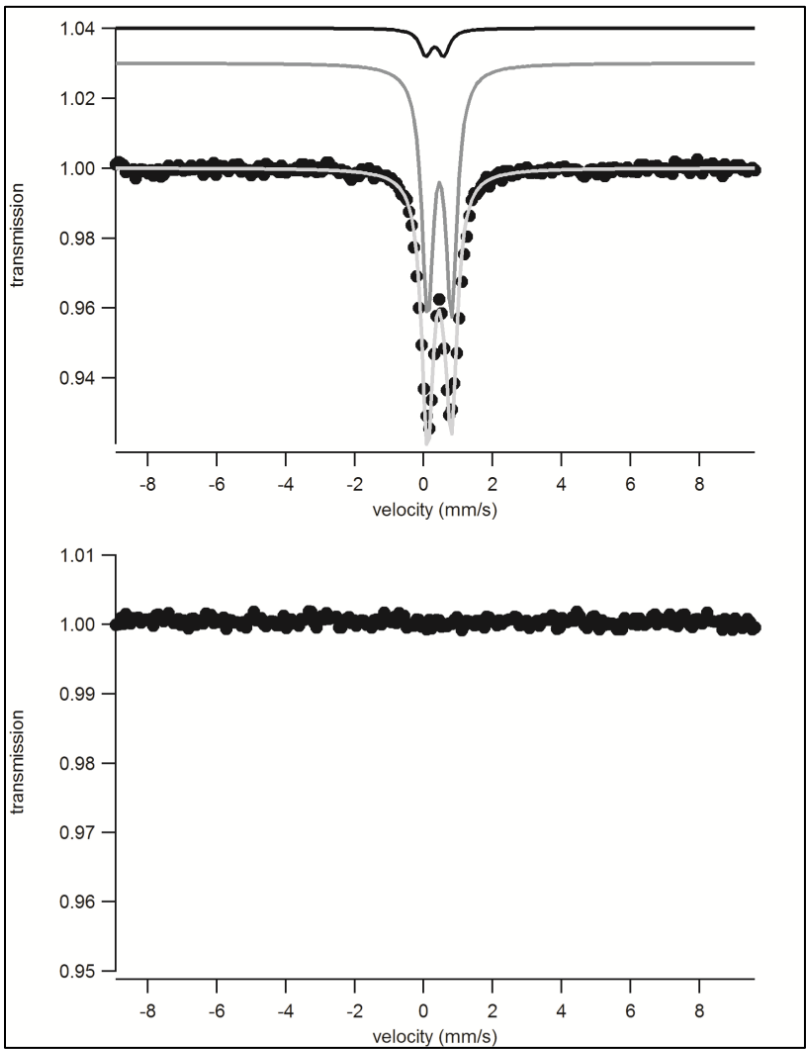

Figure I.2.1.8. TMS at 77 K of samples of *Ectocarpus* grown (A) before and (B) after washing with Ti(III)-citrate-EDTA. Dots: experimental data; dark grey line: Fe-carboxylate species; black line: unknown species; light grey line: overall fit to the data using the parameters in Table I.2.1.

The data for the unwashed sample can be fitted (Fig. I.2.1.8.A) with two doublets exhibiting the parameters shown in Table I.2.1. The main component (c2a + c2b) has

parameters which are typical for polymeric Fe(III) octahedrally coordinated to primarily oxygen ligands and fit into the range observed for carboxylate Fe(III) model complexes (Dziobkowski et al., 1981). The second and very minor component (~10% of total area) exhibits parameters which belong to an as yet unknown species. The parameters obtained for the major component are similar to, but distinct from ($\Delta\delta = 0.05$ mms^{-1} and different relaxation behavior, see below) those calculated for the major component of the internalized iron seen upon long term exposure (see Section I.2.3.1).

Table I.2.1. Parameters used to fit the TMS of *Ectocarpus* grown for 48 hrs on 30 µM ^{57}FeEDTA at various temperatures.

Temperature (K)	Component	δ (mm s^{-1})	ΔEq (mm s^{-1})	B_{hf}	Relative area (%)
77	c1	0.32	0.52	–	~10
	c2a	0.46	0.69	–	~90
	c2b	–	–	–	–
4.2	c1	0.34	0.52	–	~10
	c2a	0.49	0.65	–	~35
	c2b	0.49	0	44.7	~55
1.8	c1	0.34	0.52	–	~12
	c2a	0.49	0.65	–	~20
	c2b	0.49	0	45.4	~68

The most significant difference is in the blocking temperature (Mørup, 2011) obtained from the temperature dependence of the TMS spectrum (Fig. I.2.1.9) which is above 4.2K for the surface bound iron as compared to below 1.8K for that internalized. In the case of mineral species this behavior would normally suggest either a more crystalline structure and/or larger particle sizes.

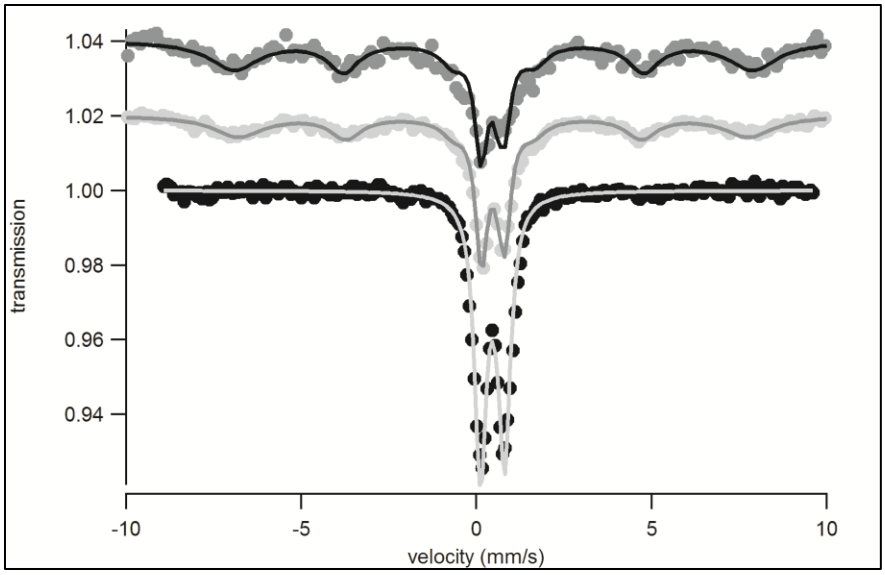

Figure I.2.1.9. TMS of unwashed *Ectocarpus* at different temperatures. Black dots: 1.8 K; light grey dots: 4.2 K; dark grey dots: 77 K; solid lines: fits to the data using parameters from Table II.1.

In addition to TMS, we employed extended X-ray absorption fine structure (EXAFS) spectroscopy to probe the chemical nature of the external iron. The EXAFS spectrum for an unwashed sample of *Ectocarpus* is shown in Figure I.2.1.10. Based on the above Mössbauer data, the presence of a superparamagnetic polymeric Fe^{3+}-oxo system was indicated.

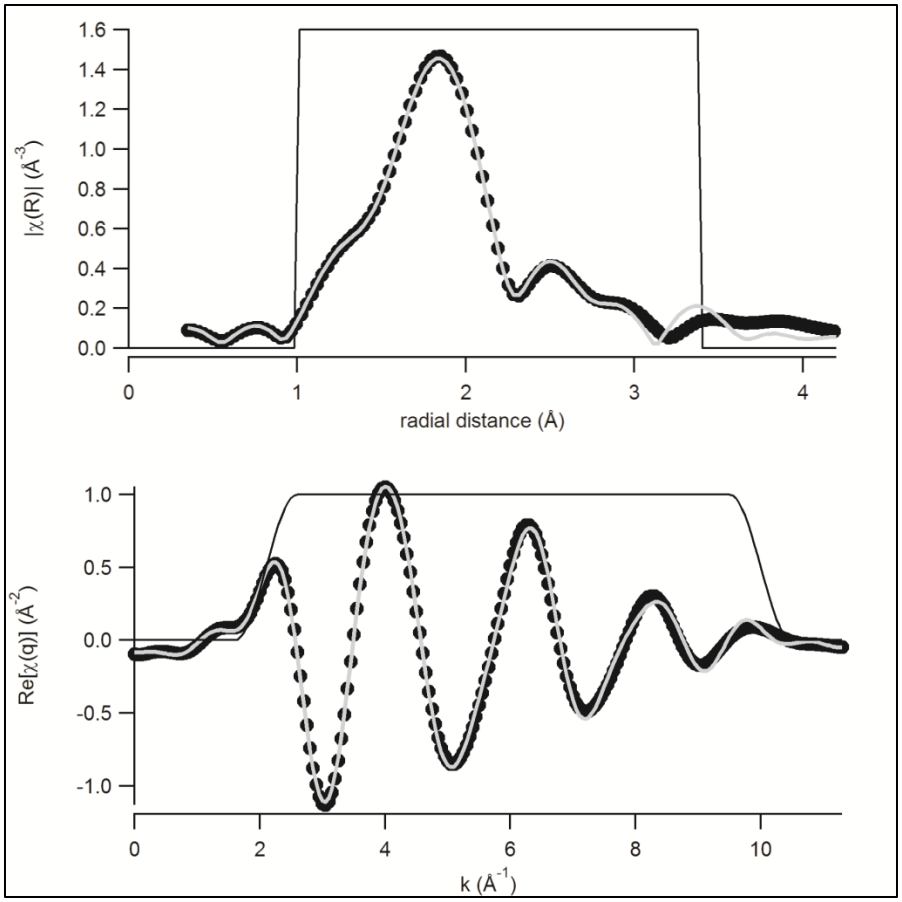

Figure I.2.1.10. EXAFS spectra of *Ectocarpus*. Top: R-space; Bottom: q-space. Black dots: experimental data; light grey lines: fits to the data; black lines: Hanning-type windows.

Within this constraint, various models were tested. Speciation models were constructed and coordinates obtained after molecular mechanics energy minimization using the program Chem 3D. These coordinates were then used as input to the FEFF program to obtain the scattering paths. The best fits came from a hydroxo-carboxylato model (Fig. I.2.1.11; see Methods I.2.2.9 for scattering paths used).

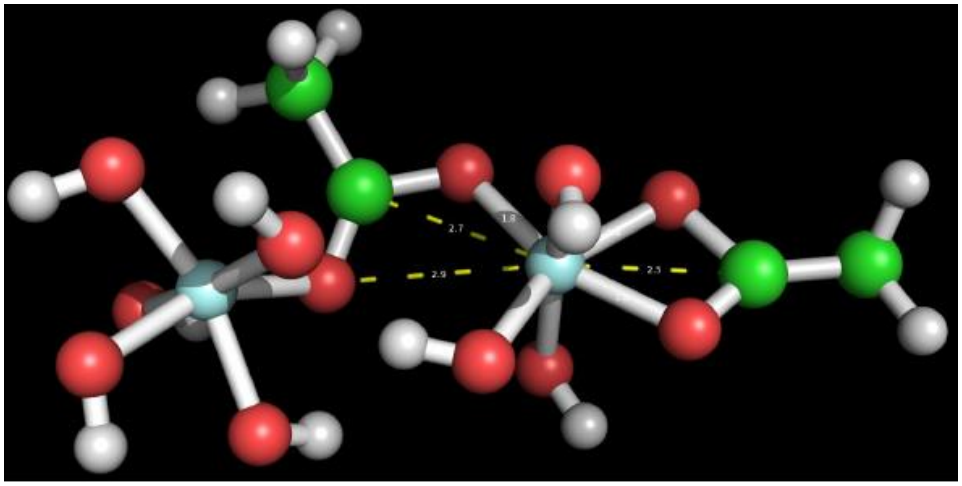

Figure I.2.1.11. EXAFS *Ectocarpus* cell surface iron bonding model.

The final fit of the EXAFS spectrum (Fig. II.2.10) to the model was very good where there are 3.4±0.8 bridging carboxylate groups Fe-O-C-[COR] present with bond distances of Fe-O of 1.99 Å (n=4.2 ±0.6), Fe-[O]-C of 2.68 Å (n=3.3±1.2), Fe-[O-C]-O of 2.90 Å (n=2.6±0.9) and 0.9±0.4 OH groups with an Fe-O bond distance of 1.81 Å. Overall, the EXAFS fit data are completely consistent with that obtained by TMS.

I.2.1.2. Discussion

Until recently, adsorption of iron to the cell surface of marine algae has been viewed as an experimental artifact complicating uptake studies. While it is indeed necessary to remove this signal when quantifying uptake, the potential biological significance of this surface bound iron has generally been ignored. Such was the case in *Ectocarpus* (Böttger et al., 2012). However, in the process of reexamining the data we were intrigued by the fact that a high level of surface binding was occurring despite the fact that all the iron present in the media was in the form of the very stable FeEDTA

chelate. Indeed surface binding persisted even when an excess of EDTA was present. Thus it appeared that the binding of iron to the surface of *Ectocarpus* is far stronger than that expected for a weak nonspecific electrostatic interaction and thus might have some biological significance. This possibility is supported by our estimate of the effective surface binding constant (K'_{eff}) for Fe(III)′ of between 3 – 29 x 10^{21} $M^{-1,}$ comparable to the affinity of EDTA′ for Fe(III)′ at pH 8.7 (see Table I.2.5). The magnitude of the drop in affinity with decreasing pH is also comparable to that observed for EDTA, which is a polycarboxylic acid and is thus consistent with the binding of iron to the cell surface of *Ectocarpus* primarily by the carboxylate groups found in alginate which is the major cell wall component in this class of organism. Histological staining and energy dispersive X-ray spectroscopy (EDS) of both environmental and laboratory derived samples of *Ectocarpus* confirms the spatial uniformity and primarily surface binding of iron, as would be expected of a constitutive scaffold such as the cell wall. While the numerous subgroups and variable side chains of these components present a challenge for the identification of the specific iron-binding site(s) we have used a combination of TMS and EXAFS spectroscopic studies to enable the determination of iron oxidation state, geometry and ligation in the first and second coordination spheres. The results are entirely consistent with octahedral hydroxo-carboxylato ligation of the iron.

Finally, the question remains: what is the biological significance (if any) of this strong surface binding of iron? While open ocean dissolved iron concentrations are virtually always extremely low (sub-nM), concentrations of this element in coastal regimes are far more variable and range from 0.1-300 nM (Chase et al., 2002). Thus, organisms in coastal ecosystems have to contend with an inherently different set of

acquisition problems as compared with organisms in oligotrophic open ocean environments. Surface binding of iron could serve as a metal ion buffer to assure organisms like *Ectocarpus* of an adequate supply of iron for metabolic needs in the face of widely varying external concentrations of the element. In times of plenty the equilibrium would strongly favor iron bound to the surface while in times of deprivation the equilibrium would shift to dissociation of the surface bound iron into solution. Our overall proposed mechanism for iron uptake in *Ectocarpus* based on the data presented here and in Böttger et al., 2012 is shown in Figure 1.2.1.12.

Since our data most closely supports a model where iron uptake is from the solution phase rather than directly from the cell surface, such equilibria would assure an adequate solution iron concentration for efficient uptake only if the solution phase iron derived from the surface was not free to diffuse away. However, in non-uniseriate plants, the cell wall space (apoplast) between cells is interconnected and serves as a continuous matrix through which surface bound nutrients could experience highly restricted diffusion despite the fact that it does not serve an obvious transport function. Maintaining a diverse cast of apoplastic polysaccharides with anionic ligands of considerable strength could be a strategy employed by *Ectocarpus* and likely many other marine macroalgae to buffer the widely fluctuating coastal iron concentrations. Such a mechanism could be biologically important and allow these organisms to be competitive particularly in high iron environments. Possible ecological evidence for this mechanism comes from the dramatic iron-induced phase shifts seen around some of the reefs on the Line Islands where corals dominate under natural oligotrophic conditions while macro and turf algae dominate near the site of recent shipwrecks releasing large amounts of iron into the

shallow-water marine environment (Kelly et al., 2012).

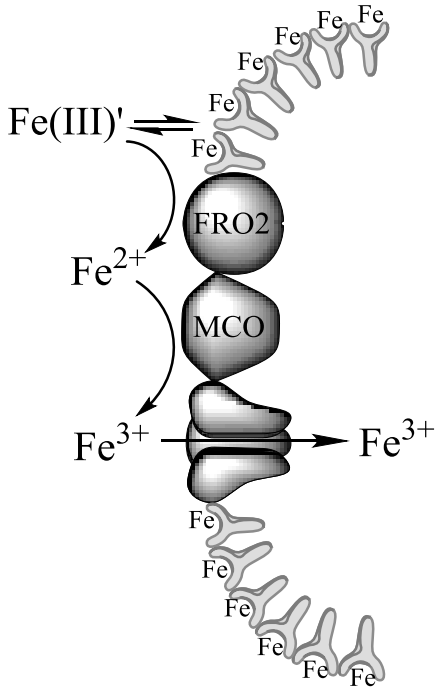

Figure I.2.1.12. Proposed mechanism for iron uptake in Ectocarpus. Free ferric iron in all its soluble forms (depicted as Fe(III)') is in equilibrium between the solution phase and the cell surface. The solution phase Fe(III)is reduced to Fe(II) by a cell-surface reductase homologous to the FRO2 protein of *Arabidopsis*. The resulting Fe(II) is then reoxidized by a multicopper oxidase (MCO) couples to an Fe(III) permease for final transport into the cell.

I.2.1.2. Methods

I.2.1.2.1. Algal culture

Ectocarpus strain EcSil NZ KU 1-3♂ (CCAP 1310NZ1310-56) was obtained from the Culture Collection of Algae and Protozoa (CCAP) at the Scottish Association for Marine Science. Cultures were grown axenically in Modified Provasoli-enriched (Andersen) Scripps Pier seawater (SPSW) at 17˚C with a 14h:10h light:dark photocycle at a photon flux density of ca. 80 µE m-2 s-1. They were grown either in borosilicate glass flasks or vented 250 mL tissue culture flasks (Greiner Bio-One, UK and USA) placed on a shaker at 80 rpm (IKA®Works, USA). Iron content of SPSW was determined to be approximately 4 nM and is thus defined as the concentration for iron-limited growth. Prior to all experiments, Ectocarpus was starved for a period of 5-10 days under iron-limited conditions. Iron-replete conditions were obtained by adding Fe-EDTA to SPSW at 30 µM.

I.2.1.2.2. Time-independent cellular iron

Ectocarpus was starved for a period of 7 days under iron-limited conditions. Radiolabeled Fe-EDTA stock solution was prepared by adding $^{55}FeCl_3$ (1522 MBq/mL; Perkin-Elmer) to ^{56}Fe-EDTA (1:10 Fe:EDTA) such that ^{55}Fe: ^{56}Fe equaled ca. 1:50. The complex was allowed to equilibrate for at least 24 hrs prior to use. Growth medium was inoculated with the ^{55}Fe-EDTA solution to give a final [Fe-EDTA] of 30 µM and grown over the course of 120 hrs. At selected time points, Ectocarpus filament aliquots were removed from the medium, washed with 25 mL “iron-free” artificial seawater (ASW), and filtered on to 5.0 µm polycarbonate filters (Millipore, USA) until dry. Filters

containing *Ectocarpus* filaments were placed in pre-weighed scintillation vials (Fisher Scientific, USA) containing 1 mL sodium hypochlorite (Fisher Scientific, USA). *Ectocarpus* dry mass was obtained by subtracting the filter mass. Samples were heated at 55℃ for 1 hr to eliminate quenching effects originating from chlorophyll. 15mL Hionic Fluor™ scintillation fluid (Perkin-Elmer, USA) was added to each scintillation vial and allowed to dark-adapt for at least 2 hrs in the scintillation counter (Beckman-Coulter LS 6500, USA) to eliminate any background chemiluminesence and phosphorescence prior to counting. Total iron uptake per mg dry *Ectocarpus* cells was calculated based on specific activity, measured count rates, scintillation counting efficiency, and biomass measurements. Surface-bound iron was defined as the ^{55}Fe signal of cells not treated with Ti(III)-citrate-EDTA less the internalized iron signal of titanium washed replicates (see section I.4 for reagent preparation details).

I.2.1.2.3. Cell surface-EDTA binding competition

An EDTA-cell surface chelate experiment was undertaken by preparing four ^{55}Fe radiolabeled Fe-EDTA stock solutions by adding $^{55}FeCl_3$ (1522 MBq/mL; Perkin-Elmer) to four ^{56}Fe-EDTA solutions (1:1.1, 1:10. 1:50, 1:100 Fe:EDTA) such that ^{55}Fe: ^{56}Fe equaled ca. 1:50. The stock solutions were allowed to equilibrate for at least 24 hrs prior to use. Eight *Ectocarpus* cultures with pH adjusted SPSW media (4 at pH 4.8, 4 at pH 8.7) were inoculated with the ^{55}Fe-EDTA solutions to give a final [Fe] of 1 µM. *Ectocarpus* was harvested, washed with 25 mL ASW, and filtered on to 5.0 µm polycarbonate filters (Millipore, USA) until dry. Filters containing Ectocarpus filaments were placed in pre-weighed scintillation vials (Fisher Scientific, USA) containing 1 mL

sodium hypochlorite (Fisher Scientific, USA). *Ectocarpus* dry mass was obtained by subtracting the filter mass. Samples were heated at 55℃ for 1 hr to eliminate quenching effects originating from chlorophyll. 15mL Hionic Fluor™ scintillation fluid (Perkin-Elmer, USA) was added to each scintillation vial and allowed to dark-adapt for at least 2 hrs in the scintillation counter (Beckman-Coulter LS 6500, USA) to eliminate any background chemiluminesence prior to counting. Total iron uptake per mg dry *Ectocarpus* cells was calculated based on specific activity, measured count rates, scintillation counting efficiency, and biomass measurements. Surface-bound iron was defined as the ^{55}Fe signal of cells not treated with Ti(III)-citrate-EDTA less the internalized iron signal of titanium washed replicates. Control data corresponding to internalized iron was defined as the ^{55}Fe signal of cells treated with Ti(III)-citrate-EDTA (see section I.4 for reagent preparation details).

I.2.1.2.4. Calculation of the cell surface effective binding constant, K'$_{eff}$

Cell surface iron affinity is expressed as the equilibrium constant K'_{eff} for reaction 1. The objective is to determine the affinity of $[Fe_T^{3+}]_{eq}$ for the cell surface by calculating the equilibrium constant K'_{eff} for Reaction 1 at a specific pH.

$$Cell + [Fe_T^{3+}]_{eq} \leftrightarrows FeCell \qquad (1) \qquad K'_{eff}$$

$Fe^{3+}{}_T$ in reaction 1 (also known as Fe(III)′) represents the total soluble and unbound aqueous iron(III) in all of its hydrolyzed forms (under our conditions ($Fe(H_2O)_6^{3+}$ + $Fe(H_2O)_5(OH)^{2+}$ + $Fe(H_2O)_4(OH)_2^{+}$ + $Fe_2(H_2O)_8(OH)_2^{4+}$). Cell surface iron affinity constants were estimated by measuring surface bound iron in reaction (1) with varying concentrations of EDTA and varying pH while [Fe(III)] remained fixed at

30 µM. In reaction (2) FeEDTA′ represents the total EDTA/iron(III) species ($FeEDTA^-$ + FeHEDTA + $Fe(OH)EDTA^{2-}$). We experimentally observe the following reaction (2) between *Cell* and $FeEDTA'$.

Cell + FeEDTA' $\leftrightarrows$ $FeCell + EDTA'$ (2) K'

EDTA' = Total species of EDTA in equilibrium = $EDTA^{4-}$ + $HEDTA^{3-}$ + H_2EDTA^{2-} + H_3EDTA^- + H_4EDTA + H_5EDTA^+

FeEDTA' = Total species of EDTA in equilibrium = $FeEDTA^-$ + *FeHEDTA* + *Fe(OH)*$EDTA^{2-}$

Relatively constant (±0.5 log unit) values were calculated for K'_{eff}at a constant pH over a range of experimental conditions (10 – 18 mg cells exposed to 33 – 1500 µM EDTA in the presence of 30 µM Fe^{3+} at pH 8.7 ±0.1), which confirms the validity of our assumptions and computational approach.

$$[Fe_T^{3+}]_{eq} = Total\ species\ of\ Free\ Fe^{3+} in\ equilibrium$$

$$= Fe(H_2O)_6^{3+} + Fe(OH)^{2+} + Fe(OH)_2^{+} + Fe_2(OH)_2^{4+}$$

$$K' = \frac{[FeCell][EDTA]'}{[Cell][FeEDTA]'} \qquad (3)$$

$$K' = \frac{[FeCell]}{[Cell][Fe_T^{3+}]_{eq}} X \frac{[Fe_T^{3+}]_{eq}[EDTA]'}{[FeEDTA]'} \qquad (4)$$

$$\beta' = \frac{[FeEDTA]'}{[Fe_T^{3+}]_{eq}[EDTA]'} \qquad (5)$$

$$K' = \frac{K'_{eff}}{\beta'} \qquad (6)$$

K' in Equations 3 through 6 can be corrected for EDTA and FeEDTA speciation using

Ringbom

$$K' = \frac{[FeCell][EDTA]'}{[Cell][FeEDTA]'} \qquad (3)$$

$$K' = \frac{[FeCell]}{[Cell][Fe_T^{3+}]_{eq}} X \frac{[Fe_T^{3+}]_{eq}[EDTA]'}{[FeEDTA]'} \qquad (4)$$

$$\beta' = \frac{[FeEDTA]'}{[Fe_T^{3+}]_{eq}[EDTA]'} \qquad (5)$$

$$K' = \frac{K'_{eff}}{\beta'} \qquad (6)$$

coefficients[1] to obtain K (Equation 10) for Reaction 7. FeCell and Cell represents all protonated forms.

$$Cell + FeEDTA^{-} \quad \leftrightarrows \quad FeCell + EDTA^{4-} \qquad (7) \qquad K$$

$$K = \frac{[FeCell][EDTA^{4-}]}{[Cell][FeEDTA^{-}]} \qquad (8)$$

$$K' = \frac{[FeCell][EDTA^{4-}]\alpha_{EDTA}}{[Cell][FeEDTA^{-}]\alpha_{EDTA}} \qquad (9)$$

$$K = \frac{K'\alpha_{FeEDTA}}{\alpha_{EDTA}} \qquad (10)$$

Equations 3 through 10 were obtained considering the equilibrium between the Cell and $FeEDTA'$ (Reaction 2) where K' is the equilibrium constant for the Reaction 2 at a specific pH. K'_{eff} is the effective binding constant for the cell and $[Fe_T^{3+}]_{eq}$ according to equilibrium Reaction 1.

Iron uptake by cells was monitored in the presence of varying concentrations of EDTA at a constant iron concentration. The amount of cells used in each experiment was

also varied over a wide range (10 – 18.6 mg). All relevant experimental data are summarized in Table I.2.2. Calculated equilibrium concentrations are summarized in Table I.2.3. Ringbom coefficients for iron, EDTA and FeEDTA were calculated using equations 11.

Table I.2.2. Experimental data used for calculations of equilibrium concentrations.

Expt.	pH	$[Fe]_{Init}$ / µM	$[EDTA]_{Init}$ / µM	$[Cell]_{Init}$/ mg	Fe uptake ng Fe/mg cell
1	8.7	30	33	11.2	998.8865
2	8.7	30	33	13.9	444.1926
3	8.7	30	33	11.2	602.3859
4	8.8	30	300	13.1	224.0947
5	8.8	30	300	18.6	179.4181
6	8.8	30	300	10.6	236.3291
7	8.6	30	1500	12.8	42.32842
8	8.6	30	1500	10.5	50.79342
9	8.6	30	1500	11.6	42.99006
10	4.8	30	3000	14.5	0.564329
11	4.8	30	3000	10	0.760243
12	4.8	30	3000	11.3	1.042555

Table I.2.3. Parameters used for calculating the reaction between Cell and FeEDTA.

Expt.	$[FeCell]_{eq}$ /mg	$[Cell]_{eq}$/ mg	$[EDTA]'_{eq}$ /µM	$[FeEDTA]'_{eq}$ /µM
1	0.01118	11.1888	13.018	19.98
2	0.00617	13.8938	8.53	24.47
3	0.00674	11.1932	9.04	23.96
4	0.00293	13.0970	272.63	27.37
5	0.00333	18.5966	272.98	27.01
6	0.00250	10.5975	272.24	27.76
7	0.00054	12.7994	1470.49	29.51
8	0.00053	10.4995	1470.48	29.52
9	0.00049	11.5995	1470.15	29.55
10	8.18×10^{-6}	14.4999	2970.007	29.99
11	7.60×10^{-6}	9.9999	2970.007	29.99
12	1.18×10^{-5}	11.2999	2970.011	29.99

to 24. β' obtained using Ringbom coefficients are also presented in Table I.2.4.

Table I.2.4. Ringbom coefficients calculated for the equilibrium between Fe^{3+} and EDTA and the equilibrium constant β'.

pH	α_{EDTA}	α_{FeEDTA}	$\alpha_{Fe(OH)}$	β'
8.8	25.599	27.915	1.99×10^{11}	8.81×10^{24}
8.7	31.986	22.379	1.25×10^{11}	1.37×10^{25}
8.6	40.036	17.982	7.94×10^{10}	5.65×10^{24}
4.8	5534346.12	1.003	2.06×10^{3}	2.28×10^{18}

Affinity constants calculated using equilibrium concentrations and Ringbom coefficients are given in Table I.2.5.

Table I.2.5. Binding constants (*K', K, and K'$_{eff}$*) for the reaction between cell and FeEDTA.

Expt.	K'	Average K'	K	Average K	K'_{eff}	Average K'_{eff}
1	6.52 x 10^{-4}	3.4 ± 2.7 x 10^{-4}	4.55 x 10^{-4}	2.4 ± 1.8 x 10^{-4}	5.74 x 10^{21}	3.03 x10^{21}
2	1.55 x 10^{-4}		1.08 x 10^{-4}		1.36 x 10^{21}	
3	2.27 x 10^{-4}		1.59 x 10^{-4}		2.00 x 10^{21}	
4	2.23 x 10^{-3}	2.1 ± 0.3 x 10^{-3}	2.43 x 10^{-3}	2.3 ± 0.3 x 10^{-3}	3.06 x 10^{22}	2.91 x 10^{22}
5	1.81 x 10^{-3}		1.97 x 10^{-3}		2.48 x 10^{22}	
6	2.32 x 10^{-3}		2.52 x 10^{-3}		3.18 x 10^{22}	
7	2.11 x 10^{-3}	2.3 ± 0.2 x 10^{-3}	9.47 x 10^{-4}	1.0 ± 0.1 x 10^{-3}	1.19 x 10^{22}	1.27 x 10^{22}
8	2.53 x 10^{-3}		1.14 x 10^{-3}		1.43 x 10^{22}	
9	2.13 x 10^{-3}		9.60 x 10^{-4}		1.21 x 10^{22}	
10	5.59 x 10^{-5}	7.8 ± 2.4 x 10^{-5}	1.01 x 10^{-11}	1.4 ± 0.4 x 10^{-11}	1.27 x 10^{14}	1.78 x 10^{14}
11	7.53 x 10^{-5}		1.36 x 10^{-11}		1.72 x 10^{14}	
12	1.03 x 10^{-4}		1.87 x 10^{-11}		2.35 x 10^{14}	

$$EDTA + nH \quad \leftrightarrows \quad H_nEDTA \qquad (11)$$

$$\beta_n^H = \frac{[H_nEDTA]}{[EDTA][H]^n} \qquad (12)$$

$$[EDTA]' = \alpha_{EDTA}\,[EDTA^{4-}] \qquad (13)$$

$$\alpha_{EDTA} = 1 + \beta_1^H[H] + \beta_2^H[H]^2 \ldots\ldots\ldots + \beta_5^H[H]^5 \qquad (14)$$

Successive log $\beta_n^H (n = 1 - 5)$ values (10.19, 16.32, 19.01, 21.01, and 22.51) were calculated from protonation constants for EDTA.

$$EDTA^{4-} + Fe^{3+} \quad \leftrightarrows \quad FeEDTA^{-} \qquad (15) \quad \beta_{110}$$

$$FeEDTA^{-} + H^{+} \quad \leftrightarrows \quad FeHEDTA \qquad (16) \quad K_1$$

$$Fe(OH)EDTA^{2-} + H^{+} \quad \leftrightarrows \quad FeEDTA^{-} \qquad (17) \quad K_2$$

$$\beta_{110}^{FeEDTA} = \frac{[EDTA^{-}]}{[Fe_{aq}^{3+}][EDTA^{4-}]} \qquad (18)$$

$$[FeEDTA]' = \alpha_{FeEDTA}\,[FeEDTA^{-}] \qquad (19)$$

$$\alpha_{FeEDTA} = 1 + K_1[H^+] + 1/(K_2[H^+]) \qquad (20)$$

Log β values used in the calculation of α_{FeEDTA} were ($\beta_{110} = 25.1$, $K_1 = 1.3, K_2 = 7.37$) for FeEDTA.

$$Fe(H_2O)_6^{3+} + OH^- \quad \rightleftarrows \quad Fe(OH)^{2+} \qquad (21) \quad K_1$$

$$Fe(H_2O)_6^{3+} + 2OH^- \quad \rightleftarrows \quad Fe(OH)_2^{2+} \qquad (22) \quad K_2$$

$$[Fe_T^{3+}]_{eq} = [Fe(H_2O)_6^{3+}]\, X\, \alpha_{Fe(OH)} \qquad (23)$$

$$\alpha_{Fe(OH)} = 1 + K_1[OH] + K_2[OH]^2 \qquad (24)$$

Formation of $Fe_2(OH)_2^{4+}$ depends on the concentration of Fe^{3+}. In most calculations, the concentration of Fe^{3+} is less than $10^{-3.7}$M. Therefore, $\alpha_{Fe(OH)}$ can be calculated neglecting $Fe_2(OH)_2^{4+}$. Log K_1 and K_2 are 11.0 and 21.7 respectively.

I.2.1.2.5. ^{55}Fe pulse/pulse-chase

Ectocarpus cells were incubated in 100 mL of 30 µM radiolabled ^{55}Fe-EDTA SPSW medium for 6 hours. Cells were then removed from the medium, washed with 5 mL low iron SPSW (ca. 4 nM ^{56}Fe) and then resuspended in 100 mL of either a) ultra-low iron oligotrophic Pacific Ocean water (ca. 0.1 nM ^{56}Fe) for the "pulse" experiment, or b) SPSW containing 30 µM "cold" ^{56}FeEDTA for the "pulse-chase" experiment. Ectocarpus was harvested at time points between 24 and 168 hours, washed with 25 mL ASW, and filtered on to 5.0 µm polycarbonate filters (Millipore, USA) until dry. Filters containing Ectocarpus filaments were placed in pre-weighed scintillation vials (Fisher Scientific, USA) containing 1 mL sodium hypochlorite (Fisher Scientific, USA). Ectocarpus dry mass was obtained by subtracting the filter mass. Samples were heated at

55℃ for 1 hr to eliminate quenching effects originating from chlorophyll. 15 mL Hionic Fluor™ scintillation fluid (Perkin-Elmer, USA) was added to each scintillation vial and allowed to dark-adapt for at least 2 hrs in the scintillation counter (Beckman-Coulter LS 6500, USA) to eliminate any background chemiluminesence prior to counting. Total iron uptake per mg dry *Ectocarpus* cells was calculated based on specific activity, measured count rates, scintillation counting efficiency, and biomass measurements. Surface-bound iron was defined as the ^{55}Fe signal of cells not treated with Ti(III)-citrate-EDTA less the internalized iron signal of titanium washed replicates. Internalized iron was defined as the ^{55}Fe signal of cells treated with Ti(III)-citrate-EDTA (see section I.4 for reagent preparation details).

I.2.1.2.6. Ferrocyanide-diaminobenzidine (Perls-DAB) staining

Environmental *Ectocarpus* cells were harvested from the shore near Dunstaffnage Marine Laboratory in Oban, Scotland. Cells were fixated in a pH 8.1, 0.1 µM phosphate buffer solution containing 2% (w/v) paraformaldehyde, 1% (w/v) glutaraldehyde, and 1% (w/v) caffeine for 2 hours. The fixed cells were then washed with 0.1 M phosphate buffer and dehydrated in successive ethanol baths of 30%, 50%, 75%, 85%, 95%, and (3X)100%. The cells were then embedded in 1:1 (v/v) ethanol/LR White resin (Electron Microscopy Sciences, USA) for 3 hours followed by 100% LR White overnight in gelatin capsules under vacuum. 3 µm sections were cut on a Reichert-Jung Ultracut E microtome and deposited on glass slides. The Perls staining and DAB intensification procedure was performed as previously described (Meguro et al., 2007; Roschzttardtz et al., 2009). Briefly, sections were incubated on glass slides with equal volumes 4% (v/v) HCl and 4%

potassium ferrocyanide (Perls staining solution) for 45 minutes. After washing with distilled H2O, sections were incubated in a methanol solution containing 0.01 M NaN_3 and 0.3% (v/v) H_2O_2 for 1 hour and then washed with 0.1 M phosphate buffer. DAB intensification was achieved by incubating sections in a 0.1 M phosphate buffer solution containing 0.00025-0.005% (w/v) DAB (Sigma), 0.005% (v/v) H_2O_2, and 0.005% (w/v) $CoCl_2$ for 30 minutes. The sections were then washed with H_2O before imaging with a Leica DMRB microscope.

I.2.1.2.7. Energy-dispersive X-ray spectroscopy (EDS)

Environmental *Ectocarpus* cells were harvested from the shore near Dunstaffnage Marine Laboratory in Oban, Scotland. Cells were fixated in a pH 8.1, 0.1 M phosphate buffer solution containing 2% (w/v) paraformaldehyde, 1% (w/v) glutaraldehyde, and 1% (w/v) caffeine for 2 h. The fixed cells were then washed with 0.1 M phosphate buffer and dehydrated in successive ethanol baths of 30, 50, 75, 85, 95, and (3X)100% . The cells were then embedded in 1:1 (v/v) ethanol/LR White resin (Electron Microscopy Sciences, USA) for 3 h followed by 100% LWR overnight in gelatin capsules under vacuum. Sections of 3 μm thickness were cut on a Leica EMUC6 microtome and deposited on glass slides. Slides were coated with carbon in a Quorum Technologies Q150T ES sputter coater (Quorum Technologies, United Kingdom). Platinum-coated samples were analyzed under high vacuum in a Quanta 450 FEG environmental scanning electron microscope (FEI, USA) equipped with an Oxford Instruments (Oxford Instruments, United Kingdom) INCA energy dispersive X-ray (EDX) microanalysis system.

I.2.1.2.8. Transmission Mössbauer Spectroscopy

Algal samples were either washed with the Ti(III)-citrate-EDTA reagent in order to remove adventitious iron from the algal surface, or they were used untreated (see section I.4 for reagent preparation details). Cells were harvested by vacuum assisted filtration. Pellets were weighed, transferred into Delrin® Mössbauer sample holders, frozen in liquid nitrogen, and kept at this temperature until measurement except for overnight transport on dry ice. The Mössbauer spectra were recorded in the horizontal transmission geometry using a constant acceleration spectrometer operated in conjunction with a 512-channel analyzer in the time-scale mode. The detector consisted of a proportional counter filled with argon-methane (9:1).The source was at room temperature and consisted of 1.4 GBq [^{57}Co] diffused in Rh foil (WissEl, Starnberg, Germany). The spectrometer was calibrated against α-iron at room temperature (RT). For measurements at 77K, samples were placed in a continuous-flow cryostat (Oxford Instruments). For measurements at 4.3K and 1.8 K a helium bath cryostat (MD306, Oxford Instruments) was employed. Spectral data were transferred from the multi-channel analyzer to a PC for further analysis employing the public domain Vinda program on an Excel 2003® platform (Microsoft, USA). Isomer shift δ, quadrupole splitting ΔE_Q, magnetic hyperfine splitting B_{hf}, line width Γ and percentage of the total absorption area were obtained by least-squares fits of Lorentzian lines to the experimental spectra. All values are rounded to the last given digit. The isomers shifts, the quadrupole splitting and the line width are given in mm/s. Hyperfine fields are given in Tesla. The relative area is given in parts per hundreds.

I.2.1.2.9. Extended X-ray absorption fine structure (EXAFS)

The K-edge iron X-ray absorption spectrum was recorded at the beamline D2 of the EMBL Outstation Hamburg at DESY, Germany. The DORIS storage ring operated at 4.5 GeV with the positron beam current ranging from 145 mA to 80 mA. A Si(111) double-crystal monochromator scanned X-ray energies around Fe K-edge (6.9 – 7.85 KeV). Harmonic rejection was achieved by a focusing mirror (cut-off energy at 20.5 KeV) and a monochromator detuning to 50% of its peak intensity. The sample cells were mounted in a two-stage Displex cryostat and kept at about 20 K. The X-ray absorption spectra were recorded as Fe K_{α} fluorescence spectra with a Canberra 13-element Ge solid-state detector. Data reduction, such as background removal, normalization and extraction of the fine structure, was performed with KEMP2 (Wellenreuther, 2009; Korbas, 2006) assuming a threshold energy $E_{0,Fe}$=7120 eV. Sample integrity during exposure to synchrotron radiation was checked by monitoring the position and shape of the absorption edge on sequential scans. No changes were detectable. Forward Fourier transformation was performed for a k-range from 2.1 $Å^{-1}$ to 10.0 $Å^{-1}$ using a Hanning window function. The final overall fit of the model (*vide infra)* uses only two legged scattering paths of Fe-O and Fe-[O]-C. The fits were performed in R-space using a Hanning type window from r=1 to 3.4 Å. For the least square fits in R-space a k-weight of 2 was used. All corrections and fits were performed with the Demeter 0.9.13 program package (Ravel and Newville 2005).

Model used to calculate scattering paths for EXAFS.

path	cw ratio	deg	n_{leg}	r_{eff} (Å)	atom
1	100.0	5.0	2	1.8147	O
2	19.214	1.0	2	1.8487	O
5	8.766	1.000	2	2.4615	C
7	1.152	2.000	3	2.5425	C
13	6.913	1.000	2	2.9016	O

Distances from Fe in column r_{eff} given in (Å).

Distances from Fe in model (Fig.I.2.1.11):

Fe-C (bidentate carboxylate), 2.5 Å

Fe-OH, 1.8 Å

Fe-C (bridging carboxylate), 2.7 Å

Fe-O carboxylate, 2.9 Å

I.2.2. Iron Uptake in *Ectocarpus siliculosus*

I.2.2.1. Results and Discussion

With the detection of a putative cell surface reductase homolog in the *Ectocarpus* genome (Cock et al., 2010), we sought experimental confirmation for external Fe(III) chelate reduction model for iron uptake (i.e. strategy 1). For these experiments *Ectocarpus* cells previously grown under either iron replete (30 µM) or limited (4 nM) conditions (see Material and Methods) were incubated in the presence of 30 µM ^{55}Fe FeEDTA and 100 µM of the Fe(II) specific chelator ferrozine (FZ) for 24 hours. Cells

were then harvested and the $^{55}Fe(FZ)_3$ complex formed in the supernatant assayed as described by Kranzler et al. (Kranzler et al., 2011). As can be seen from Figure I.2.2.1, iron limited *Ectocarpus* cells were readily capable of reducing Fe(III) in the form of an EDTA complex at a rate of approximately 1 ng Fe/mg-hr^{-1} i.e. commensurate with that of overall iron uptake. Dead cells exhibited no activity indicating that iron reduction was a specific metabolic process rather than a nonspecific one driven by the presence of FZ. Under iron replete conditions ferric chelate reduction was reduced by almost half suggesting that the reductase activity is inducible.

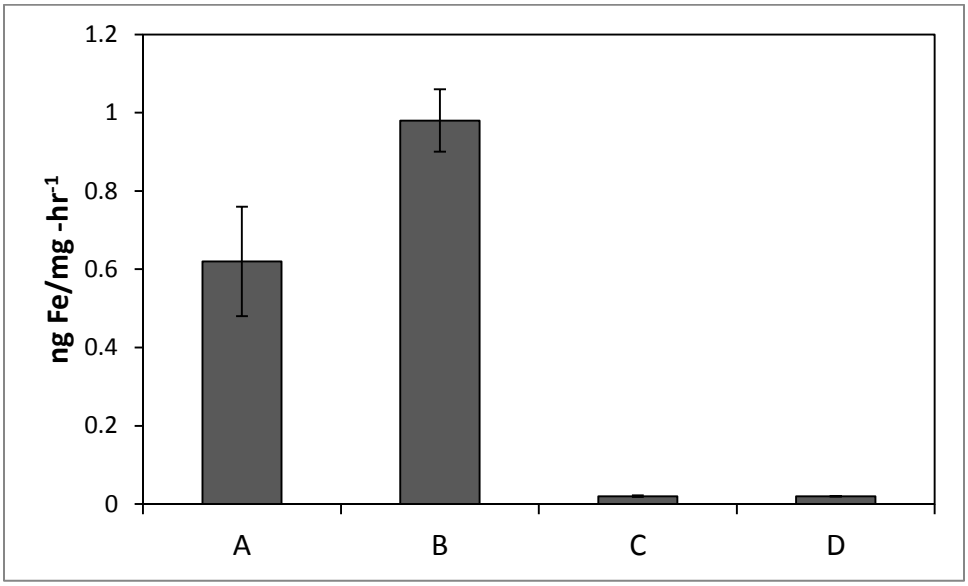

Figure I.2.2.1. Fe(III) chelate reductase activity for (A) iron-replete (30 μ M) and (B) iron-starved (4 nM) cultures of *Ectocarpus* grown as described in section I.2.2.3.4. (C) Dead cells and (D) live cells minus FZ represent negative controls. Error bars represent ±1 SD from triplicate measurements.

Iron "uptake" without the Ti(III) washing procedure described in the section I.4 was always very high and time independent; observations that are consistent with strong, nonspecific, cell surface binding. This nonspecific binding was confirmed by

transmission Mössbauer spectroscopy (TMS) which showed a very strong signal with spectral parameters distinct from those much weaker signals seen following the Ti(III) wash (*vide infra*). Careful and extensive washing of the cells with ASW following the Ti(III) wash was also required to prevent the artifactual observation of residual surface-bound Fe(II) by TMS. However with the appropriate care, ^{55}Fe from FeEDTA was seen to be taken up by iron-starved *Ectocarpus* in a time dependent fashion. Uptake was relatively rapid (0.44 ng/mg-hr^{-1}) and approximately linear for approximately 24 hrs after which the uptake rate slowed and eventually ceased (Figure I.2.2.2). The uptake process appeared to be an active one as it was inhibited by a number of metabolic

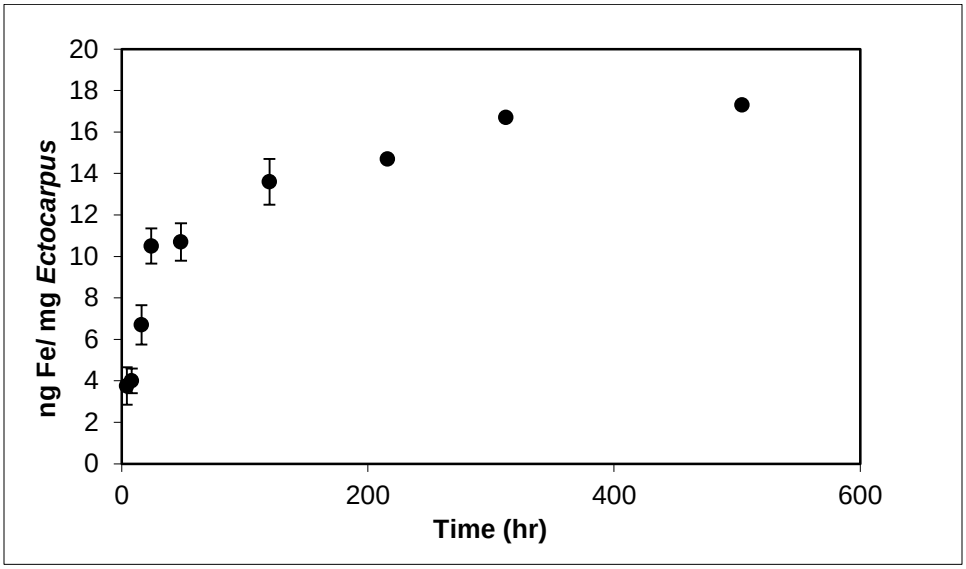

Figure I.2.2.2. Iron uptake from ^{55}FeEDTA as a function of time in *Ectocarpus* cultures over 800 h. Error bars represent ±1 SD from three separate experiments with replicate time points for each.

poisons or environmental effects. Pretreatment of cells with azide, CCCP, ascorbate, gramicidin or valinomycin resulted in 25 to 90% uptake inhibition (Figure I.2.2.3).

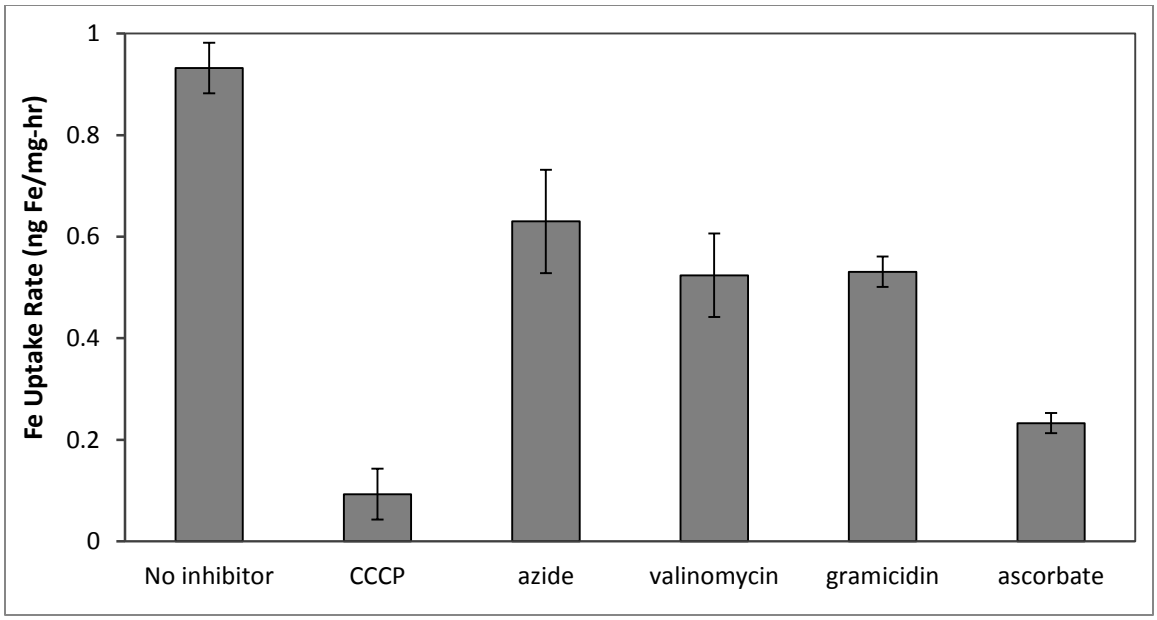

Figure I.2.2.3. Effect of metabolic and reductive inhibition on iron uptake rate in *Ectocarpus*. Error bars represent ±1 SD from three separate experiments with replicate time points for each.

The uptake process was also saturable as determined by its concentration dependence (Figure I.2.2.4) the data of which could be fit well ($R^2 = 0.9939$) to a model with a V_{max} = 1.47 ± 0.15 ng/mg-hr^{-1}, and a K_m = 1.5 ± 0.5 µM.

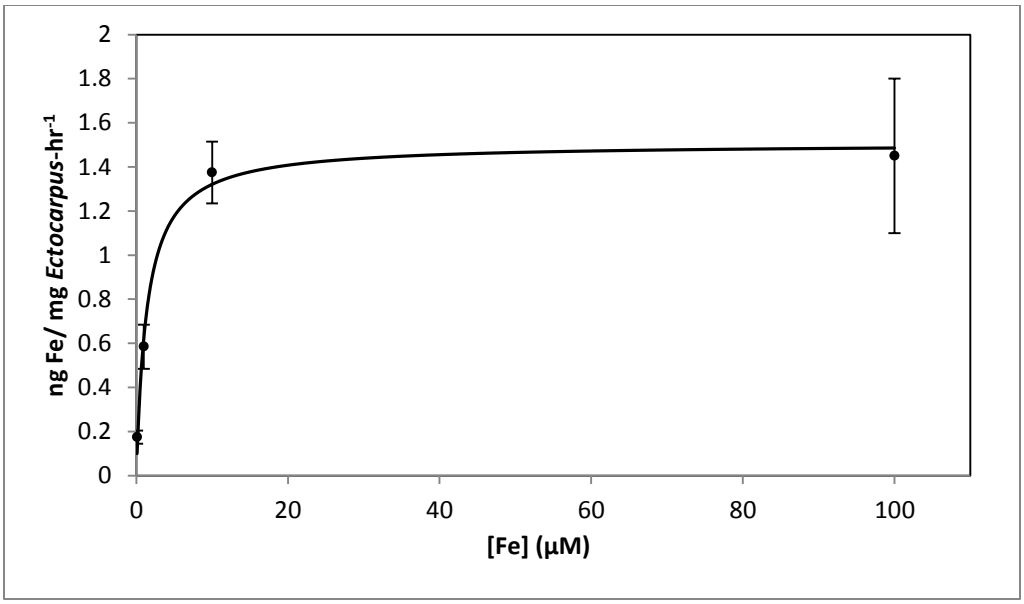

Figure I.2.2.4. Concentration-dependent uptake of iron from ^{55}FeEDTAafter 24 h by *Ectocarpus*. Error bars represent ±1 SD from duplicate experiments with replicate concentration points for each.

In the above experiments, FeEDTA was used as an iron source as it is generally thought that the intact FeEDTA complex is not a biological substrate but rather it serves as an iron buffer maintaining a fixed concentration of free soluble Fe(III) known as Fe(III)' at equilibrium while preventing the precipitation of insoluble Fe oxo-hydroxo polymeric species. To test the suitability of this hypothesis with *Ectocarpus* we looked at the iron uptake rate at a fixed concentration of iron as a function of increasing EDTA to Fe ratio. Increasing the EDTA to Fe ratio should increase the concentration of FeEDTA and decrease the concentration of free Fe(III) at equilibrium. Thus if FeEDTA itself was the biological substrate the uptake rate should increase while if free Fe(III) was the substrate then uptake should decrease. Upon going from an EDTA/Fe ratio of 1.5:1 to 100:1 we observe a 50 fold decrease in the uptake rate consistent with the idea that FeEDTA is serving simply as an iron buffer and the species actively involved in uptake is

free Fe(III)' (Figure I.2.2.5).

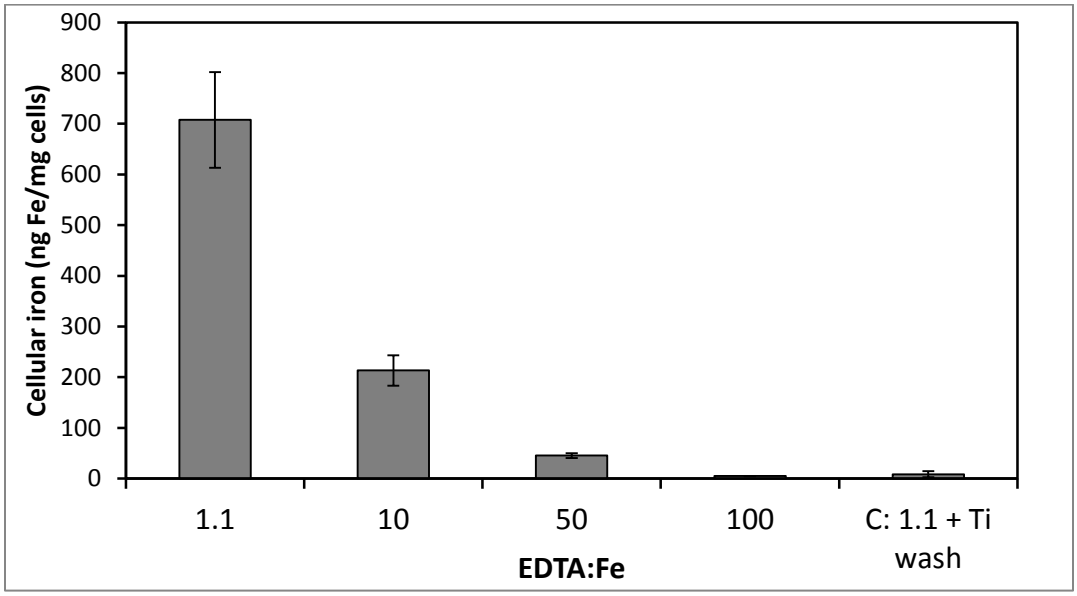

Figure I.2.2.5. Cell surface-bound iron as a function of excess EDTA in the media containing 30 µM FeEDTA. Error bars are mean ± standard deviation of triplicate measurements.

I.2.2.2. Discussion

In bacteria, there are a myriad of uptake systems and acquisition strategies designed to capture iron, many of which are often simultaneously operative in a single organism. These include uptake systems specific for siderophores, or other bound forms of iron (a similar system is also found in strategy II plants) as well as those based on ABC type transporters capable of taking up "free" Fe(III) and other transporters typically more or less specific for ferrous iron (Dassa and Bouige, 2001; Köster, 2001). Model eukaryotes typically adopt iron uptake schemes which involve reduction of Fe(III) to Fe(II) at some point although there appear to be exceptions (Sutak et al., 2010). The first of these mechanisms is a reductive-oxidative pathway such as that found in yeast (Curie and Briat, 2003) and some green algae (La Fontaine et al., 2002), the second a cell

surface reduction/divalent metal permease pathway such as that found in strategy I plants (Petra Bauer, 2003; Harold G. Weger, 2009; Morrissey and Guerinot, 2009; Sonier and Weger, 2010). Among the marine algae the iron uptake systems of the diatoms have been the most thoroughly studied (Shaked et al., 2005; Kustka et al., 2007). Iron uptake in these related organisms has been described by the so called Fe(II)s mechanism (Shaked et al., 2005) where reduction of free Fe(III)' is the seminal step. This reductive step is followed either by direct uptake of the formed Fe(II) as in the pennate diatom *P. tricornutum* or reoxidation of the Fe(II) by a multi-copper oxidase and transport as Fe(III) as in the centric diatom *T. pseudonana* (Kustka et al., 2007).

Genomic data suggests that *Ectocarpus* may, with some variation, use one or more of these approaches. In particular, homologs have been identified of *fro2*, a proposed cell surface Fe(III) reductase (Cock et al., 2010). This Fe(III) reductase activity was also experimentally verified and its rate was commensurate with that of the overall iron uptake process. Additionally, we could find homologs to several divalent metal ABC transporters (Curie and Briat, 2003; Petra Bauer, 2003; Peters et al., 2004; Charrier et al., 2008; Morrissey and Guerinot, 2009) as well as NRAMP, a M^{2+}-H^{+} symporter with a preference for Fe(II) (Curie and Briat, 2003; Petra Bauer, 2003; Morrissey and Guerinot, 2009) which would be consistent with the simple reductase/permease pathway. While we could find no direct homologs to the multi-copper oxidases (MCOs) Fox1 from *Chlamydomonas* or Fet3 of *T. pseudonana*, two genes annotated as MCOs implicated in iron transport can be found in the *Ectocarpus* genome.

Short term iron uptake studies verified that iron is taken up by *Ectocarpus* in a time and concentration dependent manner consistent with an active transport process.

Derived kinetic parameters are qualitatively and quantitatively similar to those reported in the few available studies other red, green and brown algae (Manley, 1981; Matsunaga et al., 1991; Liu et al., 2000). While it is difficult to compare V_{max} rates due to the differing units employed in each of these studies as well as the different surface / volume ratios of the model organisms, the uptake rate for the slow growing *Ectocarpus* is similar that seen in *Gracilaria* and approximately an order of magnitude less than that of the faster growing *Chlamydomonas, Laminaria* and *Macrocystis* (Manley, 1981; Matsunaga et al., 1991; Liu et al., 2000). However, the affinity constant (K_m) of ca. 1.5 µM is similar to the others which range from 0.1-3 µM. While open ocean iron concentrations are typically sub-nanomolar (Johnson et al., 1997), near shore coastal areas can have iron concentrations orders of magnitude higher i.e. hundreds of nanomolar (Chase et al., 2002). Thus, the affinity constants (based on total iron) seen for near shore dwelling macroalgae in the lower micromolar to high nanomolar range would appear to be reasonable. However it should be noted that if free soluble Fe(III)' rather than Fe(EDTA) itself is the actual substrate, as indicated by the constant Fe-variable EDTA concentration data presented earlier, then the true affinity constant is likely sub-nanomolar. However we report the data on the basis of total iron concentration in order to facilitate comparison to previous work (Manley, 1981; Matsunaga et al., 1991; Liu et al., 2000).

Although an initial reductive process is clearly indicated both genomically and experimentally, whether the iron is taken up directly as Fe(II) or reoxidized and transported as Fe(III) (*vide supra*) remains unclear. While the lack of inhibition of iron uptake by either FZ is surprising assuming a reductive process being operative, at the concentrations tested (50 µM) there is insufficient FZ to completely sequester all the

Fe(II) formed via the reductase as a $Fe(FZ)_3$ complex. Since the rate of reduction appears to exceed that of actual uptake there would remain a sufficient pool of uncomplexed Fe(II) to support continued uptake. Also possible is that the Fe(II) produced by the reductase is tightly coupled with an oxidase (*vide infra*) so that the ferrous ion is never in free equilibrium with the bulk solution and thus unaffected by the presence of an external Fe(II) chelator. The strong inhibition by ascorbate which at first glance also seems counter intuitive, suggests that a reductive/oxidative pathway may be the operative one as the ascorbate could be expected to inactivate a multi-copper oxidase.

Unfortunately, attempts to determine the oxidation state of the initially transported iron by TMS was thwarted by the low sensitively of the technique. Thus incubation times on the order of weeks in ^{57}Fe enriched solutions are required to obtain useable spectra. This precluded following short term iron uptake processes by this method. We have however been able to use TMS and XAS to provide evidence as to the fate of the transported iron after longer term exposure (3-4 weeks).

I.2.2.3. Methods

I.2.2.3.1. Algal culture

Ectocarpus strain EcSil NZ KU 1-3♂ (CCAP 1310NZ1310-56) was obtained from the Culture Collection of Algae and Protozoa (CCAP) at the Scottish Association for Marine Science. Cultures were grown axenically in Modified Provasoli-enriched (Andersen) Scripps Pier seawater (SPSW) at 17˚C with a 14h:10h light:dark photocycle at a photon flux density of ca. 80 μE m^{-2} s^{-1}. They were grown either in borosilicate glass flasks or vented 250 mL tissue culture flasks (Greiner Bio-One, USA) placed on a shaker

at 80 rpm (IKA®Works, USA). Iron content of SPSW was determined to be approximately 4 nM and is thus defined as the concentration for iron-limited growth. Prior to all experiments, *Ectocarpus* was grown for a period of 5-10 days under iron-limited conditions. Iron-replete conditions were obtained by adding Fe-EDTA to SPSW at 30 µM.

I.2.2.3.2. Time-dependent cell-associated iron

$^{55}FeCl_3$ radionuclide was obtained from Perkin-Elmer and used to prepare the ^{55}FeEDTA solution used as an iron source. *Ectocarpus* filaments were incubated in 30 µM $^{55/56}$FeEDTA over a 21 day period, with samples taken at the time points indicated. To remove any surface-adsorbed Fe(III) species, *Ectocarpus* samples were strained, washed with 50mL artificial seawater (ASW), followed by 10 mL of a titanium (III) citrate/EDTA solution prepared as described by Hudson and Morel (1989). This was followed by a final wash with 50 mL ASW to remove all traces of Fe(II). Samples were then filtered onto 10 µm Millipore™ polycarbonate filters and washed with 50mL ASW under a vacuum. Thorough washing with both the titanium reagent and subsequently with ASW is essential to eliminate artifacts caused by surface binding. Filters containing *Ectocarpus* were placed in scintillation vials and 1mL sodium hypochlorite was added to bleach the chlorophyll and reduce quenching effects. Vials were then heated in a 55˚C water bath for 1 hour and allowed to vent overnight at room temperature to allow chlorine evaporation. 15mL Hionic Fluor liquid scintillation fluid (Perkin-Elmer, USA) was added to each of the vials which were incubated in the dark for at least 2 hours to eliminate any background chemiluminesence and phosphorescence. The ^{55}Fe taken up

was measured on a Beckman-Coulter LS 6500 (Beckman-Coulter, USA) scintillation counter using the tritium channel. Total iron uptake per mg dry weight *Ectocarpus* was calculated based on specific activity, measured count rates, scintillation counting efficiency, and biomass measurements.

I.2.2.3.3. Concentration-dependent iron uptake

$^{55}FeCl_3$ radionuclide was obtained from Perkin-Elmer and used to prepare the ^{55}FeEDTA solution used as an iron source. *Ectocarpus* filaments were incubated in separate culture flasks containing media inoculated with 100nM, 1 µM, 10 µM, and 100 µM $^{55/56}$FeEDTA. *Ectocarpus* filaments were harvested after 24 hour incubation. To remove any surface-adsorbed Fe(III) species, *Ectocarpus* samples were strained, washed with 50 mL artificial seawater (ASW), followed by 10 mL of a titanium (III) citrate/EDTA solution prepared as described by Hudson and Morel (1989). This was followed by a final wash with 50 mL ASW to remove all traces of Fe(II). Samples were then filtered onto 10 µm Millipore™ (Millipore, USA) polycarbonate filters and washed with 50mL ASW under a vacuum. Thorough washing with both the titanium reagent and subsequently with ASW is essential to eliminate artifacts caused by surface binding. Filters containing *Ectocarpus* were placed in scintillation vials and 1mL sodium hypochlorite was added to bleach the chlorophyll and reduce quenching effects. Vials were then heated in a 55˚C water bath for 1 hour and allowed to vent overnight at room temperature to allow chlorine evaporation. 15mL Hionic Fluor liquid scintillation fluid (Perkin-Elmer, USA) was added to each of the vials which were incubated in the dark for at least 2 hours to eliminate any background chemiluminesence and phosphorescence.

The ^{55}Fe taken up was measured on a Beckman-Coulter LS 6500 (Beckman-Coulter, USA) scintillation counter using the tritium channel. Total iron uptake per mg dry weight *Ectocarpus* was calculated based on specific activity, measured count rates, scintillation counting efficiency, and biomass measurements.

I.2.2.3.4. Cell surface reductase activity

Cell surface reductase activity was determined as described by Kranzler et al. (Kranzler et al., 2011) using C18 Sep-Pak columns (Waters, USA) which adsorb the $^{55}Fe(FZ)_3$ complex formed by reduction of $^{55}FeEDTA$ in the presence of an excess of the Fe(II) specific chelator 3-(2-pyridyl)-5,6-diphenyl-1,2,4-triazine-p,p'-disulfonic acid (ferrozine, FZ). $^{55}FeCl_3$ radionuclide was obtained from Perkin-Elmer (Perkin-Elmer, USA) and used to prepare the $^{55/56}FeEDTA$ solution used as an iron source. *Ectocarpus* filaments were incubated in media containing 30 µM $^{55/56}FeEDTA$ and 100 µM FZ. After 8 hour incubation, media aliquots were passed through C18 Sep-Pak columns. After elution from the column with methanol, the $^{55}Fe(FZ)_3$ was quantified by adding 15mL Scintisafe liquid scintillation fluid (Perkin-Elmer, USA) to each of the vials. The vials were then incubated in the dark for at least 2 hours to eliminate any background chemiluminesence and phosphorescence. The ^{55}Fe taken up was measured on a Beckman-Coulter LS 6500 (Beckman-Couler, USA) scintillation counter using the tritium channel. Total iron uptake per mg dry weight *Ectocarpus* was calculated based on specific activity, measured count rates, scintillation counting efficiency, and biomass measurements.

I.2.2.3.5. Metabolic and reductive inhibition

For inhibition studies azide, carbonyl cyanide 3-chlorohydrazine (CCCP), ascorbate, and ionophores gramicidin and valinomycin were added to separate iron-limited cultures one hour prior to inoculation with $^{55/56}$FeEDTA. $^{55}FeCl_3$ radionuclide was obtained from Perkin-Elmer (Perkin-Elmer, USA) and used to prepare the ^{55}FeEDTA solution used as an iron source. *Ectocarpus* filaments were incubated in 30 µM $^{55/56}$FeEDTA and inhibitor for 24 hours. To remove any surface-adsorbed Fe(III) species, *Ectocarpus* samples were strained, washed with 50mL artificial seawater (ASW), followed by 10 mL of a Ti(III)-citrate-EDTA solution prepared as described by Hudson and Morel (Hudson and Morel, 1989). This was followed by a final wash with 50 mL ASW to remove all traces of Fe(II). Samples were then filtered onto 10 µm Millipore™ (Millipore, USA) polycarbonate filters and washed with 50 mL ASW under a vacuum. Thorough washing with both the titanium reagent and subsequently with ASW is essential to eliminate artifacts caused by surface binding. Filters containing *Ectocarpus* were placed in scintillation vials and 1 mL sodium hypochlorite was added to bleach the chlorophyll and reduce quenching effects. Vials were then heated in a 55˚C water bath for 1 hour and allowed to vent overnight at room temperature to allow chlorine evaporation. 15mL Hionic Fluor liquid scintillation fluid (Perkin-Elmer, USA) was added to each of the vials which were incubated in the dark for at least 2 hours to eliminate any background chemiluminesence and phosphorescence. The ^{55}Fe taken up was measured on a Beckman-Coulter LS 6500 (Beckman-Coulter, USA) scintillation counter using the tritium channel. Total iron uptake per mg dry weight *Ectocarpus* was calculated based on

specific activity, measured count rates, scintillation counting efficiency, and biomass measurements.

I.2.3. Iron Storage in *Ectocarpus siliculosus*

I.2.3.1. Results

Having established an uptake mechanism via short-term incubation experiments, we turned to an examination of long-term iron storage. Using the ferrocyanide-diaminobenzidine (DAB) staining protocol described by Roschzttardtz et al. and Meguro et. al. (Meguro et al., 2007; Roschzttardtz et al., 2009) it is possible to visualize the localization of iron at the subcellular level. The highest levels of iron consistently appeared as small dark granules clustered together inside the cell and not associated with the plastids, which in *Ectocarpus* typically adopt a spiral banded pattern (Figure I.2.3.1). Control cell slices not treated with ferrocyanide-DAB do not show such a staining pattern. While the exact nature of the structures that contain the majority of iron remains obscure it is clear that large concentrations of iron appear to be stored inside *Ectocarpus* cells.

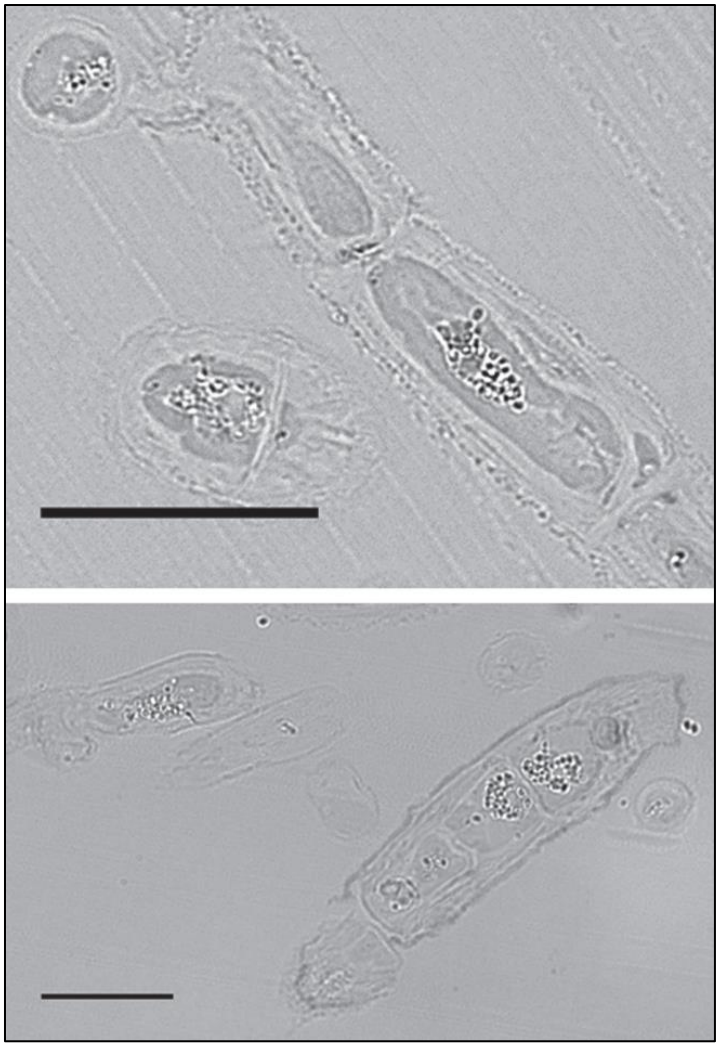

Figure I.2.3.1. Micrographs (×63) of 3 µm sections of *Ectocarpus* cells embedded in LWR and stained by the DAB procedure. Upper panel: treatment with 0.0025% DAB. Lower panel: treatment with 0.005% DAB. The dark grains represent high concentrations of iron. Scalebars, 20 µm.

After long-term (33 days) incubation in ^{57}FeEDTA enriched culture medium, transmission Mössbauer spectroscopy (TMS) spectra exhibiting sufficient resonance absorption were obtained which display a single quadrupole doublet-like feature (Figure I.2.2.6). Since the algal filament was thoroughly washed with the Ti(III)-citrate-EDTA reagent, the presence of iron on the algal surfaces can be excluded and therefore, the iron

components observed by TMS are genuinely of intracellular origin. From this, it can be concluded, that ^{57}Fe supplied as EDTA complex in the medium is transported into, and metabolized inside, cells of *Ectocarpus*. However, despite its seeming simplicity, detailed analysis of the TM spectrum showed the presence of two different and distinct iron species. The first corresponds to a $(Fe_4S_4)^{2+}$ cluster. Biological $[Fe_4S_4]^{n+}$ clusters are typically found in 3 cluster oxidation states: 1+, 2+ and 3+ (Schünemann and Winkler, 2000). All three types of $[Fe_4S_4]$ cluster exhibit characteristic Mossbauer parameters which can be distinguished in most cases quite well. An iron sulphur cluster in the +2 state displays at 4.3K isomer shifts in the range from 0.39 to 0.45mms^{-1} and quadrupole splittings from 0.98 to 1.22 mms^{-1}. Isomer shift and quadrupole splitting of the iron sulphur species in the *in situ* Mössbauer spectrum of *Ectocarpus* are in the range found for such a cluster (26% of absorption area, Table I). This iron sulfur cluster very likely represents a component of chloroplast and/or mitochondrial redox systems. The second iron compound detected by TMS displays a spectrum typical of a polymeric $(Fe^{3+}O_6)$ system which accounts for 74% of the absorption area (Table I.2.2, Figure I.2.3.2). Polymeric biological $(Fe^{3+}O_6)$ systems found by *in situ* Mossbauer spectra very often represent the mineral cores of ferritins. The Mössbauer spectroscopic features of such systems are strongly temperature and size dependent reflecting superparamagnetic relaxation of magnetic nanoparticles (Mørup, 2011). Bacterial ferritins (Bfr and Ftn) typically show superparamagnetic splitting (doublet-sextet transition) at temperatures below 4.3K indicating an amorphous and frequently phosphate rich crystal structure (Bauminger et al., 1980a; Bauminger et al., 1980b; Mann et al., 1987; Reindel et al., 2002; Boughammoura et al., 2008). The sextet lines show one third of the resonance

absorption compared to the doublet lines and are, in addition, considerably broadened due to particle size distributions of the mineral. The Mössbauer spectrum of *Ectocarpus* at 1.8K shows less resonance absorption in the center part compared to that seen at 4.3K (0.2 transmission intensity as compared to 0.45) indicating the partial disappearance of one doublet The disappearance of the ($Fe^{3+}O_6$) doublet can only be explained (since the Lamb-Mössbauer factor, f, at 1.8K cannot be smaller than that at 4.3K) by the formation of a broadened six-line pattern; the result of a doublet-sextet transition as found in bacterial ferritins. However due to the low intensity of the ($Fe^{3+}O_6$) doublet lines the six-line pattern is at the detection limits of TMS (0.1% effect per line or even less). The residual absorption at 1.8K could be adequately fit with just the iron-sulfur species.

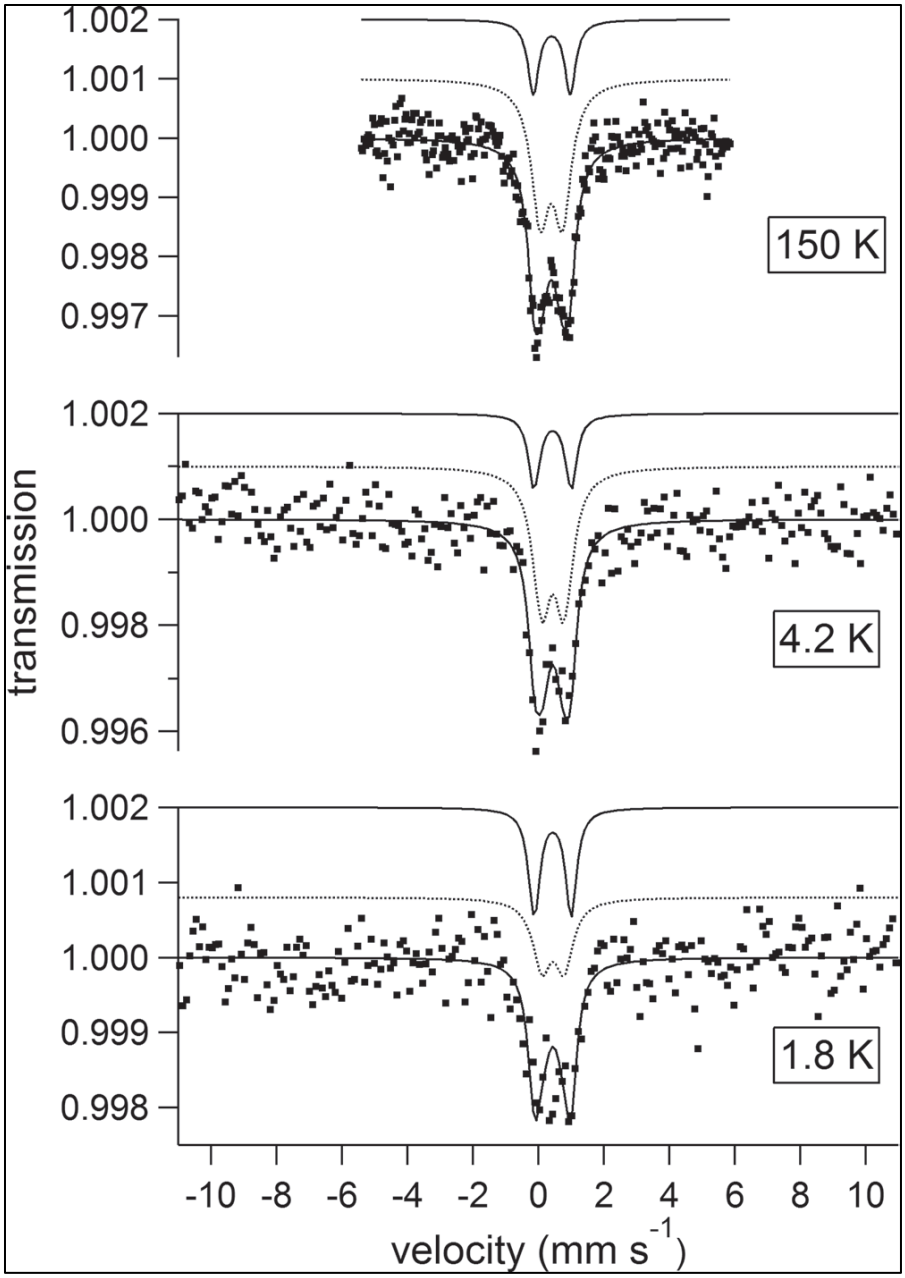

Figure I.2.3.2. Mössbauer spectra of *Ectocarpus* at 150K (upper), 4.3K (middle), and 1.8K (lower). The filled squares represent the experimental data. The subspectra obtained by least squares fits of Lorentzian lines are depicted by the light grey solid line (Fe_4S_4) and dark grey dotted line (polymeric FeO_6). The black solid line represents the overall fit.

Table I.2.6. Mössbauer fit parameters of isomer shift (δ), quadrupole splitting (ΔE_Q) linewidth (Γ) , and percentage of absorption area in % of *Ectocarpus* (CC45) at 150 4.2 and 1.8 K. Error in last digit is 0.04 $mm.s^{-1}$.

	Parameter	In mm s^{-1} at 1.8K	In mm s^{-1} at 4.2K	In mm s^{-1} at 150K
$[Fe^{3+}O_oX_m^{n}]^{mn-9}$	δ	0.44	0.44	0.39
	ΔE_Q	0.68	0.68	0.68
	Γ	0.66	0.66	0.66
	Area	50%	74%	74%
$[Fe_4\text{-}S_4]^{2+}$	δ	0.43	0.43	0.40
	ΔE_Q	1.13	1.13	1.13
	Γ	0.41	0.41	0.41
	Area	50%	26%	26%
SQRT		0.86	0.79	0.80

In addition to TMS, X-ray absorption spectroscopy (XAS) was employed to probe the chemical nature of the internalized iron. Based on the above TMS data the presence of a superparamagnetically coupled polymeric Fe^{3+}-oxo system and of a $[Fe_4S_4]^{2+}$ cluster were indicated. Within this constraint various models were tested. For the Fe^{3+}-oxo species the models tested included ferric (oxo, oxo-organic, oxo-phosphate), ferrihydrite, ferric phosphate, and FeO(OH). Models for these species were constructed and coordinates obtained after molecular mechanics energy minimization using the program Chem 3D. These coordinates were then used as for input in the FEFF program to obtain the scattering paths. The best fits came from the oxo-phosphate model. However the resulting fits were still unsatisfying when only oxo-phosphate ligands were employed in the first ligand sphere. There was definitely an iron sulphur contribution which was consistent with the Mossbauer spectra. Structural data for various Fe-S clusters were extracted from the appropriate data banks, and coordinates extracted after molecular mechanics energy minimization using the Program Chem3D. The resulting coordinates were again used for input in the FEFF program to obtain the scattering paths. Acceptable

fits were only obtained for an $[Fe_4S_4]^{2+}$ cluster.

The final fit of the EXAFS spectrum (Figures I.2.3.3 and I.2.3.4) to the two component model (i.e. polymeric Fe(III) oxo-phosphate and an $[Fe_4S_4]^{2+}$ cluster) was very good where the second coordination shell of the Fe-oxo species contains 3.5 ± 0.5 P and 1 ± 0.5 Fe (Table I.2.3). The Fe-oxo species comprises approximately 74% and the Fe-S species approximately 26% of the total iron. The average bond distances obtained from the EXAFS fit are summarized in Table I.2.3. Attempts to add additional components such as a $[Fe_2S_2]^{2+}$ (or additional Fe-oxo species) provided no statistically significant improvement to the fit. Overall, the EXAFS fit data are completely consistent with that obtained by TMS. In particular, they support both quantitatively and qualitatively the polymeric nature of the iron oxo species and the presence of an iron-sulfur protein as suggested by the TMS spectra.

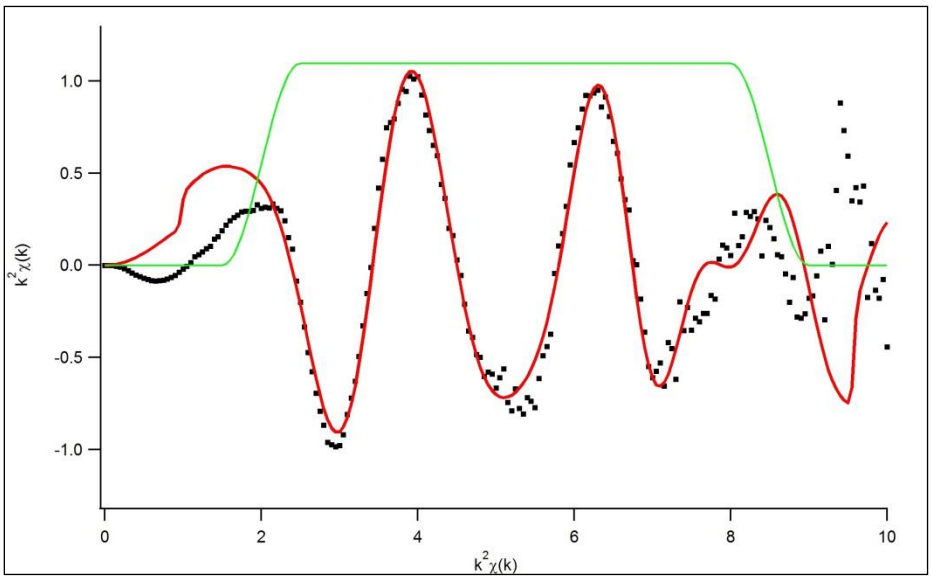

Figure I.2.3.3. Extracted EXAFS spectrum of 52 merged spectra transformed in k-space. Black squares represent experimental data; the red line represents the fit. The green line depicts the setting of the range.

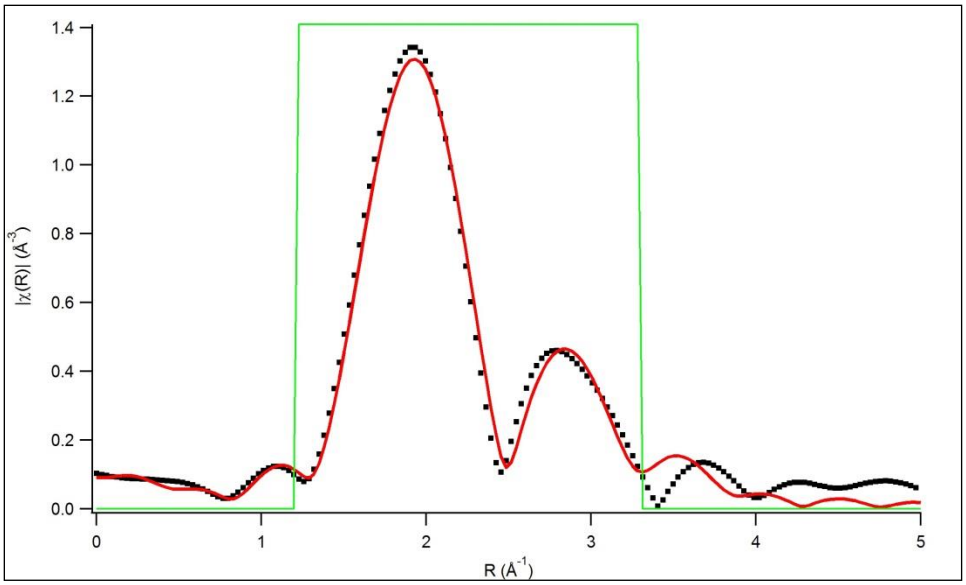

Figure I.2.3.4. EXAFS data of CC47 plotted in R-space. The graph was plotted with a k-weight of 1 and a phase correction. The k-range for the fast Fourier transformation was 2 Å-1 to 8.5 Å-1. The fit was performed with a model containing FeO_6 and Fe_4S_4 structures due to the limited R range up to r=3.35 Å as described in the text. Black squares represent experimental data; the red line represents the fit. The green line depicts the setting of the range.

Table I.2.7. Average distances and numbers of first and second shell ligands in Fe-O and Fe-S iron centers of sample CC47 obtained from the EXAFS fit as described in text. The accuracy for ligand numbers N is ±0.5. Elements in brackets display bond angles indicating that the Fe-(X)-Y distance is shorter than the summation of individual bond lengths.

	Fe-O	Fe-(O)-P	Fe-(O)-Fe	Fe-S	Fe-(S)-Fe
Å	1.96	3.07	3.35	2.11	2.64
N	6	3.5	1	4	3

I.2.3.2. Discussion

The first and most obvious conclusion from the long term incubation studies is the lack of an observable ferrous iron pool in *Ectocarpus*. In previous *in vivo* Mössbauer studies by us and others of various bacterial, fungal, plant and algal systems significant amounts of intracellular high-spin ferrous iron octahedrally coordinated by oxygen ligands could be detected (Böhnke and Matzanke, 1995; Winkelmann and Carrano, 1997; Semin et al., 2003; Matzanke et al., 2004; Kovács et al., 2006; Kovács et al., 2009). There is no evidence for such a species in *Ectocarpus*. Thus despite the fact that the iron is likely transported across the cell membrane as Fe(II), it must be relatively rapidly reoxidized to Fe(III) and stored in that form. Of the two major metabolites we could identify, one was an iron sulphur protein which is likely a component of chloroplast and/or mitochondrial redox systems. However, a storage role for this species cannot be eliminated since in some archaeal systems polyferredoxins were detected, whose physiological function, while unclear, has been hypothesized to serve as electron sinks (Nölling et al., 1995; Wasserfallen et al., 1995). Nevertheless, the vast majority of organisms store iron in one or more of the various forms of the ubiquitous protein ferritin. However, our genomic analysis reveals the presence of no ferritin or ferritin-like homologs in *Ectocarpus* (Cock et al., 2010). While this is unusual it is not unprecedented. Thus while some diatoms such as *P. tricornutum* have ferritin genes, they have not been detected in others such as *T. pseudonana* (Marchetti et al., 2009).

In the absence of ferritins two alternate or additional forms of iron storage have been identified in other organisms. The first, found in some fungi, is a siderophore based storage system (Matzanke et al., 1987; Matzanke et al., 1988) is clearly not present here.

The second, which has been elucidated in yeast and several other eukaryotes including the halotolerant alga *Dunaliella salina* is a vacuole based one (Martinoia et al., 2007; Paz et al., 2007). At present, there is little data in the literature about the chemical nature of vacuole sequestered iron stores. However, it seems likely that the iron would be stored in some sort of mineral phase. Indeed it is reported that in *Arabidopsis* seeds some iron is located in vacuole globoids containing phytate which may bind ferric ions via phosphate groups (Lanquar et al., 2005) similar to what we propose here. This notion is supported by the iron specific histological staining which show accumulation of high concentrations of granular-like iron stores inside *Ectocarpus* cells.

Since the spectroscopic parameters and relaxation properties (i.e. magnetic ordering temperatures) of condensed iron mineral phases are strongly dependent on particle sizes and their crystalline/amorphous structure, detailed temperature dependent Mössbauer measurements can shed light on the nature of any iron stores. The observation that the second iron compound detected by TMS and XAS display spectra typical of a ($Fe^{3+}O_6$) system with parameters similar to the amorphous, phosphorus rich mineral core of bacterial and plant ferritins suggests that *Ectocarpus* does indeed contain a mineral phase iron storage form. Whether this mineral phase is in the form of a ferritin-like protein which lacks significant homology to previously studied systems, or is sequestered in some sort of vacuole remains to be determined. Work geared towards more fully characterizing this system is in progress.

I.2.3.3. Methods

I.2.3.3.1. Ferrocyanide-diaminobenzidine (Perls-DAB) staining

Ectocarpus was grown in 30 μM FeEDTA Provasoli enriched SPSW culture medium for 30 days. Prior to fixation, dehydration, and embedding, filaments were washed with 10mL Ti(III) reagent (see section I.4 for reagent preparation details). Cells were fixated in a 0.1 M phosphate buffer solution containing 2% (w/v) paraformaldehyde, 1% (w/v) glutaraldehyde, and 1% (w/v) caffeine for 2 hours. The fixed cells were then washed with 0.1 M phosphate buffer and dehydrated in successive ethanol baths of 30%, 50%, 75%, 85%, 95%, and 100% (3X). The cells were then embedded in 1:1 (v/v) ethanol/LR White resin (EMS) for 3 hours followed by 100% LR White overnight in in gelatin capsules under vacuum. Three micron sections were cut on a Leica EMUC6 (Leica Biosystems, USA) microtome and deposited on glass slides. The Perls staining and DAB intensification procedure was performed as described by Meguro et al. and Roschzttardtz et al. (Meguro et al., 2007; Roschzttardtz et al., 2009). Briefly, sections were incubated on glass slides with equal volumes 4% (v/v) HCl and 4% potassium ferrocyanide (Perls staining solution) for 45 minutes. After washing with distilled H_2O, sections were incubated in a methanol solution containing 0.01 M NaN_3 and 0.3% (v/v) H_2O_2 for 1 hour and then washed with 0.1 M phosphate buffer. DAB intensification was achieved by incubating sections in a 0.1 M phosphate buffer solution containing 0.00025-0.005% (w/v) DAB (Sigma), 0.005% (v/v) H_2O_2, and 0.005% (w/v) $CoCl_2$ for 30 minutes. The sections were then washed with H_2O before imaging with a Zeiss Axiovert 40 (Zeiss, Germany) inverted microscope.

I.2.3.3.2. Transmission Mössbauer spectroscopy (TMS)

Ectocarpus was grown for 33 days in modified Provasoli enriched seawater containing 30 µM ^{57}FeEDTA. ^{57}Fe was obtained as the oxide from Isoflex (San Francisco, CA) and converted to the chloride by repeated dissolution in concentrated HCl. The chloride was subsequently added to a concentrated solution of EDTA and the pH adjusted to 6.0. Algal samples were washed with the titanium citrate/EDTA reagent in order to remove adventitious iron from the algal surface and the cells were harvested by vacuum assisted filtration. Pellets were weighed, transferred into Delrin® Mössbauer sample holders, frozen in liquid nitrogen, and kept at this temperature until measurement except for overnight transport on dry ice. The Mössbauer spectra were recorded in the horizontal transmission geometry using a constant acceleration spectrometer operated in conjunction with a 512-channel analyzer in the time-scale mode. The detector consisted of a proportional counter filled with argon-methane (9:1).The source was at room temperature and consisted of 1.4 GBq (^{57}Co) diffused in Rh foil (WissEl, Starnberg, Germany). The spectrometer was calibrated against α-iron at room temperature (RT). For measurements at 77K, samples were placed in a continuous-flow cryostat (Oxford Instruments). For measurements at 4.3K and 2K a helium bath cryostat (MD306, Oxford Instruments) was employed. Spectral data were transferred from the multi-channel analyzer to a PC for further analysis employing the public domain Vinda program on an Excel 2003® platform. Isomer shift δ, quadrupole splitting ΔE_Q, B_{hf} and percentage of the total absorption area were obtained by least-squares fits of Lorentzian lines to the

experimental spectra. All values are rounded to the last given digit. The isomers shifts (δ), the quadrupole splitting (ΔE_Q) and the line width (Γ) are given in mm/s. The relative area is given in parts per hundreds.

I.2.3.3.3. Extended X-ray absorption fine structure (EXAFS)

Ectocarpus was grown for 33 days in modified Provasoli enriched seawater containing 30 µM ^{57}FeEDTA. ^{57}Fe was obtained as the oxide from Isoflex (San Francisco, CA) and converted to the chloride by repeated dissolution in concentrated HCl. The chloride was subsequently added to a concentrated solution of EDTA and the pH adjusted to 6.0. Algal samples were washed with the titanium citrate/EDTA reagent in order to remove adventitious iron from the algal surface and the cells were harvested by vacuum assisted filtration. Pellets were weighed, transferred into Delrin® XAS sample holders with a Mylar film cover, frozen in liquid nitrogen, and kept at this temperature until measurement except for overnight transport on dry ice. Spectra were measured at Doris III, beamline A1 (DESY, Hamburg, Germany) using a fluorescence detector. Frozen samples were measured in a continuous flow cryostat (Oxford Instruments, Optistat) at 12K. The energy was calibrated in transmission mode against an iron foil while experimental spectra were recorded in the fluorescence mode. Algal samples were prepared as described above and sample CC45 (Mössbauer) and CC47 (EXAFS) were prepared from the same batch. During sample handling the sample temperature was kept below 195 K.Thirty nine energy scans from 6960 eV to 8112 eV were performed resulting in 52 spectra. Spectra obtained during ring filling were skipped. Each scan was performed as follows: from 6960 eV to 7085 eV the energy step E was 5 eV, from 7085

eV to 7152 eV ΔE was 0.5 eV and from 7152 eV to 8112 eV non-equidistant energy steps were used starting at ΔE = 0.8 eV. In the first two regions a sampling time of one second was used. In the third region an increasing sampling time was used corresponding to the non-equidistant energy steps starting at one second.

In each spectrum the K-edge was localized by the zero crossing of the second derivative of the fluorescence signal and corrected against the iron foil K-edge. All spectra were summed up prior to correction. Afterwards the sum was corrected as follows: The pre-edge range was defined relative to the determined K-edge from -150 eV to -30 eV and fitted with a line. The post-edge range for normalization was set relative to the K-edge from +150 eV to +880 eV and was fitted with a quadratic polynomial. The sum spectrum was corrected for its background, its pre-edge and normalized to its post-edge. Forward Fourier transformation was performed for a k-range from 2 $Å^{-1}$ to 8.5 $Å^{-1}$ using a Hanning window function. The final overall fit of the two component model (*vide infra)* uses scattering paths with distances below 3.4 Å. The fits were performed in R-space using a Hanning type window from r=1.2 Å to 3.35 Å. For the least square fits in R-space a k-weight of 2 was used. All corrections and fits were performed by the Athena/Artmis program package of Bruce Ravel (Ravel and Newville, 2005).

I.3. Cell Surface-Binding and Iron Storage in *Macrocystis pyrifera*

I.3.1. Cell Surface-binding of Iron in *Macrocystis pyrifera*

I.3.1.1. Results

I.3.1.1.1. Kinetics and thermodynamics of surface-bound iron

Prior to the development of the Ti(III)-citrate-EDTA washing reagent (Hudson

and Morel, 1989) an alternative washing step (10 μM EDDHA) was used in *Macrocystis* studies to remove surface-bound and free space iron (Manley, 1981). Surface-bound iron is defined as iron uptake (washed samples) subtracted from total cellular iron (unwashed replicates). The effectiveness of this EDDHA reagent was reported to be ~90%; however, data is lacking for surface bound iron for timeframes greater than 30 min (Manley, 1981). While it is clear from Figure I.3.1.1 that surface binding of iron is much slower kinetically than that of *Ectocarpus*, the extent of this binding has not been studied.

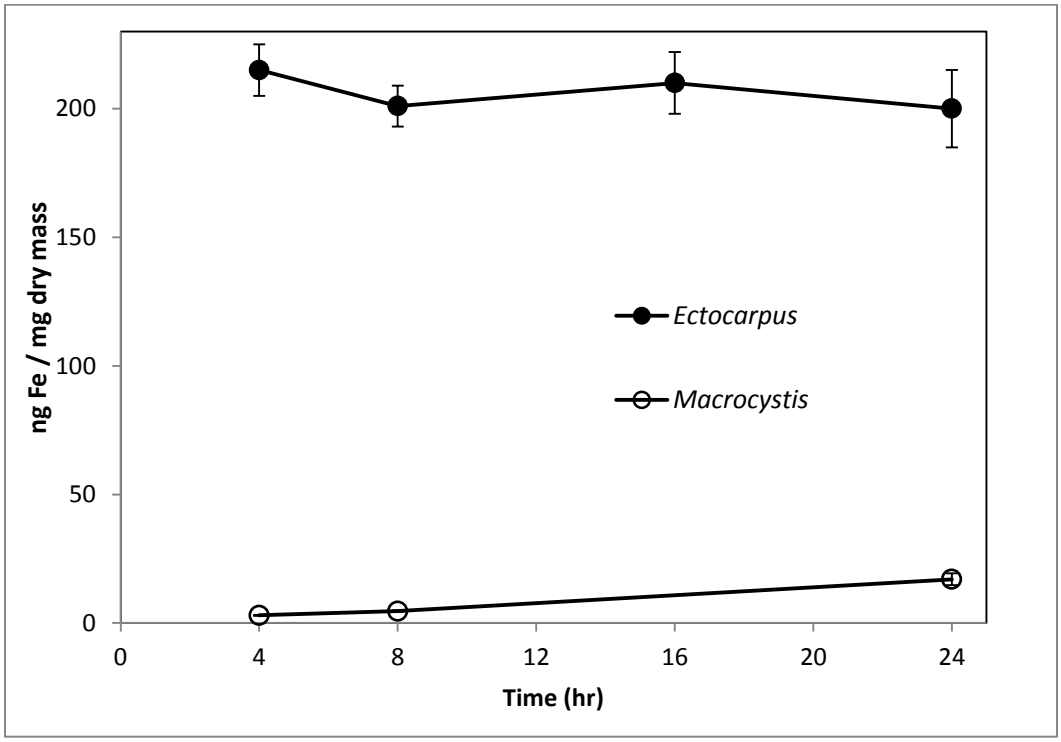

Figure I.3.1.1. Surface-binding of iron in *Ectocarpus* (closed circles) and immature *Macrocystis* blade (open circles) as a function of time. Error bars represent ±1 SD from triplicate measurements.

Further, a significant variability in the degree of surface-binding versus uptake exists as a function of life-cycle and tissue type. As can be seen in Figure I.3.1.2, immature *Macrocystis* blades (<1 m from frond apex) bind 7-fold more iron on the cell surface than

that of mature blades (>3 m from apex). Immature blades also took up 40-fold more iron intracellularly than mature blades (Figure I.3.1.2).

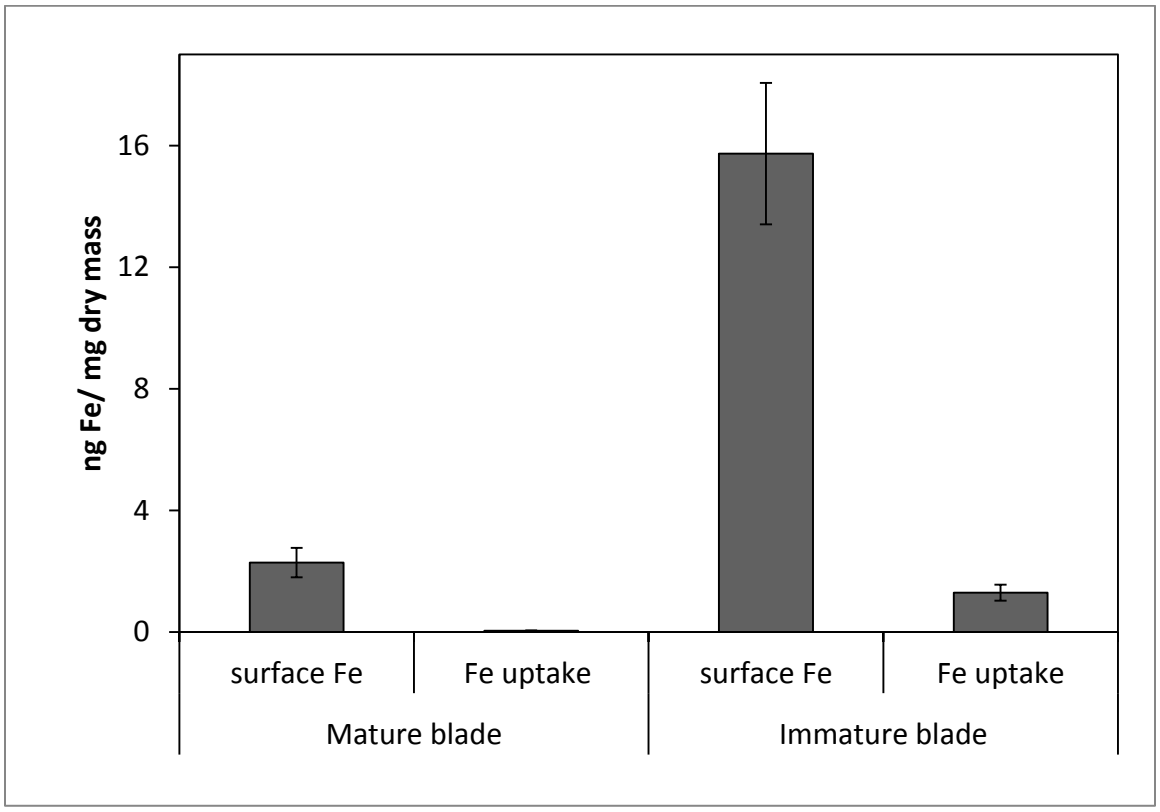

Figure I.3.1.2. Surface-bound vs. intracellular iron in *Macrocystis* blade as a function of life cycle. Error bars represent ±1 SD from triplicate measurements.

Macrocystis stipe also exhibits a variable degree of cell surface-binding of iron depending on life-cycle (Figure I.3.1.3). Immature stipe binds roughly twice as much iron on the cell surface than mature stipe, but significantly less than blade. In terms of intracellular iron, stipe age appears to have no effect. However, it is known that iron is concentrated in stipe sieve tube exudate (sieve sap) to 5.1 μM- considerably higher than a typical coastal southern California Pacific Ocean seawater concentration of 35 nM

(Manley, 1981) Therefore, whether this is true "uptake" as opposed to translocation of iron originating from the blade is doubtful. A variety of nutrients are assimilated in the blade and transported via the stipe through the water column to compensate for depth-dependent scarcities of nutrients and photons. Furthermore, potential iron chelators such as malate, phosphate, aspartate, and glutamate are common constituents of kelp sieve sap and are thus candidates for the stabilization of iron for long-distance translocation (Schmitz and Srivastava, 1979; Manley, 1981).

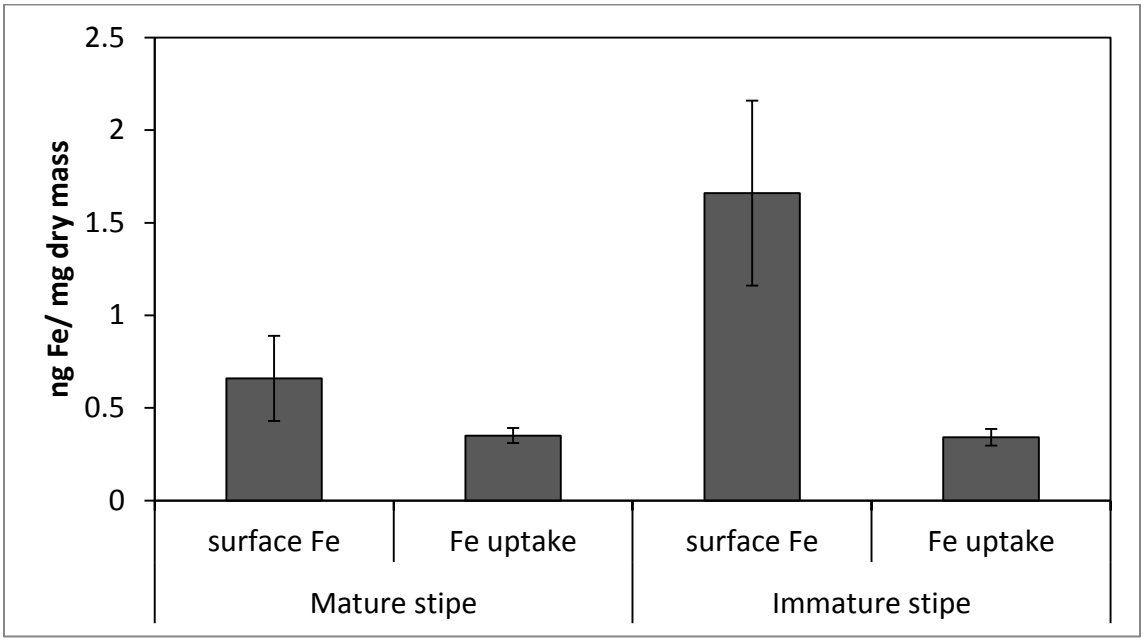

Figure I.3.1.3. Surface-bound vs. intracellular iron in *Macrocystis* stipe as a function of life cycle. Error bars represent ±1 SD from triplicate measurements.

While *Macrocystis* has been shown to bind iron on the cell surface (albeit much less than Ectocarpus, as seen in Figure I.3.1.4), the identity of these iron ligands remains unclear. Fortunately, cell wall composition of *Macrocystis* has been well-defined.

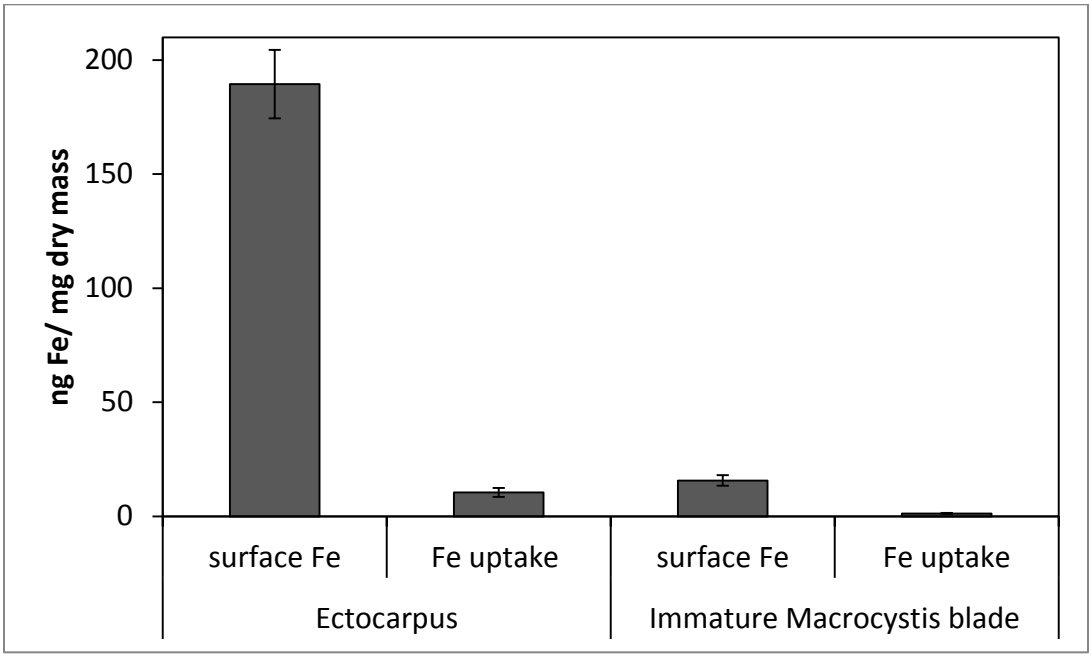

Figure I.3.1.4. Comparison of surface-bound and intracellular iron in immature *Macrocystis* blade with *Ectocarpus* after 24 hour incubation. Error bars represent ±1 SD from triplicate measurements.

Approximately 30 – 40% of the dry mass is the polysaccharide alginate. At seawater pH, each cyclic residue contains one carboxylate side chain (Figure I.3.1.5).

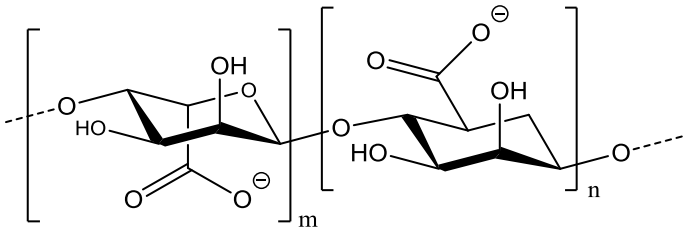

Figure I.3.1.5. Molecular structure of alginate.

Carboxylates are moderately strong iron ligands, depending on the bonding mode. Carboxylate ligands from adjacent alginate chains have the ability to complex a single

iron atom but are limited by sterics. To determine the extent of Fe-carboxylato complexation in immature blades, alginate lyase (alginase) enzymatic digestion was performed on blade tissue. The capacity of cell surface iron-binding after a 24 hour alginase incubation can be seen in Figure I.3.1.6. These results indicate that 96% of surface-bound iron is alginate-associated in immature blades. The effect of enzymatic

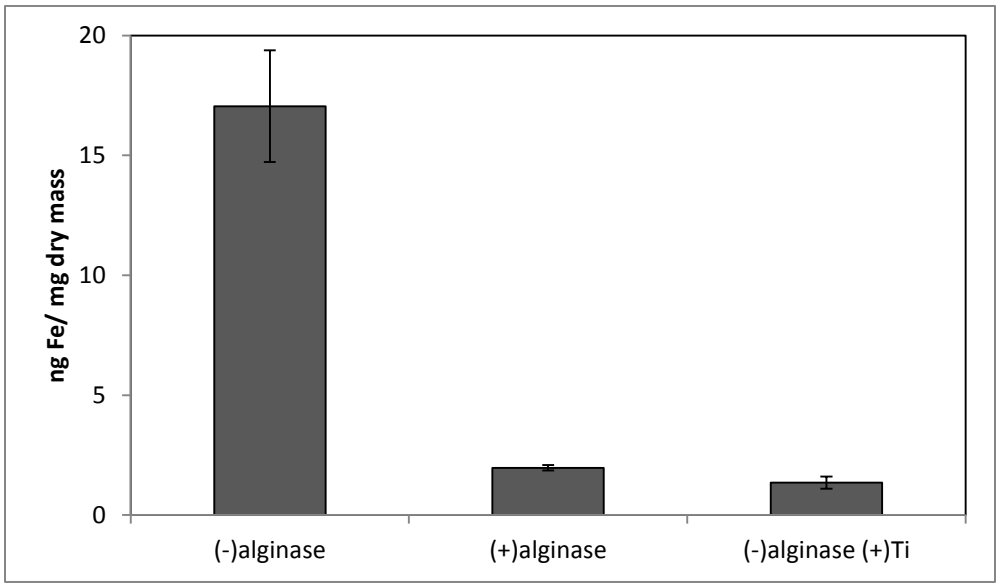

Figure I.3.1.6. Effect of 24 hour enzymatic digestion of immature *Macrocystis* blade by alginase. Error bars represent ±1 SD from triplicate measurements.

digestion in mature blade tissue can be seen in Figure I.3.1.7. These results indicate that 80% of surface-bound iron is alginate-associated in mature blades. This difference between alginate-bound versus total surface-bound iron as a function of life cycle can be attributed to several factors including (but not limited to) differences in mucilaginous covering, microbial digestion, epiphytic digestion, and age-dependent expression levels of alginate synthase.

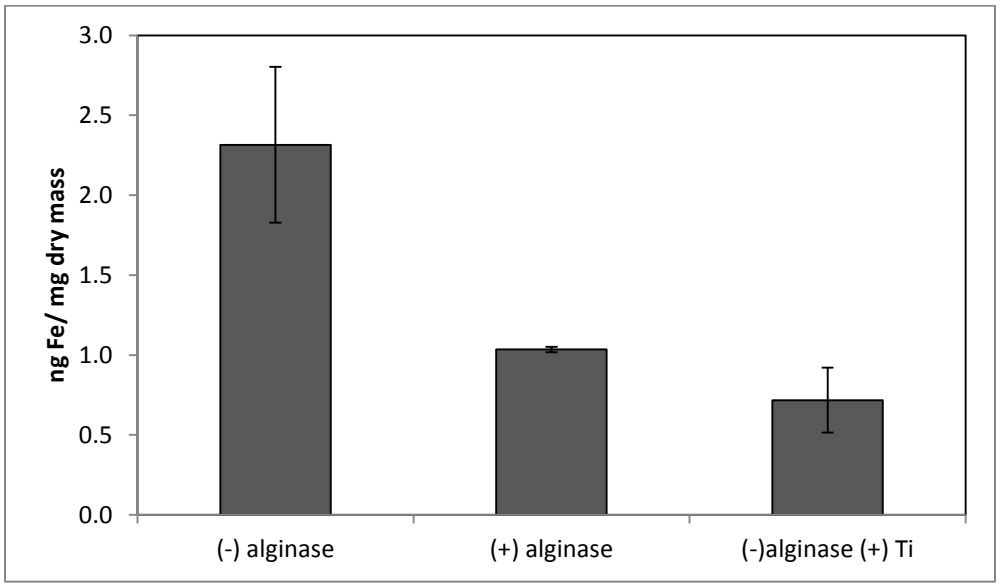

Figure I.3.1.7. Effect of 24 hour enzymatic digestion of mature *Macrocystis* blade by alginase. Error bars represent ±1 SD from triplicate measurements.

Although it was found that the high level of surface binding persisted with *Ectocarpus* until the EDTA to Fe concentration approached 100:1, Macrocystis retained only 30% of the surface-bound iron when the EDTA to Fe concentration approached 10:1 (Figure I.3.1.8). The remaining 30% of surface-bound iron is bound by high affinity ligands which out-compete EDTA even when the EDTA to Fe concentration approached 150:1 at physiological pH. These ligands were not stripped of iron until the powerful reducing reagent Ti(III)-citrate-EDTA was applied.

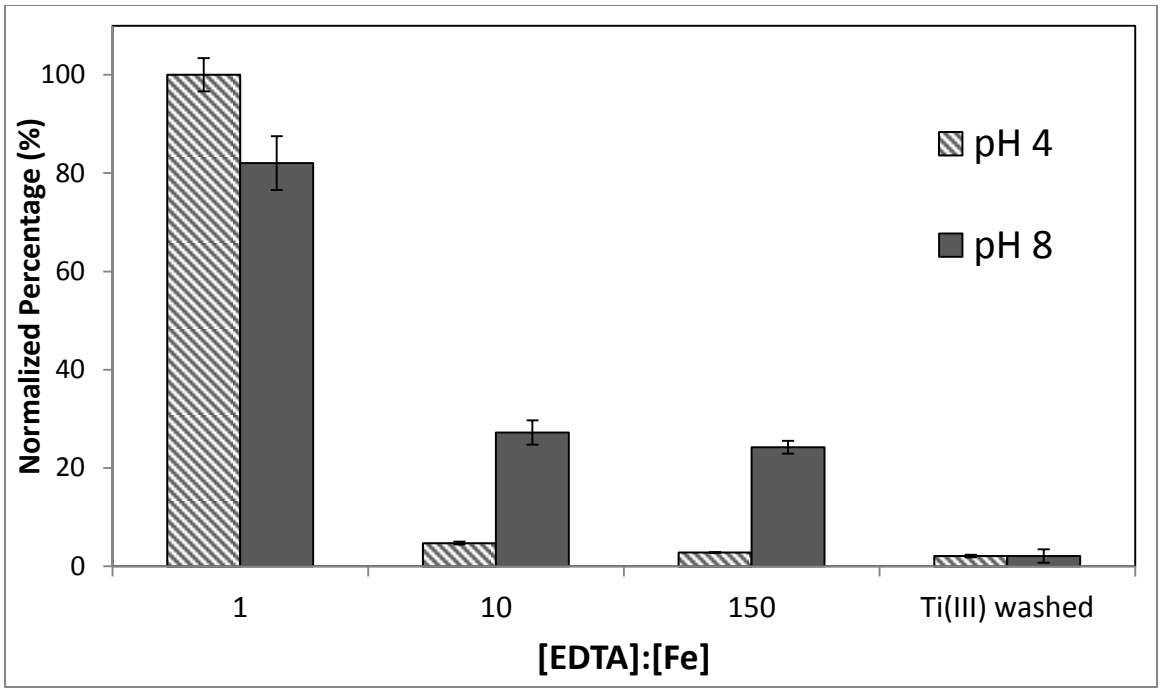

Figure I.3.1.8. Immature *Macrocystis* blade cell surface binding of iron as a function of excess EDTA in growth medium. Error bars represent ±1 SD from duplicate measurements.

Measuring the surface binding from a solution of fixed [^{55}Fe] (1 μM) as a function of [EDTA] and pH allowed us to estimate an effective surface binding constant K'_{eff}. The values obtained were relatively constant (K'_{eff} = 10^{18} M^{-1}) over a wide range (0.1 – 1490 μM) of excess EDTA, confirming a uniform binding and the reliability of the data set. At high pH (8.1), iron binding is very strong (log K'_{eff} = 18) while at acidic pH (4.0) the binding constant is drastically reduced (log K'_{eff} = 12) presumably due to protonation of the alginate carboxylate groups thought to be the major iron binding moieties. The lower value of K'_{eff} relative to *Ectocarpus* may be due to differences in tissue architecture and/or the presence of a fucoidan mucous layer on *Macrocystis* blade surfaces. Fucoidan is a sulfated polysaccharide with several oxygen ligands which could

potentially modulate the bonding mode of the carboxylato ligands giving rise to a weaker iron complex. Alternatively, fucoidan may simply form a physical barrier preventing the iron in seawater from accessing the cell wall.

I.3.1.1.2. Localization of iron on the surface

Microscopic analyses were performed on environmental samples to investigate the spatial distribution and uniformity of iron bound to the cell surface. The iron-specific stain ferrocyanide was lacking in intensity for optical microscopic analysis so the enhancing agent 3,3-diaminobenzidine (DAB) was used in conjunction with ferrocyanide (see section 1.3.1.2.6). This proved effective for detecting extracellular iron but not intracellular iron (Fig. I.2.1.9).

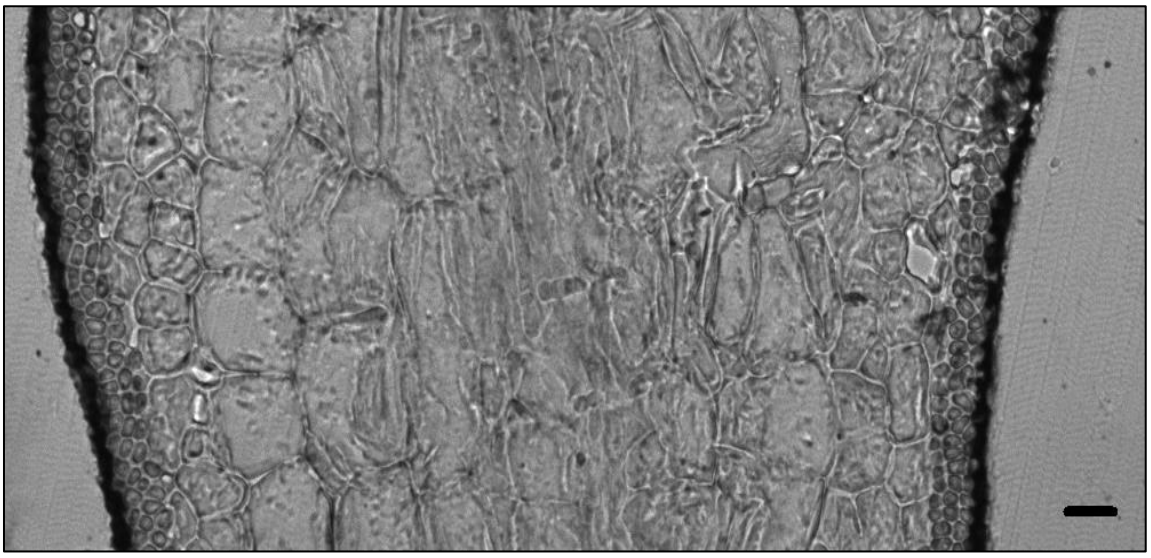

Figure I.3.1.9. DAB staining of environmental sample of immature *Macrocystis* blade. The black regions on the tissue surface represent polyDAB catalyzed by high concentrations of extracellular iron. Scalebar, 20µM.

It is clear that the majority of the iron in samples not washed with the Ti(III) reagent is present on the surface with no internal iron visible in Ti(III) washed samples (Figure I.3.1.10).

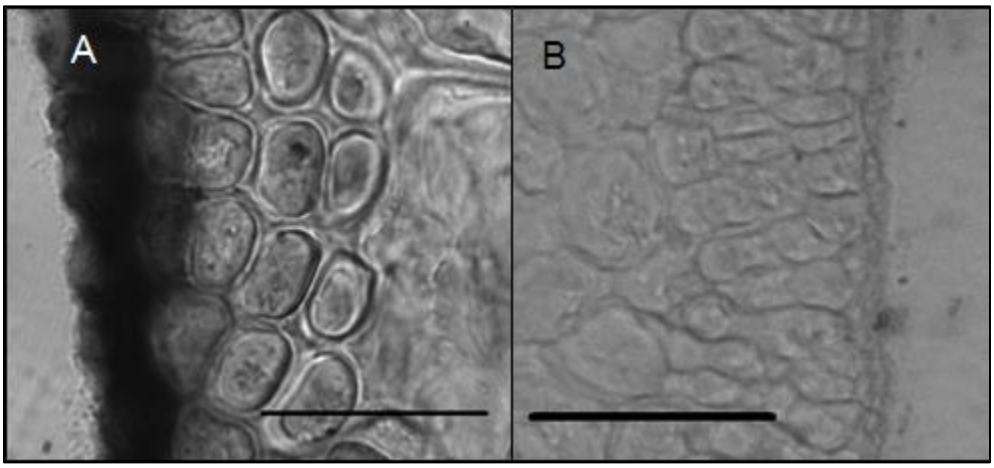

Figure I.3.1.10. DAB staining of environmental sample of immature *Macrocystis* blade. (A) Without Ti(III) wash, and (B) with Ti(III) wash. The black regions in (A) represent polyDAB catalyzed by high concentrations of extracellular iron. Scalebar, 20μM.

While the ferrocyanide-DAB procedure was successful in visualizing extracellular iron in *Macrocystis*, the stain was ineffective for the visualization of internal iron stores. For this reason, the newly reported and highly sensitive iron-specific fluorescent probe MPNBD was synthesized (see Methods I.3.1.2.2) and employed for both intra- and extracellular iron visualization in *Macrocystis* (Park et al., 2014).

In *Macrocystis* blade, intense Fe-MPNBD fluorescence indicates iron concentrated to the meristoderm and to a lesser degree in the apoplast of the cortex (Figure I.3.1.11).

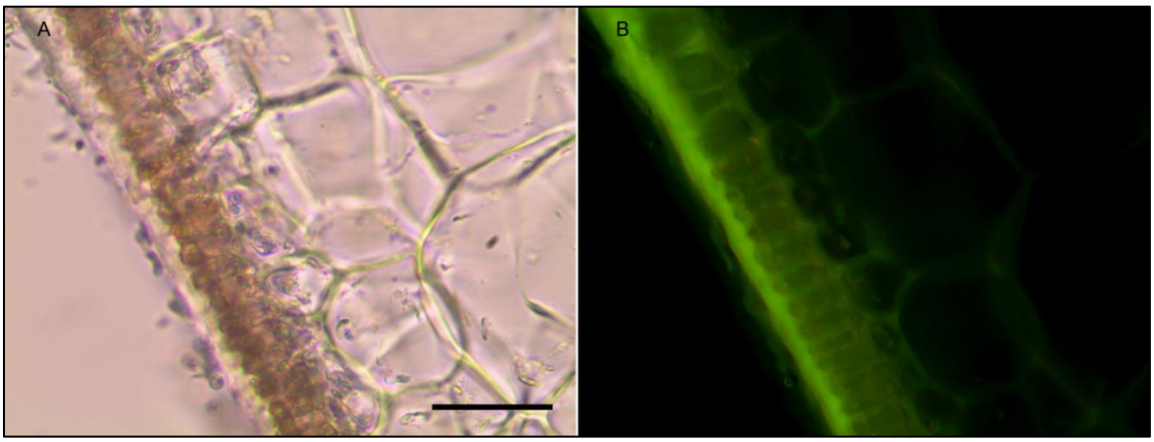

Figure I.2.1.11. Fe-MPNBD fluorescence of environmental sample of immature *Macrocystis* blade. (A) Brightfield transmission image. (B) Green fluorescence on the tissue surface and apoplast represent Fe-MPNBD complexation in areas with high concentrations of iron. Scalebar, 20µM.

Likewise, in *Macrocystis* stipe iron is concentrated mostly to the meristoderm (Figure I.3.1.12). The stipe cortex appears to concentrate iron in the apoplast at a level

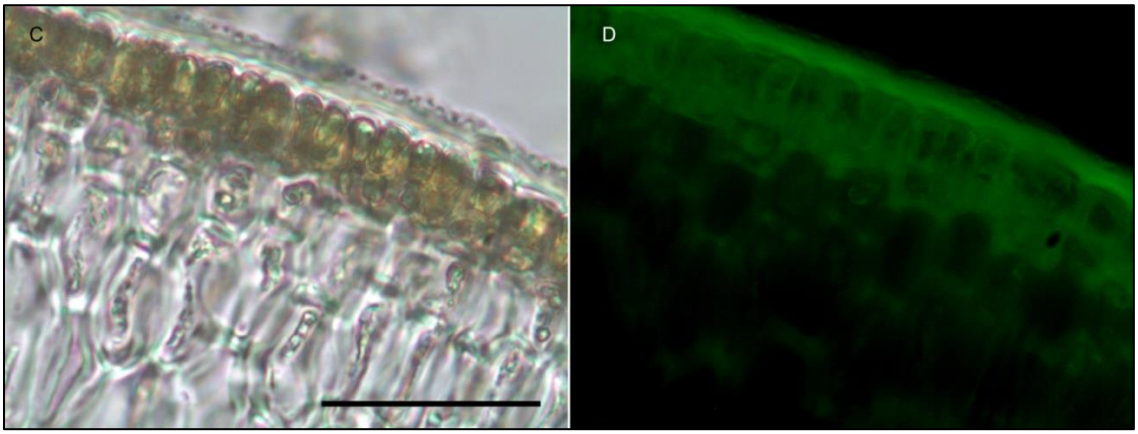

Figure I.3.1.12. Fe-MPNBD fluorescence of environmental sample of *Macrocystis* stipe meristoderm. (C) Brightfield transmission image. (D) Green fluorescence on the tissue surface and apoplast represent Fe-MPNBD complexation in areas with high concentrations of iron. Scalebar, 20µM.

slightly higher than that of blade cortex (Figure I.3.1.13). This may be due to

diffusion/leakage of iron from the medullar sieve cells where iron is concentrated to 150-

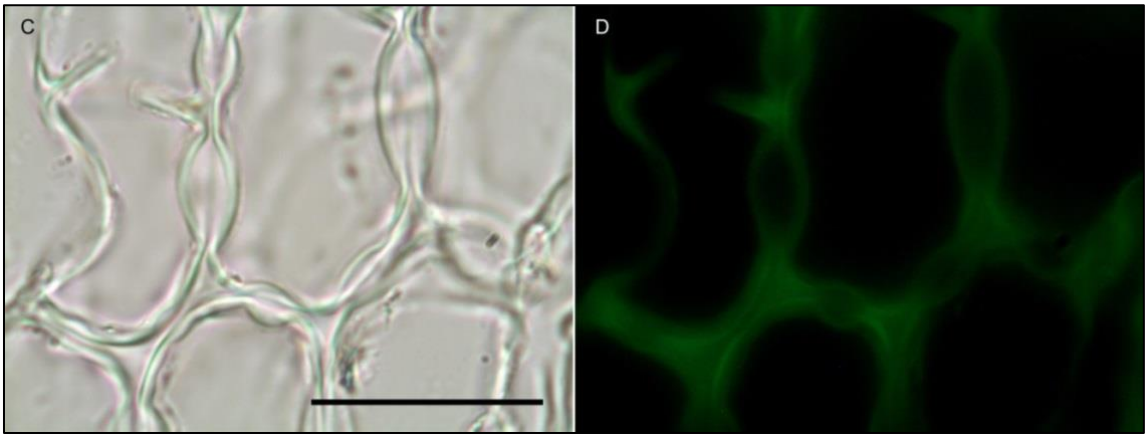

Figure I.3.1.13. Fe-MPNBD fluorescence of environmental sample of *Macrocystis* stipe cortex. (C) Brightfield transmission image. (D) Green fluorescence in the apoplast represent Fe-MPNBD complexation in areas with high concentrations of iron. Scalebar, 40µM.

fold the concentration of seawater. As can be seen in Figure I.3.1.14, a significant amount iron is localized in the medulla. The large sieve cells appear to contain iron in the cell wall, sieve plate pores, and hyphae mitochondria.

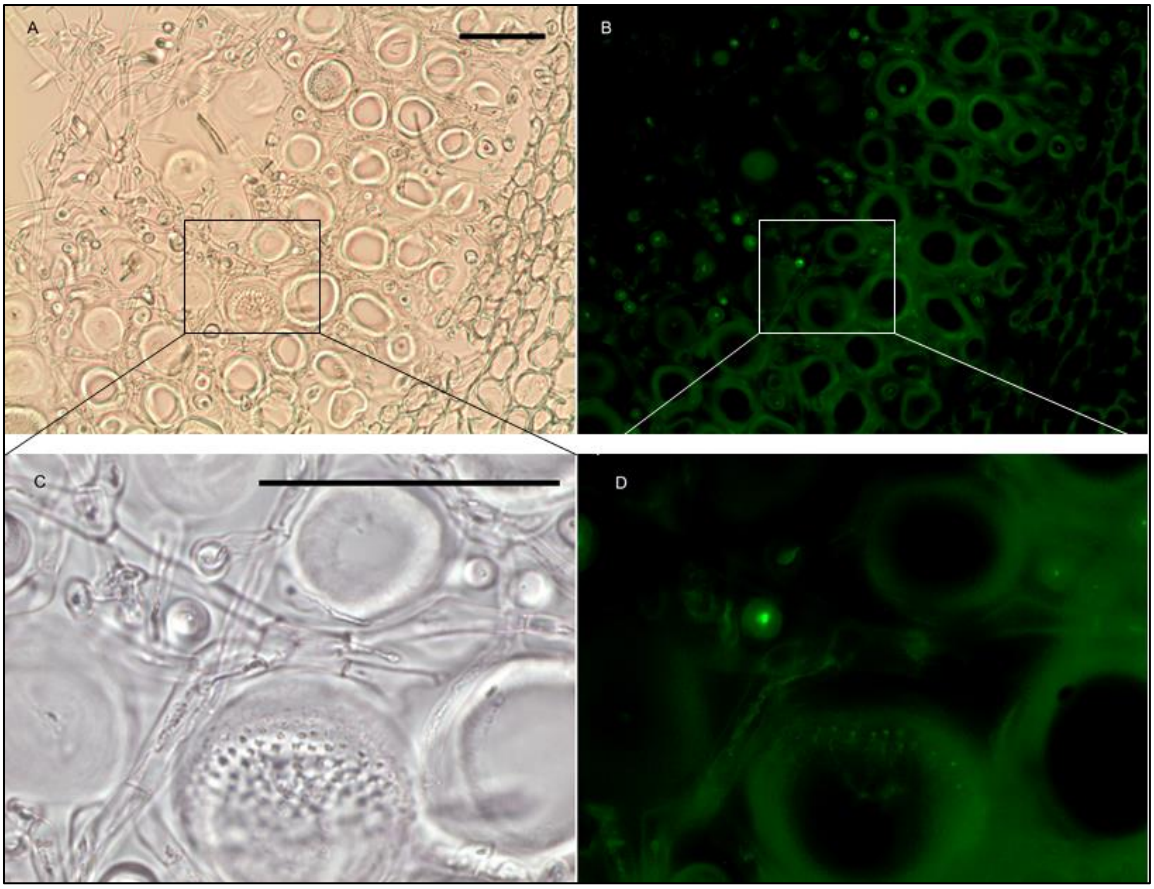

Figure I.3.1.14. Fe-MPNBD fluorescence of environmental sample of *Macrocystis* stipe medulla. (A) Brightfield transmission image. (B) Green fluorescence in the apoplast represent Fe-MPNBD complexation in areas with high concentrations of iron. (C) Brightfield transmission image. (D) Green fluorescence in the hyphae cell and sieve pores represent Fe-MPNBD complexation in areas with high concentrations of iron. Scalebar, 40µM.

Energy dispersive X-ray spectroscopy (EDS) was attempted to confirm the presence of iron. However, the sensitivity of EDS was inadequate for the detection of iron in *Macrocystis*. As can be seen in Figure I.3.1.15, the K_{α} iron signal originating from

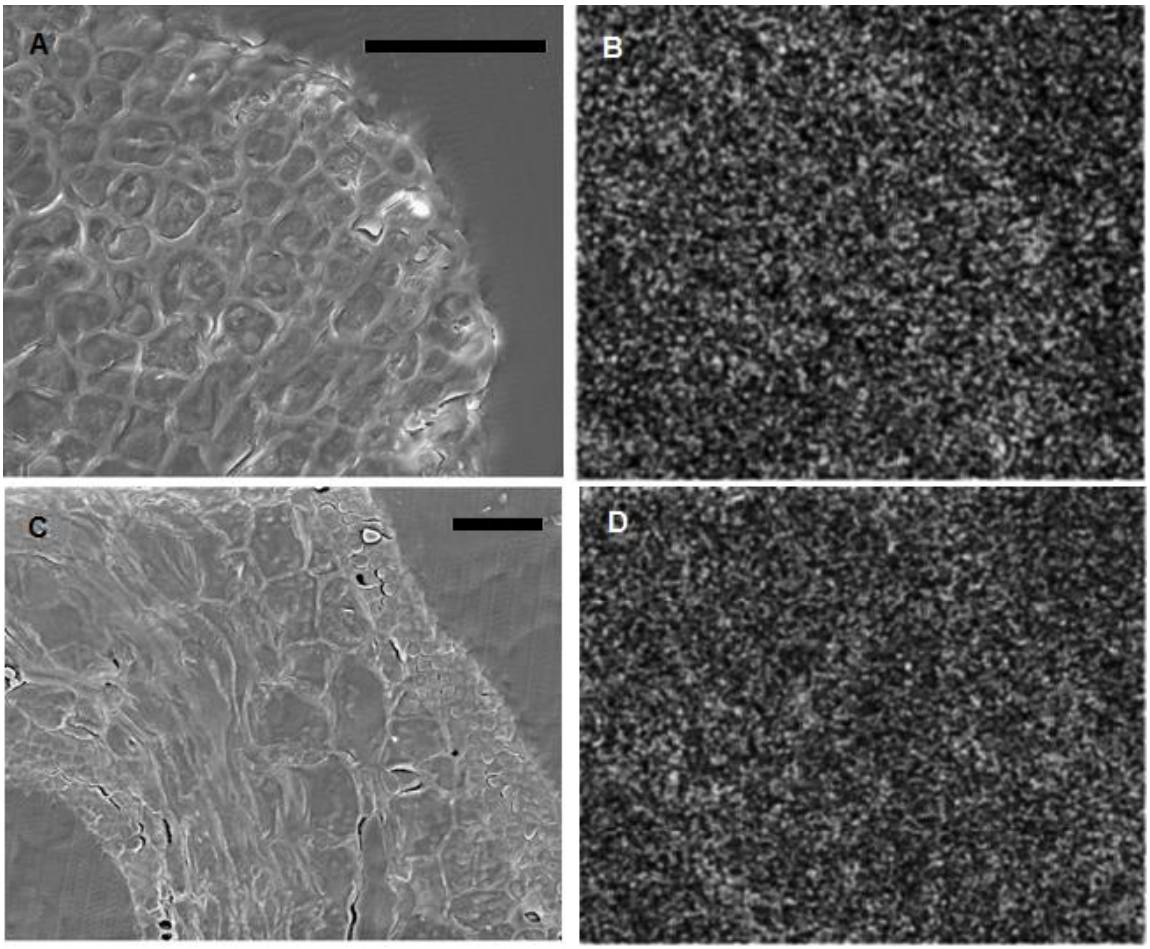

Figure I.3.1.15. EDS of immature environmental *Macrocystis* blade. (A & C) SEM and (B & D) Fe Kα signal of corresponding field. Scalebars, 20µm.

the surface of *Macrocystis* blade is scarcely visible. When taking into consideration the EDS from *Ectocarpus* arising from a much higher surface-binding affinity, this lack of iron signal from *Macrocystis* is hardly surprising.

I.3.1.1.3. Nature of the surface bound iron.

Transmission Mössbauer spectroscopy (TMS) was utilized to determine more precise details of the surface iron and its surrounding ligands. The TMS spectra of a sample of *Macrocystis* grown for 24 hours exposed to 10 µM ^{57}FeEDTA can be seen in

Figure I.3.1.12.

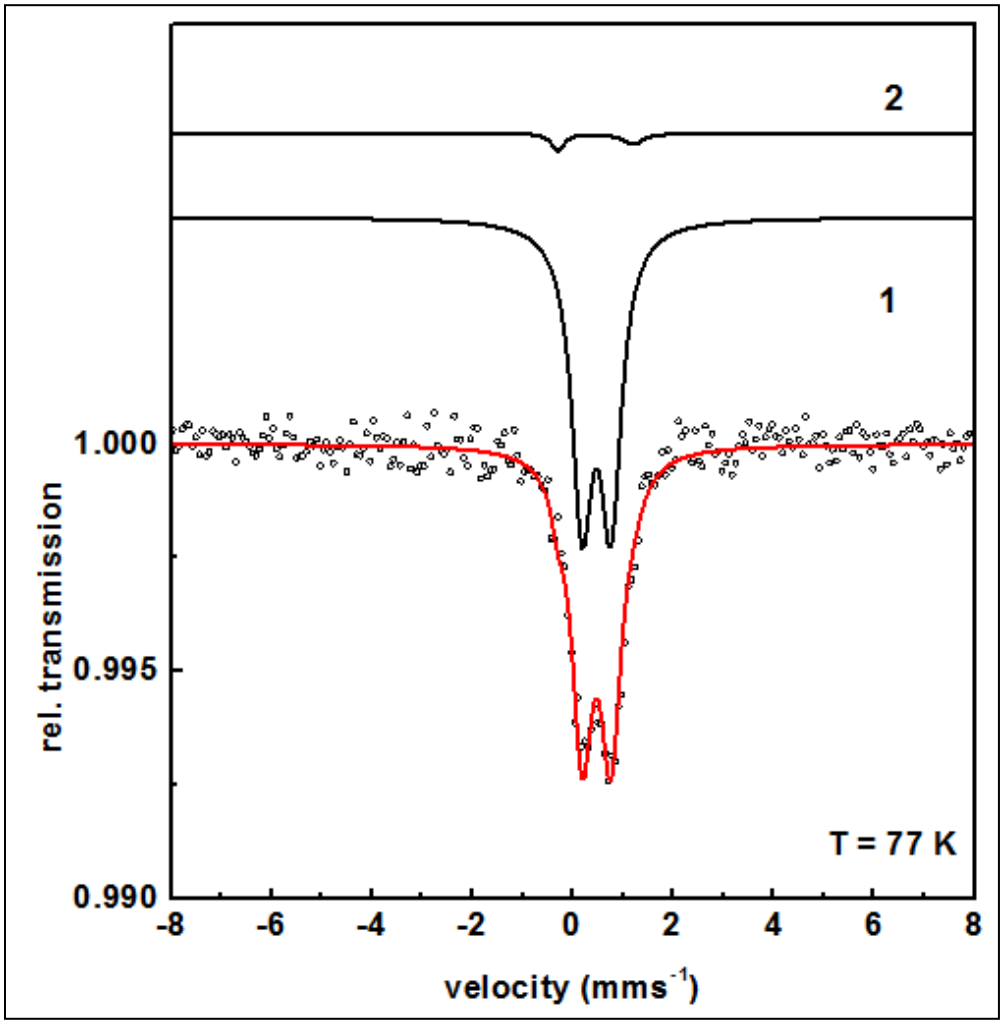

Figure I.3.1.16. TMS of *Macrocystis* blade after 24 hour incubation in ^{57}Fe enriched growth medium. Black circles indicated data points, Species 1 and species 2 are separate components to the overall fit (red line).

The data can be fit with two doublets exhibiting the parameters shown in Table I.2.1. The main component (species 1) has parameters which are typical for polymeric Fe(III) octahedrally coordinated to primarily oxygen ligands and fit into the range observed for carboxylate Fe(III) model complexes (Dziobkowski et al., 1981). The minor species (2)

exhibits parameters consistent with a ferric cytochrome.

Table I.3.1. Mössbauer fit parameters of isomer shift (δ), quadrupole splitting (ΔE_Q), and percentage of absorption area of *Macrocystis* at 77 K.

Species		Parameter	Fitted value
1	$[Fe^{3+}O_6X_n{}^m]^{mn-9}$	δ	0.47 mm/s
		ΔE_Q	0.57 mm/s
		Γ	0.5 mm/s
		Area	93%
2	Fe^{3+} cytochrome	δ	0.45 mm/s
		ΔE_Q	1.5 mm/s
		Γ_1	0.3 mm/s
		Γ_2	0.5 mm/s
		Area	7%

I.3.1.2. Discussion

Until recently, adsorption of iron to the cell surface of marine algae has been viewed as an experimental artifact complicating uptake studies. While it is indeed necessary to remove this signal when quantifying uptake, the potential biological significance of this surface bound iron has generally been ignored. Such was the case for *Ectocarpus* (see section I.2.1) but not in the case of *Macrocystis*. Despite the fact that all the iron present in the media was in the form of the very stable FeEDTA chelate, surface binding persisted even when an excess of EDTA was present. However, the *Macrocystis* cell surface exhibits much weaker and less extensive iron-binding in comparison with *Ectocarpus*- a closely related brown seaweed. Irrespective of the vastly different tissue morphologies of these two species, the cell wall is quite similar on a molecular level.

Alginate comprises 30 – 40% of the dry mass of both species, with carboxylate groups from alginate being the biological iron ligand in *Ectocarpus*. It can be assumed that *Macrocystis* also binds iron on the surface through alginate but the results presented here suggest slightly different binding interactions. Indeed, alginase digestion eliminated nearly all of the bound iron on the surface, suggesting that nearly all of the iron is bound to alginate but the estimate of an effective surface binding constant (K'_{eff}) for Fe(III)′ of between 10^{18} M^{-1} is much weaker than that for *Ectocarpus*.

Histological staining and fluorescence of *Macrocystis* suggests iron is localized on the meristoderm surface in contact with seawater and also the apoplast of the meristoderm and cortex. The significantly higher iron concentration on the meristoderm surface may be due to 1) a more robust alginate cell wall at the meristoderm-seawater interface, or 2) the presence of iron starvation-induced proteins (Isips) purported to reside on the cell surface of diatoms of which homologous genes are found in *Ectocarpus* and (by genetic association) possibly *Macrocystis* (Sutak et al., 2012). However, TMS is more in line with a mineral storage form of iron with parameters more consistent with a polymeric octohedral Fe(III)-oxo/hydroxo center rather than protein ligands. Further spectroscopic studies to determine second coordination sphere ligands of *Macrocystis* were hampered by the low levels of iron found and the correspondingly weak TMS signal.

Taken together, these results imply that surface binding in *Macrocystis* has rather less biological significance, compared to *Ectocarpus*. From a standpoint of surface-bound iron as a function of biomass, it would appear that *Macrocystis* binds much less iron than *Ectocarpus* and thus, requires less buffering of the fluctuating coastal iron concentrations

to meet its metabolic needs of photosynthesis, respiration, etc. However, when taking in to consideration the contrast in cell differentiation and tissue architecture between these two organisms, their respective measured surface-binding capacities align more closely. For example, only meristoderm cells of *Macrocystis* cells are photosynthetic, whereas cortical and sieve cells are essentially void of organelles (Whitton, 1999). This small fraction of photosynthesizing and actively metabolizing cells account for a correspondingly small fraction of the total mass. This may have an effect of skewing the data to appear as though surface-binding is less significant than *Ectocarpus* where each cell is basically homologous. On the other hand, cortical cells have no *a priori* need or means to import the iron bound to their alginate cell walls. Rather, iron localized in the diffusion-limited space of the cortical apoplast may serve a similar buffering function in *Macrocystis* in which alginate-bound iron, regardless of its location, may diffuse through the interconnected apoplastic network to reach the meristoderm and/or mitcochondria-rich hyphae cells (Figure I.3.1.13).

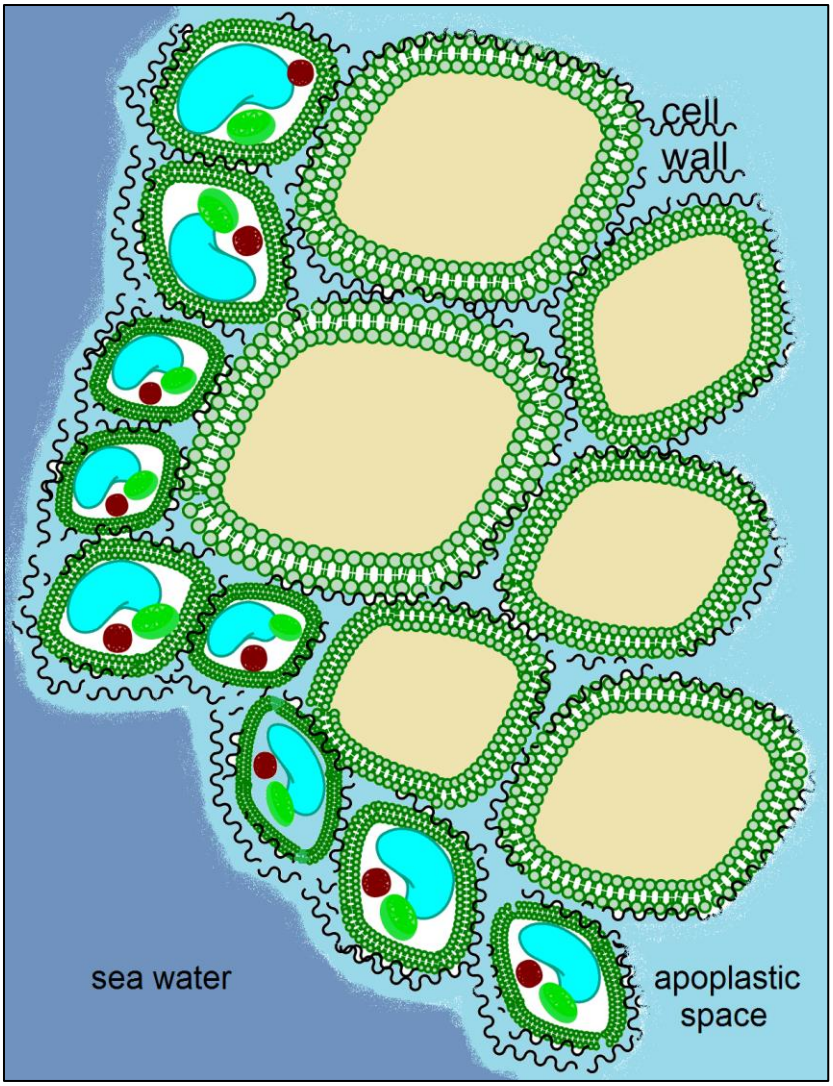

Figure I.3.1.17. Diagram of *Macrocystis* meristoderm (cells with organelles) and cortex (cells without organelles) and the extracellular apoplastic space (light blue regions).

I.3.1.3. Methods

I.3.1.3.1. Algal culture

Macrocystis was harvested from the Point Loma kelp forest (32.7 N, 117.3 W) and either used immediately after collection or maintained in a photobioreactor (New Brunswick Scientific, USA) containing aerated Provasoli-enriched Scripps Pier sea water

(SPSW) at 12 °C under a 14/10 light/dark photocycle.

I.3.1.3.2. Time-dependent and age-dependent surface binding studies

Macrocystis blade and stipe portions were transferred from the photobioreactor to 250 mL culture flasks (Greiner, Germany) containing 10 μM radiolabeled $^{55/56}$FeEDTA (Perkin-Elmer, USA) Provasoli enriched SPSW with ^{56}Fe:^{55}Fe ratio of 48:1. Blade and stipe samples were harvested after 4, 8, and 24 hours for the time-dependent study. Immature and mature blade and stipe samples were harvested after 24 hours for the age-dependent study. *Macrocystis* blade discs and stipe segments were washed with 25 mL ASW, and placed into pre-weighed scintillation vials (Millipore, USA) containing 1 mL of sodium hypochlorite (Fisher Scientific, USA). Vials were then weighed and subtracted to obtain *Macrocystis* mass. Samples were heated at 55°C for 1 hr to eliminate quenching effects originating from chlorophyll. 15mL Hionic Fluor™ scintillation fluid (Perkin-Elmer, USA) was added to each scintillation vial and allowed to dark-adapt for at least 2 hrs in the scintillation counter (Beckman-Coulter LS 6500, USA) to eliminate any background chemiluminesence and phosphorescence prior to counting. Total iron uptake per mg dry *Macrocystis* cells was calculated based on specific activity, measured count rates, scintillation counting efficiency, and biomass measurements. Surface-bound iron was defined as the ^{55}Fe signal of cells not treated with Ti(III)-citrate-EDTA less the internalized iron signal of titanium washed replicates. Control data corresponding to internalized iron was defined as the ^{55}Fe signal of cells treated with Ti(III)-citrate-EDTA (see section I.4 for reagent preparation details).

I.3.1.3.3. Ferrocyanide-diaminiobenzidine (Perls-DAB) staining

Macrocystis was harvested the Point Loma kelp forest (32.7 N, 117.3 W) and blade discs were bored with a coring tool. Discs were fixated in a 0.1 M phosphate buffer solution containing 2% (w/v) paraformaldehyde, 1% (w/v) glutaraldehyde, and 1% (w/v) caffeine for 2 hours. The fixed cells were then washed with 0.1 M phosphate buffer and dehydrated in successive ethanol baths of 30%, 50%, 75%, 85%, 95%, and 100% (3X). The cells were then embedded in 1:1 (v/v) ethanol/LR White resin (EMS) for 3 hours followed by 100% LR White overnight in in gelatin capsules under vacuum. Three micron sections were cut on a Leica EMUC6 microtome and deposited on glass slides. The Perls staining and DAB intensification procedure was performed as described by Meguro et al. (Meguro et al., 2007) and Roschzttardtz et al. (Roschzttardtz et al., 2009). Briefly, sections were incubated on glass slides with equal volumes 4% (v/v) HCl and 4% potassium ferrocyanide (Perls staining solution) for 45 minutes. After washing with distilled H_2O, sections were incubated in a methanol solution containing 0.01 M NaN_3 and 0.3% (v/v) H_2O_2 for 1 hour and then washed with 0.1 M phosphate buffer. DAB intensification was achieved by incubating sections in a 0.1 M phosphate buffer solution containing 0.00025-0.005% (w/v) DAB (Sigma-Aldrich, USA), 0.005% (v/v) H_2O_2, and 0.005% (w/v) $CoCl_2$ for 30 minutes. The sections were then washed with H_2O before imaging with a Zeiss Axiovert 40 (Zeiss, Inc., Germany) inverted microscope.

I.3.1.3.4. 7-(4-methylpiperazin-1-yl)-4-nitrobenzo-2-oxa-1,3-diazole (MPNBD)

Macrocystis was harvested from the Point Loma kelp forest (32.7 N, 117.3 W) and embedded and cryofixed in Tissue-Tek® O.C.T. Compound (Electron Microscopy

Sciences, USA). Cryosections of 50 μm thickness were cut with a Leica EMUC6 cryostat (Leica Biosystems, USA) and placed on well slides. Sections were thawed and then incubated for 5 minutes with a 0.025% working solution of MPNBD in methanol followed by three washes with 0.1 M phosphate buffer (pH 8.1). Wells were then mounted with coverslips and immediately viewed with a Nikon Eclipse TE2000-U inverted microscope (Nikon Imaging, Inc., Japan). The fluorescent dye MPNBD was prepared as described by Park, et. al. (Park et al., 2014). Briefly, 0.357 g (1.785 mmol) 4-chloro-7-nitrobenzofuran (Sigma-Aldrich, USA) was dissolved in 14.3 mL $CHCl_3$ (Sigma-Aldrich, USA). 1-methylpiperazine (0.2 mL, 1.79 mmol) was added and stirred for 1 hour. The solution was concentrated through evaporation for 6 hours. The remaining solution (~5 mL) was purified through a SiO_2 (Sigma-Aldrich, USA) column and eluted with CH_2Cl_2:MeOH = 10:1). The solvent was removed by evaporation overnight. The remaining red powder (~0.25 g) was dissolved in 10 mL MeOH to form a stock solution. Working solutions were prepared by diluting 100-fold with MeOH. 13C-NMR and ^{1}H-NMR spectra were measured on a 500 MHz Varian NMR spectrometer (Varian, USA). Figure I.3.1.18 displays the ^{1}H-NMR spectra in ppm from tetramethylsilane as an internal standard in $CDCl_3$: δ 2.39 (s, 3H), 2.67 (t, 4H), 4.12 (t, 4H), 6.31 (d, 1H), 8.42 (d, 1H).

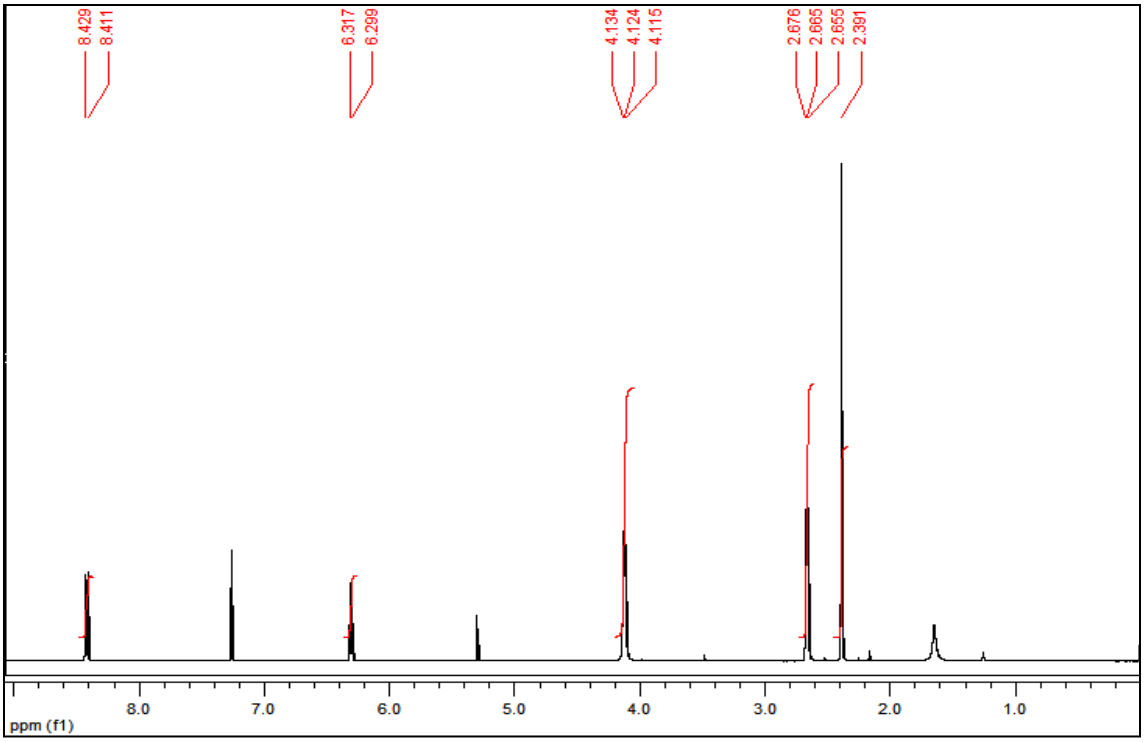

Figure I.3.1.18. ^{1}H-NMR spectrum of MPNBD.

Figure I.3.1.19 displays the ^{13}C-NMR spectra in ppm from tetramethylsilane as an internal standard in $CDCl_3$: δ 45.84, 49.34, 54.56, 102.61, 123.57, 135.15, 144.80, 144.85, 145.20.

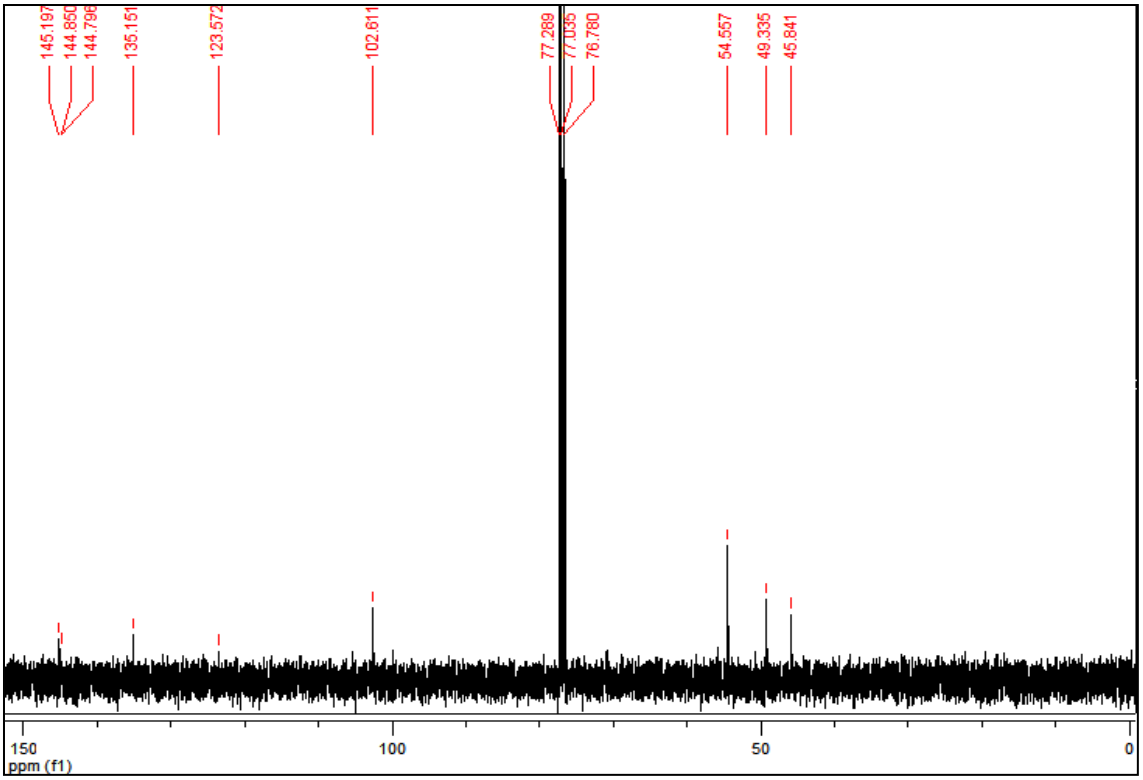

Figure I.3.1.19. ^{13}C-NMR spectrum of MPNBD.

I.3.1.3.5. Energy-dispersive X-ray spectroscopy (EDS)

Macrocystis fronds were harvested from the Point Loma kelp forest (32.7 N, 117.3 W). Blade discs were cut with a coring tool and fixated in a pH 8.1, 0.1 M phosphate buffer solution containing 2% (w/v) paraformaldehyde, 1% (w/v) glutaraldehyde, and 1% (w/v) caffeine for 2 h. The fixed cells were then washed with 0.1 M phosphate buffer and dehydrated in successive ethanol baths of 30, 50, 75, 85, 95, and (3X)100% . The cells were then embedded in 1:1 (v/v) ethanol/LR White resin (Electron Microscopy Sciences, USA) for 3 h followed by 100% LWR overnight in gelatin capsules under vacuum. Sections of 3 µm thickness were cut on a Leica EMUC6 (Leica Biosystems, USA) microtome and deposited on glass slides. Slides were coated with

carbon in a Quorum Technologies Q150T ES sputter coater (Quorum Technologies, United Kingdom). Platinum-coated samples were analyzed under high vacuum in a Quanta 450 FEG environmental scanning electron microscope (FEI, USA) equipped with an Oxford Instruments (Oxford Instruments, United Kingdom) INCA energy dispersive X-ray (EDX) microanalysis system.

I.3.1.3.6. Enzymatic digestion of alginate in Macrocystis blade

Small sections of fresh blade tissue were cut and placed in petri dishes containing 20 mL Provasoli enriched Scripps Pier sea water (SPSW) and 1 mg/mL alginate lyase (Sigma-Aldrich, USA). The petri dish was covered to prevent evaporation and placed on a shaker inside an incubator maintained at 12° C for 24 hours. The medium was then inoculated with radiolabeled $^{55/56}$FeEDTA and allowed to incubate for an additional 24 hours. *Macrocystis* blade discs were harvested, washed with 25 mL ASW, and placed into pre-weighed scintillation vials (Millipore, USA) containing 1 mL of sodium hypochlorite (Fisher Scientific, USA). Vials were then weighed and subtracted to obtain *Macrocystis* mass. Samples were heated at 55°C for 1 hr to eliminate quenching effects originating from chlorophyll. 15mL Hionic Fluor™ scintillation fluid (Perkin-Elmer, USA) was added to each scintillation vial and allowed to dark-adapt for at least 2 hrs in the scintillation counter (Beckman-Coulter LS 6500, USA) to eliminate any background chemiluminesence and phosphorescence prior to counting. Total iron uptake per mg dry *Macrocystis* cells was calculated based on specific activity, measured count rates, scintillation counting efficiency, and biomass measurements. Surface-bound iron was defined as the ^{55}Fe signal of cells not treated with Ti(III)-citrate-EDTA less the

internalized iron signal of titanium washed replicates. Control data corresponding to internalized iron was defined as the ^{55}Fe signal of cells treated with Ti(III)-citrate-EDTA (see section I.4 for reagent preparation details).

I.3.1.3.7. EDTA-cell surface binding competition

An EDTA-cell surface chelate experiment was undertaken by preparing four ^{55}Fe radiolabeled Fe-EDTA stock solutions by adding $^{55}FeCl_3$ (1522 MBq/mL; Perkin-Elmer) to four ^{56}Fe-EDTA solutions (1:1.1, 1:10, 1:150 Fe:EDTA) such that ^{55}Fe: ^{56}Fe equaled ca. 1:48. The stock solutions were allowed to equilibrate for at least 24 hrs prior to use. Six *Macrocystis* cultures with pH adjusted SPSW media (3 at pH 4.0, 3 at pH 8.1) were inoculated with the ^{55}Fe-EDTA solutions to give a final [Fe] of 10 µM. *Macrocystis* blade discs and stipe segments were harvested, washed with 25 mL ASW, and placed into pre-weighed scintillation vials (Millipore, USA) containing 1 mL of sodium hypochlorite (Fisher Scientific, USA). Vials were then weighed and subtracted to obtain *Macrocystis* mass. Samples were heated at 55℃ for 1 hr to eliminate quenching effects originating from chlorophyll. 15mL Hionic Fluor™ scintillation fluid (Perkin-Elmer, USA) was added to each scintillation vial and allowed to dark-adapt for at least 2 hrs in the scintillation counter (Beckman-Coulter LS 6500, USA) to eliminate any background chemiluminesence or phosphorescence prior to counting. Total iron uptake per mg dry *Macrocystis* cells was calculated based on specific activity, measured count rates, scintillation counting efficiency, and biomass measurements. Surface-bound iron was defined as the ^{55}Fe signal of cells not treated with Ti(III)-citrate-EDTA less the internalized iron signal of titanium washed replicates. Control data corresponding to

internalized iron was defined as the ^{55}Fe signal of cells treated with Ti(III)-citrate-EDTA (see section I.4 for reagent preparation details).

I.3.1.3.8. Calculation of the cell surface effective binding constant, K'$_{eff}$

Cell surface iron affinity is expressed as the equilibrium constant K'_{eff} for reaction 1. The objective is to determine the affinity of $[Fe_T^{3+}]_{eq}$ for the cell surface by calculating the equilibrium constant K'_{eff} for Reaction 1 at a specific pH.

$$Cell + [Fe_T^{3+}]_{eq} \leftrightarrows FeCell \qquad (1) \qquad K'_{eff}$$

Fe_T^{3+} in reaction 1 (also known as Fe(III)′) represents the total soluble and unbound aqueous iron(III) in all of its hydrolyzed forms (under our conditions ($Fe(H_2O)_6^{3+}$ + $Fe(H_2O)_5(OH)^{2+}$ + $Fe(H_2O)_4(OH)_2^{+}$ + $Fe_2(H_2O)_8(OH)_2^{4+}$). Cell surface iron affinity constants were estimated by measuring surface bound iron in reaction (1) with varying concentrations of EDTA and varying pH while [Fe(III)] remained fixed at 10 µM. In reaction (2) FeEDTA′ represents the total EDTA/iron(III) species ($FeEDTA^-$ + FeHEDTA + $Fe(OH)EDTA^{2-}$)

We experimentally observe the following reaction (2) between *Cell* and $FeEDTA'$.

$$Cell + FeEDTA' \leftrightarrows FeCell + EDTA' \qquad (2) \qquad K'$$

$$EDTA' = Total\ species\ of\ EDTA\ in\ equilibrium$$

$$= EDTA^{4-} + HEDTA^{3-} + H_2EDTA^{2-} + H_3EDTA^{-} + H_4EDTA + H_5EDTA^{+}$$

$$FeEDTA' = Total\ species\ of\ FeEDTA\ in\ equilibrium$$

$$= FeEDTA^{-} + FeHEDTA + Fe(OH)EDTA^{2-}$$

Relatively constant values were calculated for K'_{eff}at a constant pH over a range of experimental conditions (7 - 20 mg cells exposed to 11 – 1500 μM EDTA in the presence of 10 μM Fe^{3+} at pH 8.1), which confirms the validity of our assumptions and computational approach.

$$[Fe_T^{3+}]_{eq} = Total\ species\ of\ Free\ Fe^{3+} in\ equilibrium$$
$$= Fe(H_2O)_6^{3+} + Fe(OH)^{2+} + Fe(OH)_2^{+} + Fe_2(OH)_2^{4+}$$

K' in Equations 3 through 6 can be corrected for EDTA and FeEDTA speciation using Ringbom

$$K' = \frac{[FeCell][EDTA]'}{[Cell][FeEDTA]'} \qquad (3)$$

$$K' = \frac{[FeCell]}{[Cell][Fe_T^{3+}]_{eq}} X \frac{[Fe_T^{3+}]_{eq}[EDTA]'}{[FeEDTA]'} \qquad (4)$$

$$\beta' = \frac{[FeEDTA]'}{[Fe_T^{3+}]_{eq}[EDTA]'} \qquad (5)$$

$$K' = \frac{K'_{eff}}{\beta'} \qquad (6)$$

coefficients[1] to obtain K (Equation 10) for Reaction 7. FeCell and Cell represents all protonated forms.

$$Cell + FeEDTA^{-} \quad \leftrightarrows \quad FeCell + EDTA^{4-} \qquad (7) \quad K$$

$$K = \frac{[FeCell][EDTA^{4-}]}{[Cell][FeEDTA^{-}]} \qquad (8)$$

$$K' = \frac{[FeCell][EDTA^{4-}]\alpha_{EDTA}}{[Cell][FeEDTA^{-}]\alpha_{EDTA}} \qquad (9)$$

$$K = \frac{K'\alpha_{FeEDTA}}{\alpha_{EDTA}} \qquad (10)$$

Equations 3 through 10 were obtained considering the equilibrium between the Cell and $FeEDTA'$ (Reaction 2) where K' is the equilibrium constant for the Reaction 2 at a specific pH. K'_{eff} is the effective binding constant for the cell and $[Fe_T^{3+}]_{eq}$ according to equilibrium Reaction 1.

Iron uptake by cells was monitored in the presence of varying concentrations of EDTA at a constant iron concentration. The amount of cells used in each experiment was also varied over a wide range (7 - 20 mg). All relevant experimental data are summarized in Table I.3.2. Calculated equilibrium concentrations are summarized in Table I.3.3. Ringbom coefficients for iron, EDTA and FeEDTA were calculated using equations 11

Table I.3.2. Experimental data used for calculations of equilibrium concentrations.

Expt.	pH	$[Fe]_{Init}$ / µM	$[EDTA]_{Init}$ / µM	$[Cell]_{Init}$ / mg	Fe uptake ng Fe/mg cell
1	8.1	10	11	12.125	48.363
2	8.1	10	11	14.375	56.104
3	8.1	10	100	9.75	15.606
4	8.1	10	100	11.375	19.108
5	8.1	10	1500	6.375	16.373
6	8.1	10	1500	7.125	14.497
7	4.0	10	11	13.625	66.056
8	4.0	10	11	19.875	61.268
9	4.0	10	100	14.625	2.83
10	4.0	10	100	13.75	3.212
11	4.0	10	1500	8.375	1.823
12	4.0	10	1500	10.875	1.772

Table I.3.3. Parameters used for calculating the reaction between Cell and FeEDTA.

Expt.	pH	$[FeCell]_{eq}$ /mg	$[Cell]_{eq}$ /mg	$[EDTA]'_{eq}$ /μM	$[FeEDTA]'_{eq}$ /μM
1	8.1	0.000586	12.12	1.58	9.42
2	8.1	0.000695	14.37	1.68	9.32
3	8.1	0.000183	9.75	90.22	9.78
4	8.1	0.000245	11.37	90.27	9.73
5	8.1	0.000104	6.37	1490.15	9.85
6	8.1	0.000103	7.12	1490.15	9.85
7	4.0	0.000900	13.62	1.86	9.14
8	4.0	0.001218	19.87	2.15	8.85
9	4.0	0.000041	14.62	90.09	9.91
10	4.0	0.000044	13.75	90.09	9.91
11	4.0	0.000015	8.37	1490.07	9.93
12	4.0	0.000019	10.87	1490.07	9.93

through 24. β' obtained using Ringbom coefficients are also presented in Table I.3.4.

Table I.3.4. Ringbom coefficients calculated for the equilibrium between Fe^{3+} and EDTA and the equilibrium constant β'.

pH	[EDTA:Fe]	α_{EDTA}	α_{FeEDTA}	$\alpha_{Fe(OH)}$	β′
8.1	1.1	79.65	24.62	5.58E+10	7.44E+23
	10	85.13	23.33	4.89E+10	7.81E+21
	150	98.78	16.56	9.33E+09	9.39E+20
4	1.1	6.61E+06	0.68	830	1.19E+17
	10	7.19E+07	0.89	212	8.31E+16
	150	8.80E+09	1.44	6.1	6.94E+16

Affinity constants calculated using equilibrium concentrations and Ringbom coefficients are given in Table I.3.5.

Table I.3.5. Binding constants (*K', K, and K'$_{eff}$*) for the reaction between cell and FeEDTA.

Expt.	*K'*	Average *K'*	*K*	Average *K*	$[Fe_T^{3+}]_{eq}$	*K'$_{eff}$*	Average *K'$_{eff}$*
1	8.11E-06	8.41E-06	2.51E-06	2.60E-06	8.01E-24	6.04E+18	6.26E+18
2	8.70E-06		2.69E-06		7.47E-24	6.48E+18	
3	1.73E-04	1.86E-04	4.73E-05	5.10E-05	1.39E-23	1.35E+18	1.45E+18
4	2.00E-04		5.47E-05		1.38E-23	1.56E+18	
5	2.48E-03	2.33E-03	4.15E-04	3.91E-04	7.04E-24	2.33E+18	2.19E+18
6	2.19E-03		3.68E-04		7.04E-24	2.06E+18	
7	1.35E-05	1.42E-05	1.38E-12	1.46E-12	4.13E-17	1.60E+12	1.68E+12
8	1.49E-05		1.53E-12		3.47E-17	1.77E+12	
9	2.57E-05	2.75E-05	3.19E-13	1.62E-13	1.32E-18	2.14E+12	2.28E+12
10	2.92E-05		4.78E-15		1.32E-18	2.43E+12	
11	2.74E-04	2.70E-04	4.48E-14	4.41E-14	9.60E-20	1.90E+13	1.87E+13
12	2.66E-04		4.35E-14		9.60E-20	1.85E+13	

$$EDTA + nH \quad \leftrightarrows \quad H_nEDTA \qquad (11)$$

$$\beta_n^H = \frac{[H_nEDTA]}{[EDTA][H]^n} \qquad (12)$$

$$[EDTA]' = \alpha_{EDTA}\,[EDTA^{4-}] \qquad (13)$$

$$\alpha_{EDTA} = 1 + \beta_1^H[H] + \beta_2^H[H]^2 \ldots\ldots\ldots + \beta_5^H[H]^5 \qquad (14)$$

Successive log $\beta_n^H (n = 1-5)$ values (10.19, 16.32, 19.01, 21.01, and 22.51) were calculated from protonation constants for EDTA.

$$EDTA^{4-} + Fe^{3+} \quad \leftrightarrows \quad FeEDTA^- \qquad (15) \quad \beta_{110}$$

$$FeEDTA^- + H^+ \quad \leftrightarrows \quad FeHEDTA \qquad (16) \quad K_1$$

$$Fe(OH)EDTA^{2-} + H^+ \quad \leftrightarrows \quad FeEDTA^- \qquad (17) \quad K_2$$

$$\beta_{110}^{FeEDTA} = \frac{[EDTA^-]}{[Fe_{aq}^{3+}][EDTA^{4-}]} \qquad (18)$$

$$[FeEDTA]' = \alpha_{FeEDTA}\,[FeEDTA^-] \qquad (19)$$

$$\alpha_{FeEDTA} = 1 + K_1[H^+] + 1/(K_2[H^+]) \qquad (20)$$

Log β and K values used in the calculation of α_{FeEDTA} were ($\beta_{110} = 25.1$, $K_1 = 1.3, K_2 = 7.37$) for FeEDTA.

$$Fe(H_2O)_6^{3+} + OH^- \quad \rightleftarrows \quad Fe(OH)^{2+} \qquad (21) \quad K_1$$

$$Fe(H_2O)_6^{3+} + 2OH^- \quad \rightleftarrows \quad Fe(OH)_2^{2+} \qquad (22) \quad K_2$$

$$[Fe_T^{3+}]_{eq} = [Fe(H_2O)_6^{3+}]\, X\, \alpha_{Fe(OH)} \qquad (23)$$

$$\alpha_{Fe(OH)} = 1 + K_1[OH] + K_2[OH]^2 \qquad (24)$$

Formation of $Fe_2(OH)_2^{4+}$ depends on the concentration of Fe^{3+}. In most calculations, the concentration of Fe^{3+} is less than $10^{-3.7}$M. Therefore, $\alpha_{Fe(OH)}$ can be calculated neglecting $Fe_2(OH)_2^{4+}$. Log K_1 and K_2 are 11.0 and 21.7 respectively.

I.3.1.3.9. Transmission Mössbauer spectroscopy (TMS)

Macrocystis fronds were harvested from the Point Loma kelp forest and then cultured in for 1 week in oligotrophic open Pacific Ocean sea water (~4 nM Fe) to remove adventitious ^{56}Fe from the cell surface. Blades were then transferred to 10 μM ^{57}FeEDTA enriched Scripps Pier sea water (SPSW) for 24 hours. These blades were then lyophilized and packed in to Delrin® Mössbauer sample holders and weighed. The Mössbauer spectra were recorded in the transmission geometry using a constant acceleration spectrometer operated in conjunction with a 512-channel analyzer in the time-scale mode. The detector consisted of a proportional counter filled with argon-krypton-xenon. The source was at room temperature. The spectrometer was calibrated against α-iron at room temperature (RT). For measurements at 77K, samples were placed

in a continuous-flow cryostat (Oxford Instruments, United Kingdom). Spectral data were transferred from the multi-channel analyzer to a PC for further analysis employing the public domain Vinda program on an Excel 2003® platform (Microsoft, USA). Isomer shift δ, quadrupole splitting ΔE_Q, line width Γ and percentage of the total absorption area were obtained by least-squares fits of Lorentzian lines to the experimental spectra. All values are rounded to the last given digit. The isomers shifts, the quadrupole splitting and the line width are given in mm/s. The relative area is given in parts per hundreds.

I.3.2. Iron Storage in *Macrocystis pyrifera*

I.3.2.1. Results

Microscopic and spectroscopic studies focusing on iron storage are challenging for organisms that have evolved efficient iron uptake strategies and consequently store little of this element. *Macrocystis* is one such organism with internal iron concentrations below the detection limit of light microscopy, X-ray fluorescence (EDS), and X-ray absorption spectroscopy (XAS). Thus, in this study methodologies are limited to fluorescence microscopy and transmission Mössbauer spectroscopy (TMS).

Fe-MPNBD fluorescence in meristoderm cells revealed iron localized in areas uncharacteristic of any known iron storage strategies. Despite being concentrated to a large organelle resembling a vacuole- a storage strategy employed by the higher plant *Arabidopsis* and recently suggested for *Ectocarpus* (see section I.2.3)- the localization to the perimeter of these organelles while not distinctly inside the organelle (see arrows in Figure I.3.2.1) raises concerns as to the utility of visualizing iron stores with MPNBD fluorescence in *Macrocystis*. Without genomic data, assigning this fluorescence to the

vacuolar transport protein homologs VIT1 and NRAMP as in *Ectocarpus* would be purely speculative.

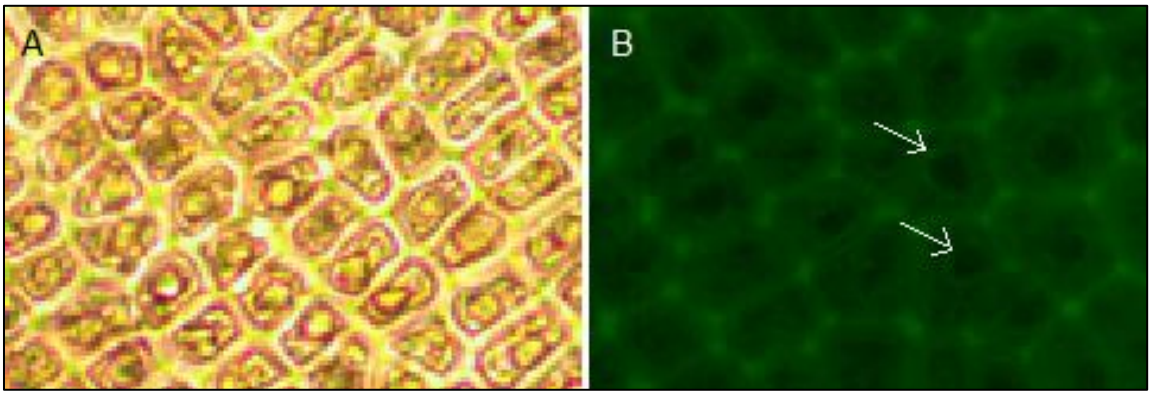

Figure I.3.2.1. Fe-MPNBD fluorescence of *Macrocystis* blade meristoderm grown for 21 days on 10 µM FeEDTA enriched culture medium. (C) Brightfield transmission image. (D) Green fluorescence represent Fe-MPNBD complexation in areas with high concentrations of iron. Arrows indicate possible intracellular iron stores. Scalebar, 20µM.

The most sensitive technique available in this study for the detection and characterization of mineralized iron is TMS. After long-term (21 days) incubation in ^{57}FeEDTA enriched culture medium, TMS spectra exhibiting sufficient resonance absorption were obtained which display a single quadrupole doublet-like feature (Figure I.3.2.2). Since the blade material was thoroughly washed with the Ti(III)-citrate-EDTA reagent, the presence of iron on the algal surfaces can be excluded and therefore, the iron components observed by TMS are genuinely of intracellular origin. From this, it can be concluded, that ^{57}Fe supplied as EDTA complex in the medium is transported into, and

metabolized inside, cells of *Macrocystis*. A low percentage (<0.2%) of the TMS signal experienced resonant absorption with the ^{57}Fe Mössbauer nucleus. A single iron compound detected by TMS displays a spectrum typical of a polymeric ($Fe^{3+}O_6$) system. (Figure I.3.2.2, Table I.3.2).

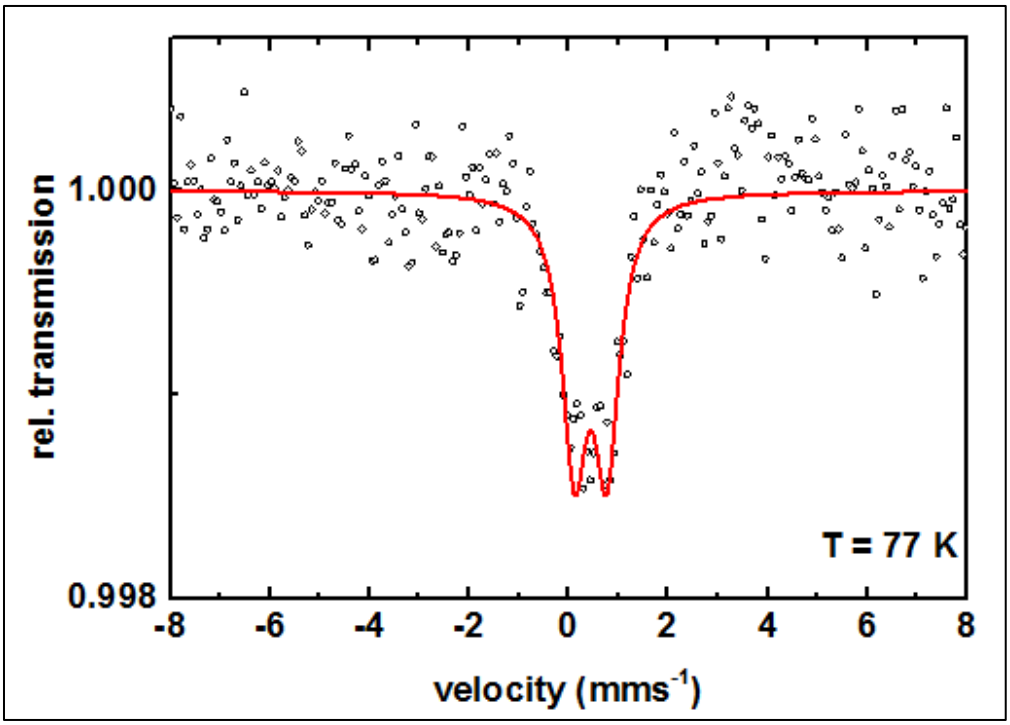

Figure I.3.2.2. TMS of *Macrocystis* blade grown for 21 days on 10 µM ^{57}Fe enriched culture medium. Black circles represent data points and red line represents the fit to the data points.

Table I.3.6. Mössbauer fit parameters of isomer shift (δ), quadrupole splitting (ΔE_Q), and percentage of absorption area of *Macrocystis* at 77 K.

Species		Parameter	Fitted value
1	$[Fe^{3+}O_6X_n{}^m]^{mn-9}$	δ	0.44 mm/s
		ΔE_Q	0.65 mm/s
		Γ	0.6 mm/s

Due to this weak signal at 77 K, low temperature TMS was below the detection limit, attributable to the doublet splitting into a sextet and an accompanying decrease in peak intensity when a polymeric iron species is present (data not shown). Polymeric biological ($Fe^{3+}O_6$) systems found by *in situ* Mossbauer spectra very often represent the mineral cores of ferritins. The Mössbauer spectroscopic features of such systems are strongly temperature and size dependent reflecting superparamagnetic relaxation of magnetic nanoparticles (Mørup, 2011). In lieu of an approximate blocking temperature, the relative degree of crystallinity and particle size of the mineral phase cannot be determined. However, based on the similarity of parameters with the TMS of *Ectocarpus,* it can be inferred that *Macrocystis* has a similar mineral core.

I.3.2.2. Discussion

In light of the *Ectocarpus* TMS data reported for long-term ^{57}Fe incubation, it is scarcely surprising *Macrocystis* lacks an observable ferrous iron pool- a common strategy for various bacterial, fungal, plant and algal systems (Böhnke and Matzanke, 1995; Winkelmann and Carrano, 1997; Semin et al., 2003; Matzanke et al., 2004; Kovács et al., 2006; Kovács et al., 2009). Thus, despite the fact that the iron is likely transported across the cell membrane as Fe(II) (Manley, 1981), it must be relatively rapidly reoxidized to Fe(III) and stored in that form. The vast majority of organisms store iron in one or more of the various forms of the ubiquitous protein ferritin. However, by genetic proximity to *Ectocarpus*, the presence of ferritin in *Macrocystis* is unlikely. In the absence of ferritins two alternate or additional forms of iron storage have been identified in other organisms. The first, found in some fungi, is a siderophore based storage system (Matzanke et al.,

1987; Matzanke et al., 1988) clearly not present here. The second, which has been elucidated in yeast and several other eukaryotes including the halotolerant alga *Dunaliella salina* is a vacuole based one (Martinoia et al., 2007; Paz et al., 2007). At present, there is little data in the literature about the chemical nature of vacuole sequestered iron stores. However, it seems likely that the iron would be stored in some sort of mineral phase. Indeed it is reported that in *Arabidopsis* seeds some iron is located in vacuole globoids containing phytate which may bind ferric ions via phosphate groups (Lanquar et al., 2005).

Since the spectroscopic parameters and relaxation properties (i.e. magnetic ordering temperatures) of condensed iron mineral phases are strongly dependent on particle sizes and their crystalline/amorphous structure, detailed temperature dependent Mössbauer measurements can shed light on the nature of any iron stores. Unfortunately, the weak signal from *Macrocystis* hinders these measurements and also XAS experiments. However, it can be deduced with reasonable confidence that *Macrocystis* stores iron in a mineral phase similar to that found in *Ectocarpus*. Whether this mineral phase is crystalline or amorphous, phosphate rich or poor, and the the subcellular location remains to be determined. Work geared towards more fully characterizing this system using the more intense synchrotron beam as a Mössbauer source is continuing.

I.3.2.3. Methods

I.3.2.3.1. 7-(4-methylpiperazin-1-yl)-4-nitrobenzo-2-oxa-1,3-diazole (MPNBD)

Macrocystis was harvested from the Point Loma kelp forest (32.7 N, 117.3 W) and embedded and cryofixed in Tissue-Tek® O.C.T. Compound (Electron Microscopy

Sciences, USA). Cryosections of 30 μm thickness were cut with a Leica EMUC6 cryostat (Leica Biosystems, USA) and placed on well slides. Sections were thawed and then incubated for 5 minutes with a 0.025% working solution of MPNBD in methanol followed by three washes with 0.1 M phosphate buffer (pH 8.1). Wells were then mounted with coverslips and immediately viewed with a Nikon Eclipse TE2000-U inverted microscope (Nikon Imaging, Inc., Japan). The fluorescent dye MPNBD was prepared as described by Park, et. al. (Park et al., 2014). See section I.3.1.3.4 for synthesis and characterization details.

I.3.2.3.2. Transmission Mössbauer spectroscopy (TMS)

Macrocystis fronds were harvested from the Point Loma kelp forest (32.7 N, 117.3 W) and then cultured in ^{57}FeEDTA enriched Scripps Pier sea water (SPSW) in a photobioreactor (New Brunswick Scientific, USA) for 21 days. Blades were then washed with Ti(III)-citrate-EDTA reagent and then rinsed thoroughly with SPSW in order to remove adventitious iron from the extracellular cell surface (see section I.4 for reagent preparation details). These blades were then lyophilized and packed in to Delrin® Mössbauer sample holders and weighed. The Mössbauer spectra were recorded in the transmission geometry using a constant acceleration spectrometer operated in conjunction with a 512-channel analyzer in the time-scale mode. The detector consisted of a proportional counter filled with argon-krypton-xenon. The source was at room temperature. The spectrometer was calibrated against α-iron at room temperature (RT). For measurements at 77K, samples were placed in a continuous-flow cryostat (Oxford Instruments, United Kingdom). Spectral data were transferred from the multi-channel

analyzer to a PC for further analysis employing the public domain Vinda program on an Excel 2003® platform (Microsoft, USA). Isomer shift δ, quadrupole splitting ΔE_Q, line width Γ and percentage of the total absorption area were obtained by least-squares fits of Lorentzian lines to the experimental spectra. All values are rounded to the last given digit. The isomers shifts, the quadrupole splitting and the line width are given in mm/s. The relative area is given in parts per hundreds.

I.4. Appendix

Titanium(III)-citrate-EDTA reagent

A Ti(III)-citrate-EDTA reagent was prepared according to Hudson and Morel (Hudson and Morel, 1989) to remove extracellular iron from *Ectocarpus* and *Macrocystis*. Briefly, water was deoxygenated through boiling, allowed to cool, and the following solids were dissolved such that citrate [0.047 M], EDTA [0.047 M], NaCl [0.35 M], KCl [0.01 M]. The pH was adjusted to ca. 8 with NaOH and then 7.77 mL 20% $TiCl_3$ giving [0.047 M] Ti(III). The pH was again adjusted with NaOH dropwise to pH 8.1 and the final reagent was stored in a drybox until further use. The Ti(III)-citrate-EDTA reagent was applied to the *Ectocarpus* and Macrocystis samples after rinsing with ASW. 5 mL of the reagent was added to the algal tissue and allowed to incubate for 2 min. It was removed by decanting or vacuum filtration followed by a 25 mL wash with ASW.

I.5. Acknowledgements

We thank Prof. Kathy Barbeau, SIO/UCSD and her students for determining the iron content of our Scripps Pier water, and DESY, Hamburg for access to their

infrastructure (DORIS III beamline at HASYLAB) making possible our EXAFS experiments, and Dr. Steve Barlow, SDSU Microscopy Center for help with the histochemistry and microscopy.

Chapter I, in part, is a reprint of the material as it appears in the Journal of Experimental Botany, 2012, Böttger, Lars H.; Miller, Eric P.; Andresen, Christian; Matzanke, Berthold F.; Küpper, Frithjof C.; Carrano, Carl J. The dissertation author was the second author of this paper.

Chapter I, in part, is a reprint of the material as it appears in the Journal of Experimental Botany, 2014, Miller, Eric P.; Böttger, Lars H.; Weerasinghe, Aruna J.; Crumbliss, Alvin L.; Matzanke, Berthold F.; Meyer-Klaucke, Wolfram; Küpper, Frithjof C.; Carrano, Carl J. The dissertation author was the primary investigator and author of this paper.

II. Boron Uptake, Localization, and Speciation in *Ectocarpus siliculosus* and *Macrocystis pyrifera*

II.1. Introduction

Boron has been known to be an essential micronutrient for all terrestrial plants and many other organisms since at least the 1920s. However, it can also be toxic at higher environmental concentrations (Warington, 1923; Goldbach et al., 2001) suggesting a rather narrow optimal concentration window. A considerable amount of literature has focused on the element from the perspective of its effects on terrestrial agriculture (Tanaka and Fujiwara, 2008) where there are examples of both boron deficiency (Warington, 1923) and toxicity (Yau et al., 1995). As a consequence, both boron-tolerant and boron-efficient cultivars have been developed. The essentiality of boron to higher plants stems from its ability to crosslink cell wall carbohydrates. The first isolated B-cell wall complex was identified as the *bis*-diester of boron with the pectic polysaccharide rhamnogalacturonan II (RG-II) (Kobayashi et al., 1996). Monomeric RG-II has four side chains, two of which contain apiose. The apiosyl residues engage in spirocyclic borate-crosslinking between apiofuranosyl residues of two 2-O-methyl-D-xylose sidechains resulting in a dimeric complex. In general, borate reacts most strongly with sugars that have *cis*-1,2-diols on a furanoid ring as a result of both steric and electronic forces (Acree, 1973; Vandenberg et al., 1994).

In contrast to the generally boron-poor terrestrial environment, the concentration of boron in the marine environment is relatively high (0.4 mM) and while there has been extensive interest in its use as a surrogate of pH in paleoclimate studies in the context of

climate change-related questions (Spivack et al., 1993), the relatively depth independent, and the generally non-nutrient-like concentration profile of this element have led to it being neglected as potentially biologically relevant. This dearth of research persists despite the fact that a number of studies report that boron is essential for the growth and development in many marine plant-like linages and that it is recognized as an important constituent of algal culture media (Spector, 1956). For example, in the marine red algae *Bangia* and *Porphyra*, boron at seawater concentrations is essential for sustained growth (Henkel, 1952), while Lewin demonstrated the requirement of boron for the growth of marine pennate and centric diatoms (Lewin, 1965; Lewin, 1966a; Lewin, 1966b; Lewin and Chen, 1976). An essential role of boron in the development of the brown macroalga *Fucus edentatus* (Phaeophyceae) was also recognized (McLachlan, 1977) whereby omission of boron from the culture medium resulted in moribund embryos with normal development being restored by adding 1 - 4 µM boron. Gametogenesis in brown algal gametophytes (of the kelps *Laminaria japonica* and *L. angustata* and of the sulfuric acid-producing *Desmarestia ligulata*) is also known to be strongly affected by the availability of boron (Motomura & Sakai, 1984). Demonstration of the presence of boroesters in marine plants was initially described for a sulfated polysaccharide of the green seaweed *Ulva lactuca* (Haug, 1976) and later shown by ^{11}B NMR to also be present in red and brown macroalgae (Chuda et al., 1997).

Among the marine plant-like organisms, the brown algae (Phaeophyta) are one of only three lineages of photosynthetic eukaryotes to have evolved complex multicellularity. Many of brown algae's unusual and often unique features are attributable to this singular evolutionary history. These adaptations are a reflection of the marine

coastal environment which brown algae dominate in terms of biomass. For example, extensive kelp forests effectively serve as an interface between the ocean atmosphere and land masses, whereas filamentous seaweed accumulates on man-made surfaces to such extents that it is largely considered a nuisance in marine industries. Consequently, brown algae are of fundamental importance to oceanic ecology, geochemistry, and coastal industry. Just as brown algae morphology differs greatly by order, their ecological roles and industrial applications differ as well.

Herein, I describe boron uptake, speciation, localization and possible biological function in two species of brown algae: *Macrocystis* and *Ectocarpus*. With a length of up to 60 m, *Macrocystis* is by far the largest seaweed in the world and, indeed, one of the largest organisms on Earth. *Macrocystis* is also the single largest source of raw material for the global alginate industry and supports an economic activity of several hundred million dollars annually (McHugh, 1987). *Ectocarpus* is one of the best-studied seaweeds and has many significant advantages as an experimental model. In addition to being easily cultured in the laboratory, it is the first seaweed of which the entire genome has been sequenced and thus offers many opportunities for study.

II.2. Results

II.2.1. Boron Uptake

Boron uptake by *Ectocarpus* and *Macrocystis* was quantified by ICP-MS elemental analysis of algal biomass over a 24 hour period (see section II.4 for methods). *Ectocarpus* exhibits near linear uptake for ~4 h, after which uptake ceased (Fig. II.1). Concentration-dependent boron uptake data during the linear

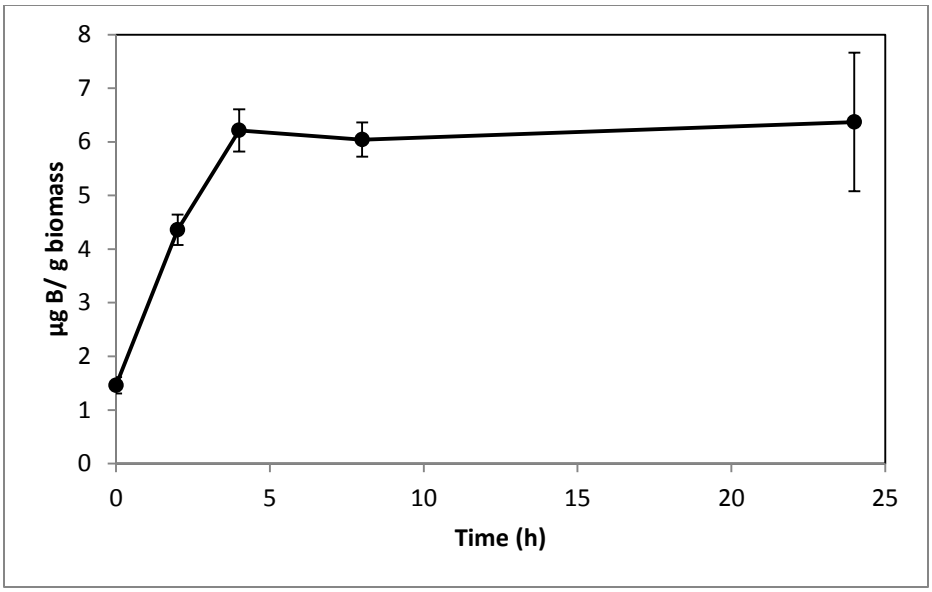

Figure II.1. Boron uptake in *Ectocarpus* from ASW medium enriched with 0.4 mM borate as a function of time. Error bars represent ± 1 S.D. from duplicate experiments with replicate time points for each.

uptake period (Fig. II.2) most accurately fits a biphasic system consisting of both a saturable carrier-assisted transport and a non-saturable diffusion-limited transport as defined by Neame and Richards (Neame and Richards, 1972):

$$\text{Rate} = \frac{V_{max} \bullet [S]}{K_M + [S]} + K_D \bullet [S]$$

where V_{max} is the maximum carrier transport rate, [S] is the substrate concentration, K_M is the Michaelis constant, and K_D is the diffusion constant. Non-linear least squares fits to the data implemented using Sigma Plot 12.5™ (Systat Software Inc., USA) yielded V_{max}= 1.07 ng B•mg biomass^{-1}•hr^{-1}, K_m= 7.8 µM, and K_D= 1.7x10^{-4} ng B•mg biomass^{-1}•hr^{-1}•µM^{-1}.

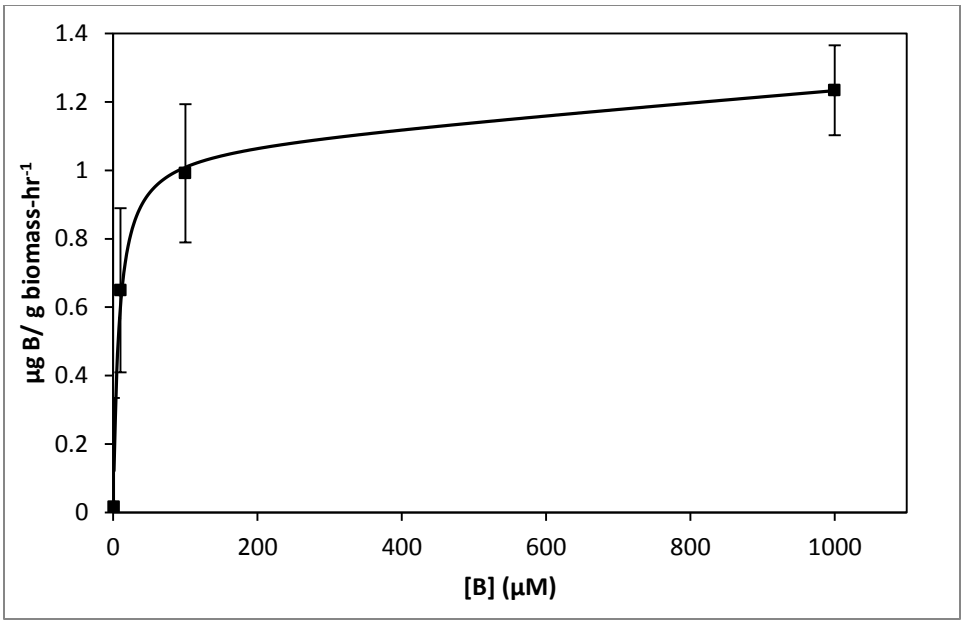

Figure II.2. Uptake of boron by *Ectocarpus* after two hour incubation in ASW medium as a function of boron concentration. Data points are shown as squares while the solid line represents fits to the data as described in the text. Error bars represent ± 1 S.D. from duplicate experiments with replicate concentration points for each.

Macrocystis blade and stipe take up significantly more boron than seen with *Ectocarpus* (Fig. II.3). We examined uptake by both blade and stipe. Blade uptake slows over a 24 hour period while near linear

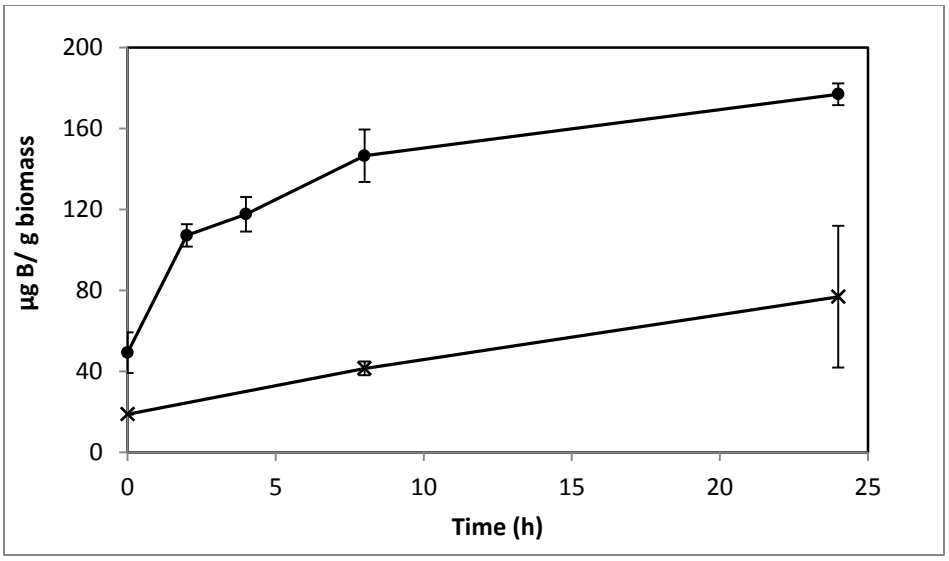

Figure II.3. Boron uptake by *Macrocystis* blade (closed circles) and stipe (X) from ASW medium enriched with 0.4 mM borate as a function of time. Error bars represent ± 1 S.D. from duplicate experiments with replicate time points for each.

boron uptake in the stipe continues over the same period. In contrast to *Ectocarpus*, a diffusion parameter is not necessary to fit concentration dependent boron uptake in *Macrocystis* (Fig. II.4). Blade and stipe both display low affinity saturation kinetics with V_{max}=150 ng B•mg biomass^{-1}•hr^{-1}, K_m= 863 µM and V_{max}= 30 ng B•mg biomass^{-1}•hr^{-1}, K_m= 318 µM, respectively.

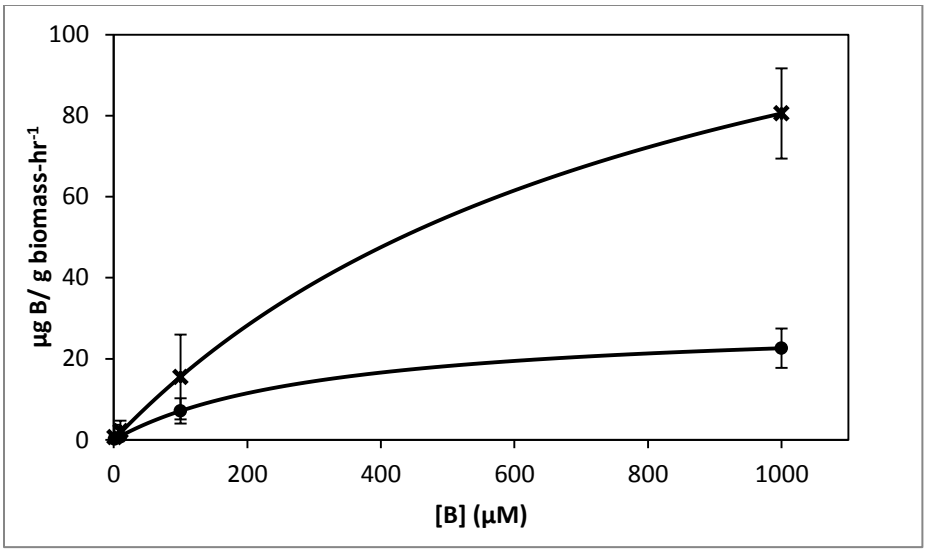

Figure II.4. Uptake of boron by *Macrocystis* blade (X) after two hour incubation and stipe (closed circles) after four hour incubation in ASW medium as a function of boron concentration. Data points are shown as x's (blade) or closed circles (stipe) while the solid line represents fits to the data as described in the text. Error bars represent ± 1 S.D. from duplicate experiments with replicate concentration points for each.

II.2.2. Boron Localization

The localization of boron in brown algal tissue was investigated using two separate means. The first involves determining the location of likely boron binding sites (*cis*-diols), the two most likely of which are the primary carbon storage molecule mannitol, and the primary structural carbohydrate, alginic acid. We used micro Raman spectroscopy to identify high concentrations of these species and compared their localization with that found for the fluorescent dye phenylboronic acid- fluorescein isothiocyanate (B-FITC) which has previously been used as a probe for boron binding sites in terrestrial plants (Glüsenkamp et al., 1997). B-FITC likely forms highly fluorescent monoesters with *cis*-diol species since the stable B-C bond in phenylboronic

acid precludes formation of borodiesters.

Treatment of *Ectocarpus* with B-FITC leads to a fluorescence signal that is diffuse in some areas while discreet in other structured areas such as the plastids visible in the bright-field image of Figures II.5A and II.5B. Although some of the fluorescence appears to be intracellular, a strong signal is seen in the apoplast as well (Figs. II.5C and II.5D).

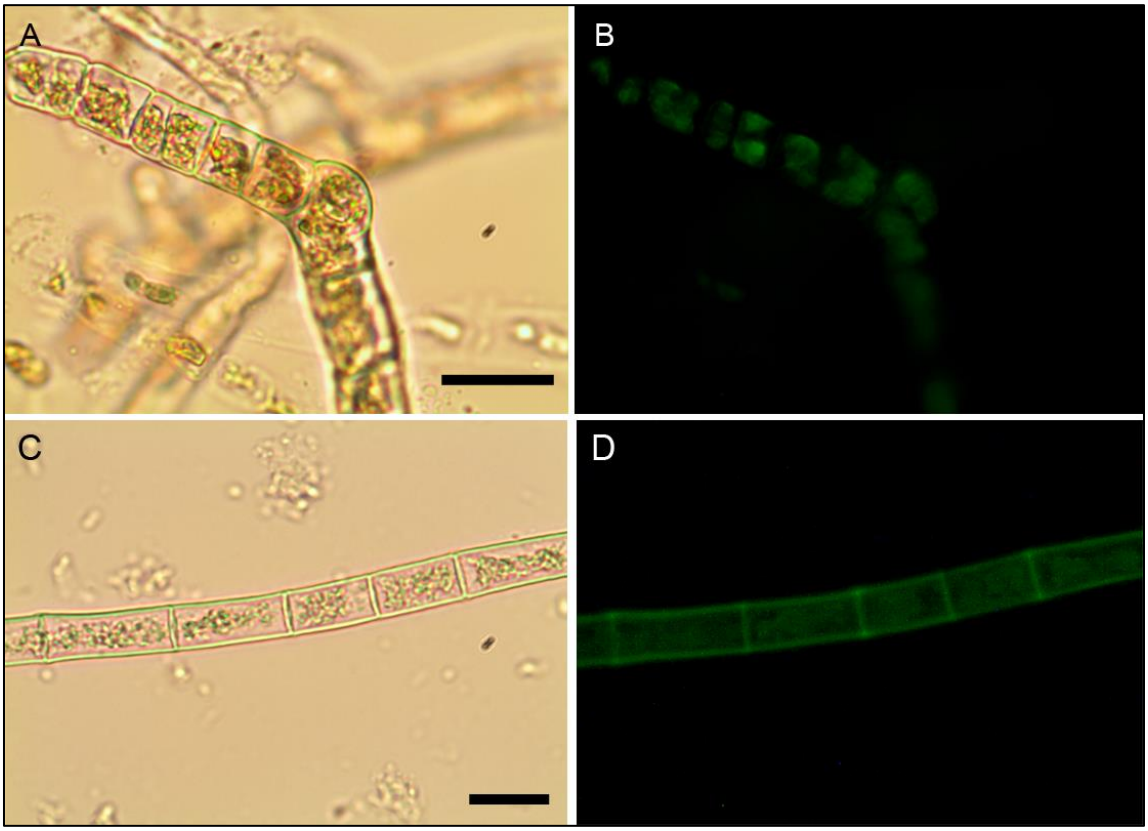

Figure II.5. *Ectocarpus.* (A & C) Brightfield transmission, (B & D) B-FITC fluorescence. Scalebars, 30 µm.

Macrocystis exhibits much more cellular and tissue differentiation with many

different potential ligand environments as compared to *Ectocarpus* and correspondingly leads to a more complex staining pattern. B-FITC signal is localized to the meristoderm, cortical, and medullar apoplasts in the blade and stipe (Figs. II.6 and II.7).

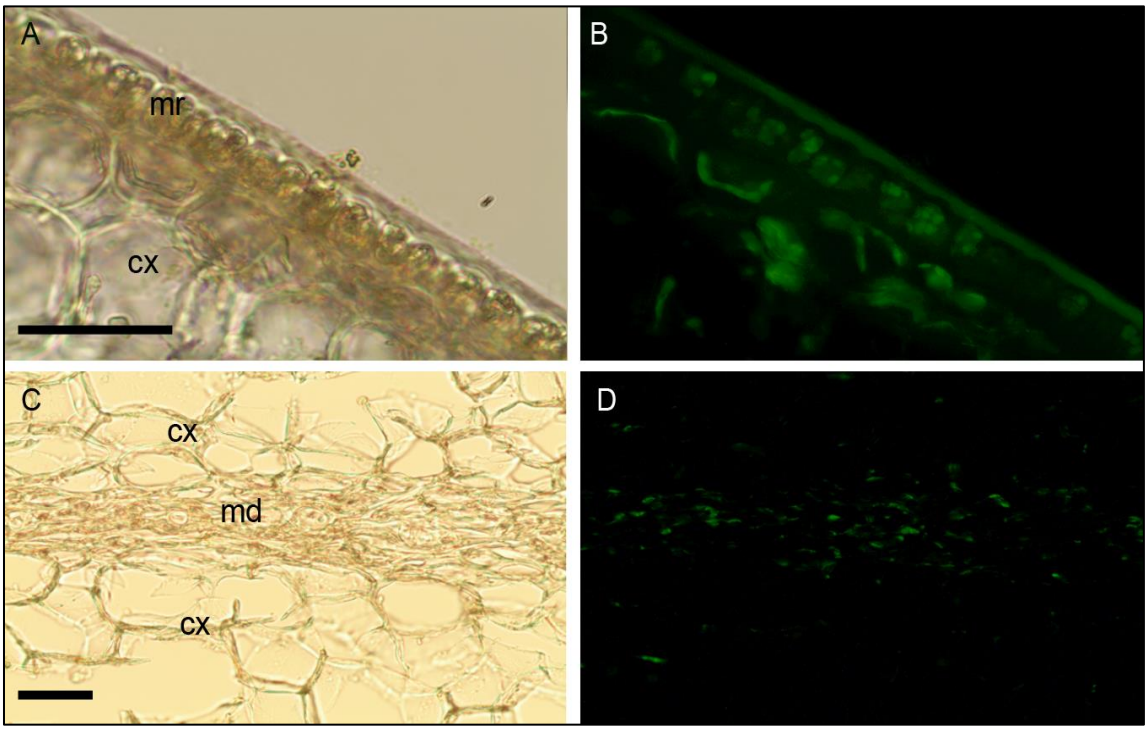

Figure II.6. *Macrocystis* blade. Meristoderm and cortex (A) Brightfield transmission, (B) B-FITC fluorescence. Medulla (C) Brightfield transmission, (D) B-FITC fluorescence. Meristoderm (mr), cortex (cx), medulla (md). Scalebars, 40 µm.

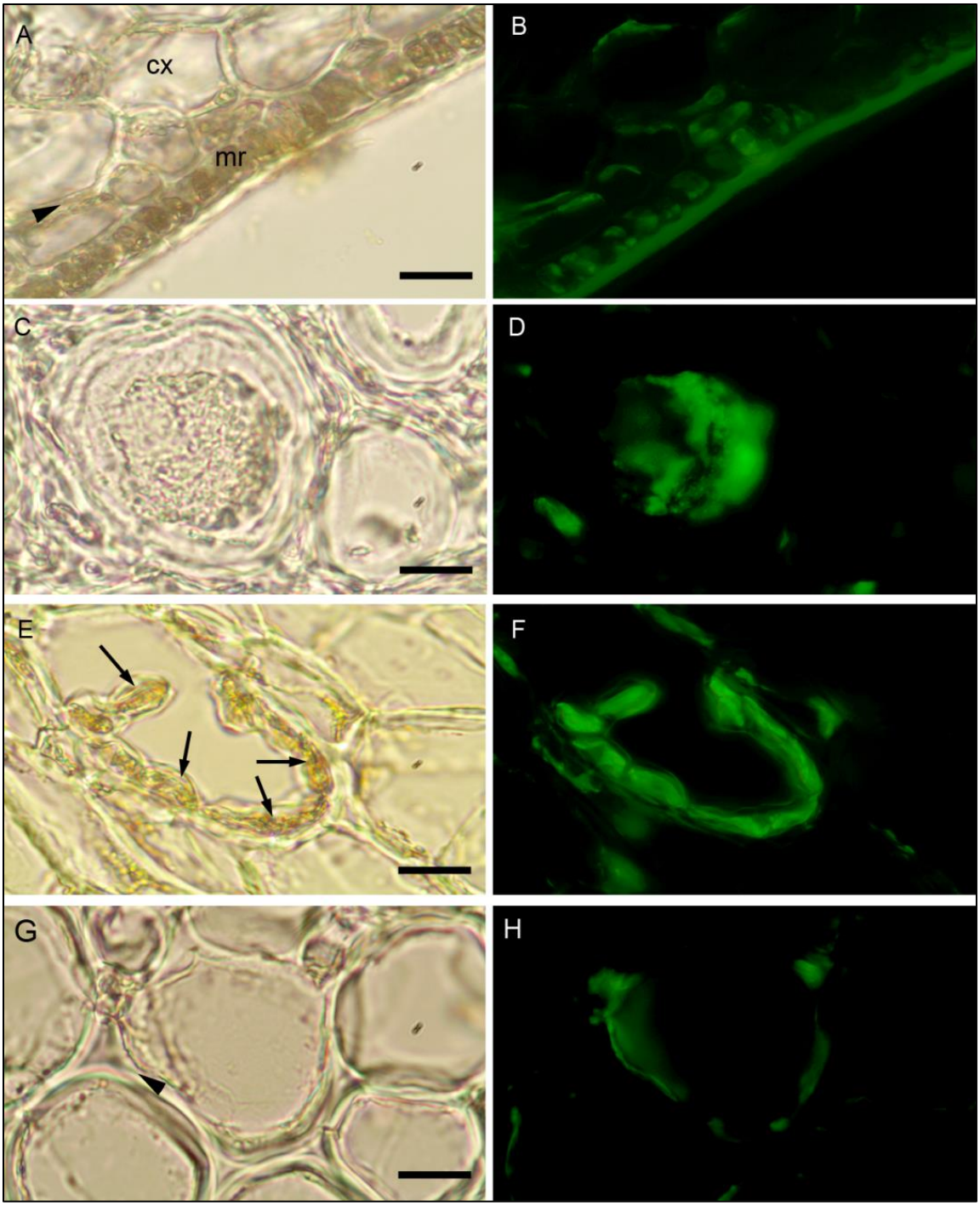

Figure II.7. ***Macrocystis*** **stipe. Meristoderm (A) Brightfield transmission and (B) B-FITC fluorescence. (C & D) Medullar sieve cells. (E & F) Cortex with secretory cells (arrows). (G & H) Cortex cells. Meristoderm (mr), cortex (cx), arrowheads indicate apoplasts. Scalebars, 20 µm.**

In the stipe cortex, fluorescence from secretory cells (black arrows) suggests significant amounts of *cis*-diols (Fig. II.7F). Sieve cells in the stipe medulla also fluoresce, indicating a possible transported metabolite with *cis*-diol groups (Fig. II.7D).

With the apparent strong fluorescent signal of the B-FITC probe in the apoplast and sieve cells of *Macrocystis* suggesting high concentrations of potential boron binding ligands, we used micro-Raman spectroscopy to identify likely candidates. Figure II.8 shows a complete Raman spectrum of the apoplastic region of a *Macrocystis* cortical cell along with a heat map of Raman spectral intensity at 955 cm^{-1}.

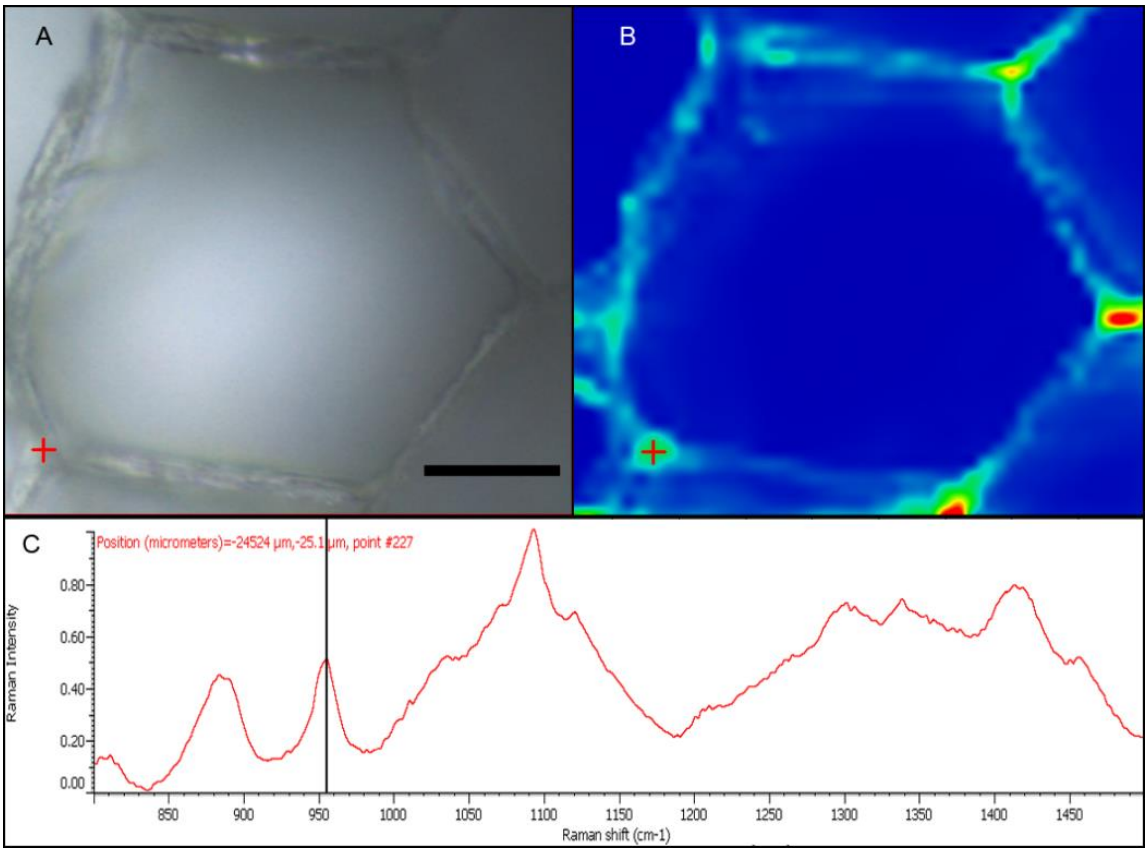

Figure II.8. *Macrocystis* cortex. (A) Brightfield. (B) Heatmap of the 955 cm-1 Raman shift. (C) Raman spectrum of the point indicated by the red crosshairs in (A) and (B). Scalebar, 20 µm.

The Raman spectra displayed has been identified as that of alginate by comparison with the literature (Schmid et al., 2008). As can be seen, the intensity of the 955 cm^{-1} band indicative of the presence of alginate, is concentrated in the apoplastic regions of the cortical cells. This mirrors the staining pattern seen for the same cell type with the B-FITC probe suggesting boron binding to alginate in the apoplast of these cells. In comparison, different results were seen when sieve cells were examined. Here, the Raman spectrum (Figure II.9C) appears to be that of mannitol as determined by comparison with a pure standard (Figure II.9D). A corresponding heat map based on the 875 cm^{-1} Raman shift characteristic of mannitol shows a concentration of this species in the sieve cells. Again this mirrors the staining pattern of B-FITC for these cells.

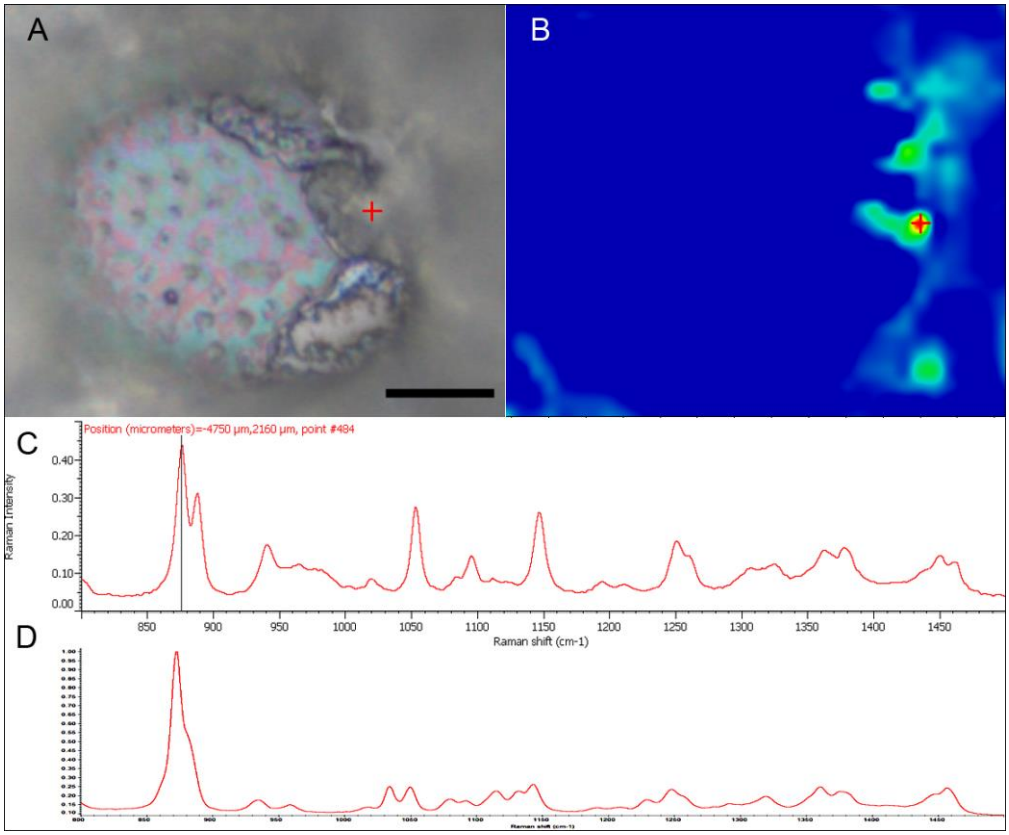

Figure II.9. *Macrocystis* sieve cell. (A) Brightfield micrograph. (B) Heat map of the 875 cm-1 Raman shift. (C) Raman spectrum of the point indicated by the red crosshairs in (A) and (B). (D) Raman spectrum of pure mannitol standard. Scalebar, 15 µm.

While the above methods provide information about the nature and localization of boron binding sites in algal cells they do not actually report localization of boron itself. To accomplish the latter we utilized energy dispersive X-ray spectroscopy (EDS) in scanning transmission electron microscopy (STEM) mode which allowed the mapping of boron in uncoated algal sections. Uncoated thin sections (<60 nm) facilitated transmission of a low energy (<7 keV) electron beam through the section, thus providing an adequate K_α X-ray signal for mapping boron while minimizing self-absorption by the sample. The boron binding sites on or in plastids, as suggested by B-FITC, are confirmed

for *Ectocarpus* (Fig. II.10). Additional boron appears concentrated to the cell wall, a cellular component that did not exhibit B-FITC fluorescence.

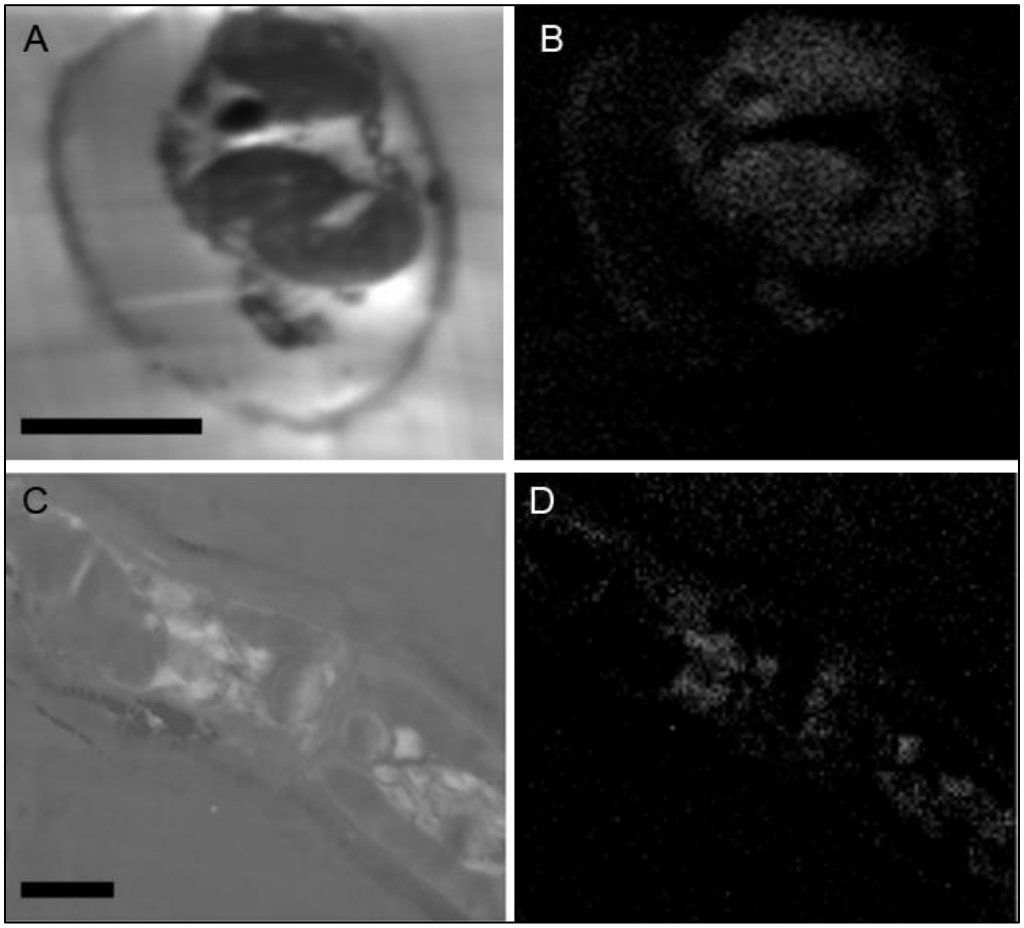

Figure II.10. *Ectocarpus* embedded cross-sections. Longitudinal section (A) STEM, (B) EDS boron K_α signal of the field in (A).. Lateral section (C) STEM. (D) EDS boron K_α signal of the field in (C). Scalebars, 10 µm.

Macrocystis blade meristoderm cells contain significant levels of boron (Fig II.11) while most other cell types in the blade and stipe contain a detectable amount of boron extracellularly

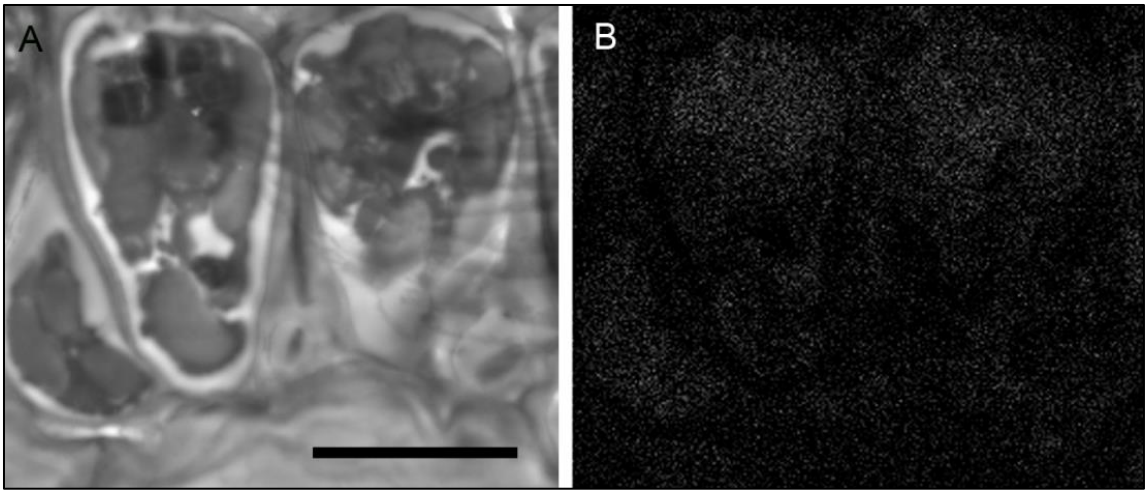

Figure II.11. *Macrocystis* blade meristoderm. (A) STEM, (B) EDS boron K_α signal of the field in (A).. Scalebar, 5 µm.

(apoplastic) but not intracellularly. An exception is the sieve cells located in the medulla (Fig. II.12F) where intracellular boron is evident.

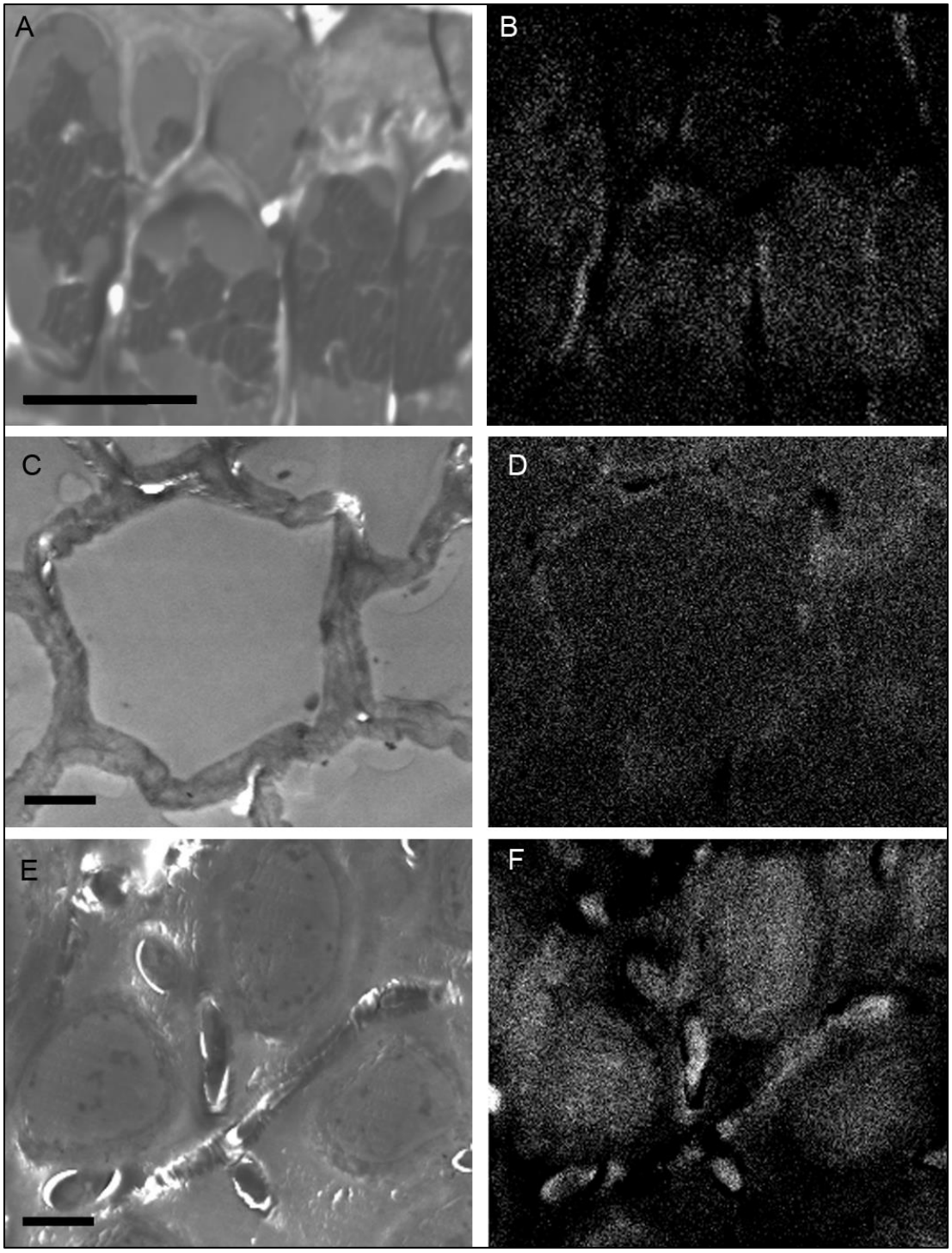

Figure II.12. *Macrocystis* stipe. Meristoderm (A) STEM, (B) EDS boron K_α signal of the field in (A). Cortex (C) STEM, (D) EDS boron K_α signal of the field in (C). Medulla (E) STEM, (F) EDS boron K_α signal of the field in (E). Scalebars, 10 µm.

II.2.3. Boron Speciation

The chemical nature of the bound boron in intact brown algal cells was examined by ^{11}B NMR. Previous studies have established that boron is found in sufficient quantities in brown algal cells to allow determination of some aspects of its chemical nature by this technique (Chuda et al., 1997). The ^{11}B NMR spectrum of *Ectocarpus* is shown in Figure II.13 which shows two resonances, one at 19.2 and a second at 9.5 ppm. While broad band decoupled NMR signals cannot be strictly quantitated by signal integration, it is clear that the 19.2 ppm band is in the majority. Previous work has established that trigonal planar boro-monoesters and boric acid itself appear near 19-20 ppm, tetrahedral monoesters between 6 and 8 ppm, tetrahedral borodiesters in the 9-10 ppm range and borate itself near 0 ppm (Bishop et al., 2004). Based

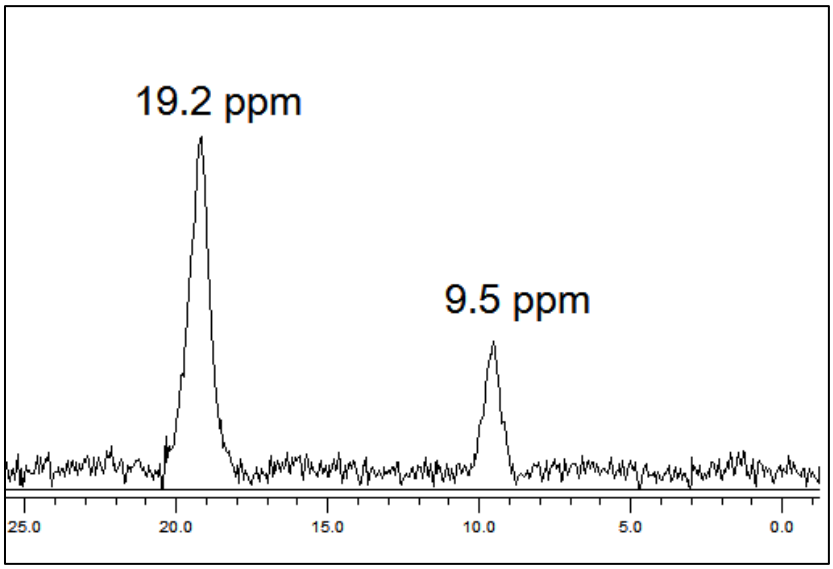

Figure II.13. ^{11}B NMR of *Ectocarpus*. 10000 scans were acquired with standard pulse sequences (50 ms pulse duration, 50 ms relaxation) at 5°C. A broad ^{11}B signal originating from the borosilicate NMR probe was manually background subtracted.

on this we assign the 19.2 ppm band in *Ectocarpus* as due to trigonal planar boromonoester likely from boron bound to polymeric alginate where borodiester formation is sterically restricted. The 9.5 ppm peak is clearly that of a tetrahedral borodiester most probably the *bis*-mannitol complex. The ^{11}B NMR spectra of *Macrocystis* blade and stipe (Figures II.14A and II.14B, respectively) show the same two species but in different ratios. The blade seems to have a relatively small quantity of boron (based on the S/N ratio) and roughly equivalent amount of both species being present while the stipe has both a much stronger boron signal and appears to be almost entirely borodiester. This latter observation is consistent with the high concentration of mannitol found in the stipe (Reed et al., 1985)

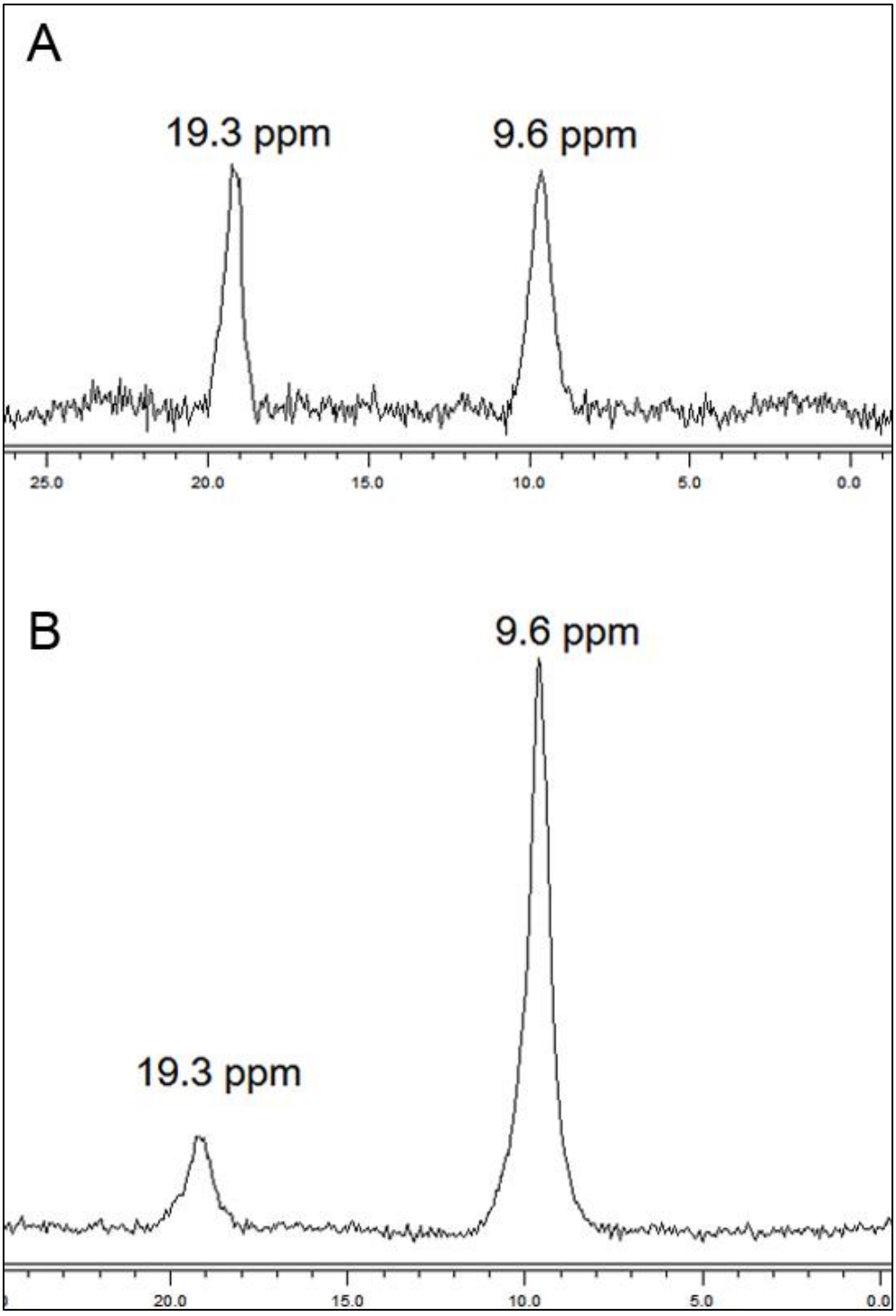

Figure II.14. ^{11}B NMR of *Macrocystis* (A) blade (B) stipe. 10000 scans were acquired with standard pulse sequences (50 ms pulse duration, 50 ms relaxation) at 5°C. A broad ^{11}B signal originating from the borosilicate NMR probe was manually background subtracted.

II.3. Discussion

A broad systematic understanding of boron uptake mechanisms is lacking for animals, though uptake is known to occur across mucous membranes of the gastrointestinal and respiratory systems. In contrast, terrestrial plants are fairly well studied with regards to boron uptake with the molecular aspects of boron transporters having recently been reviewed (Tanaka and Fujiwara, 2008). Boric acid is an uncharged and undissociated molecule over much of the physiological pH range and therefore it is this form that is considered to be the species taken up (Raven, 1980), generally assumed to occur through passive diffusion. However recent studies over the last decade have shown that uptake occurs as an active process mediated by active BOR transporters or facilitated by nodulin-like intrinsic proteins (NIPs). BOR1, a member of the SLC4 anion-exchanger superfamily (Frommer and von Wiren, 2002) which also includes bicarbonate transporters, was identified as the first transport protein involved in active boron-loading of the xylem in the higher plant model *Arabidopsis* (Takano et al., 2002). Shortly afterwards, the same group found several members of the major intrinsic proteins (MIPs), namely NIP5;1, and NIP6;1 to be essential for boron uptake and plant development under boron limitation (Takano et al., 2006; Tanaka et al., 2008). These molecules appear to function as channels or porins for boron (Kato et al., 2009).

In contrast to the terrestrial environment, the marine environment is boron-rich, suggesting perhaps the greater need for a boron efflux system (to prevent toxicity) over one for transport. Recently, using yeast as a eukaryotic model system, several proteins in addition to BOR1 have been implicated in resistance to boron toxicity including DUR3, FPS1 and ATR1 (Kaya et al., 2009). It was subsequently shown that ATR1 was the

primary efflux system responsible for boron tolerance in yeast and that overexpression of this protein allowed growth on media containing as much as 200 mM boron (Kaya et al., 2009). ATR1 homologs were detected in fungi, bacteria and archaea but not in the limited array of animals, vascular plants, or algae examined. Our results along with data from the literature indicate that boron is indeed taken up, likely by a facilitated diffusion mechanism and against a considerable concentration gradient. Manley reports that sieve tube sap from *Macrocystis* has a boron concentration between 24-32 mM- an increase over seawater concentration by a factor of 75-fold (Manley, 1983). To take up boron against such a concentration gradient requires either an energy dependent transport system or an internal sink (*vide infra*) which removes it from equilibrium. Both mechanisms seem possible in the brown algae.

The presence of an active transport system is suggested by our concentration dependent uptake results where *Ectocarpus* appears to take up boron with much higher affinity but lower capacity than the system seen in either *Macrocystis* blade or stipe. Additionally, homologs have been identified in the *Ectocarpus* genome that cluster in the same clade with BOR1 of *Arabidopsis*, the yeast protein YNL275w (BOR1p) and the BTR1 protein of humans (Carrano et al., 2009). Similar homologs are also found in the genome of the diatom *Phaeodactylum tricornutum*. Thus, it appears that boron transporters may be widespread among marine plant-like lineages.

It is widely regarded that the primary role of boron in higher plants is the formation of cell wall carbohydrate crosslinks specifically with the peptic polysaccharide rhamnogalacturonan II (RGII). However, it is by no means clear it has the same role in marine brown algae whose major wall polysaccharides (alginate, fucoidan, and cellulose)

are quite different. Based on our results here (^{11}B NMR, micro-Raman and fluorescence microscopy) and literature precedence, we would propose that in both *Ectocarpus* and *Macrocystis* some boron is indeed bound to cell wall constituents- most likely alginate- but probably does not form crosslinks. This type of interaction appears to occur mainly in the apoplast but its biological function, if any, remains unresolved. The second major sink for boron appears to be mannitol.

While much of the essentiality of boron to higher plants stems from its ability to crosslink cell wall carbohydrates, boron is thought to play a part in a number of other essential functions including transport functions, membrane and membrane-associated interactions, reproduction, and nitrogen fixation among them. Mannitol is a monomeric sugar alcohol and one of the primary photosynthetic products in brown algae. It has multiple functions, including osmoregulation, storage, and scavenging of reactive oxygen species. Having *cis*-1,2-diol groups and forming five membered chelate rings when ligated to boron, it forms very stable complexes with this element. Binding constants for the reactions 1 and 2

(1)

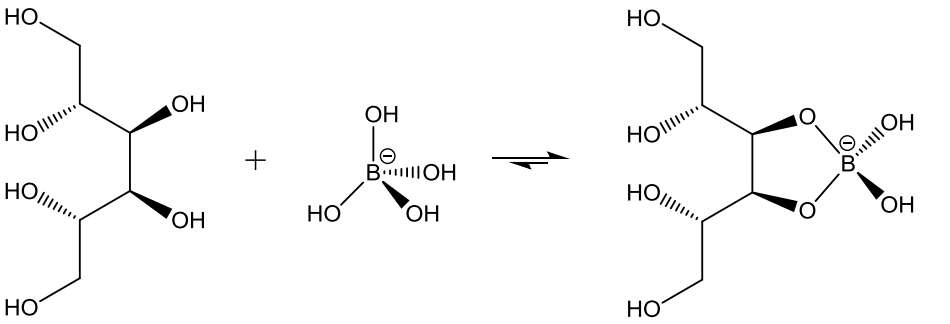

D-mannitol borate B-mannitol monoester

(2)

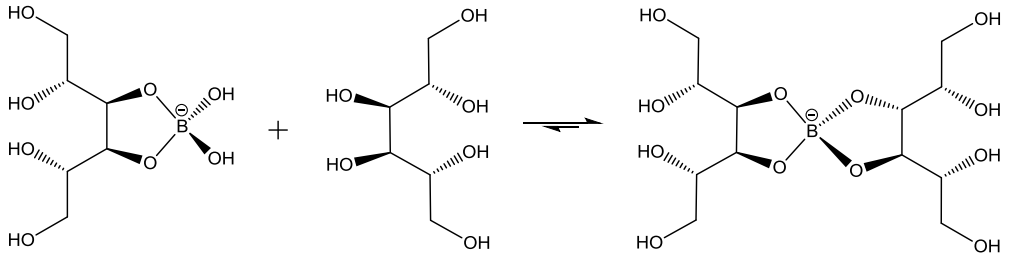

B-mannitol monoester + D-mannitol ⇌ *bis*-mannitol borodiester

have been reported with $\beta_1 = 617$ and $\beta_2 = 155$ (Knoeck and Taylor, 1969).

At the pH and concentrations of boron and mannitol reported by Manley (Manley, 1984) in *Macrocystis* sieve tube sap, it is clear that essentially all the boron would be expected to be complexed as the *bis*-mannitol borodiester. This is consistent with the high level of diester seen in *Macrocystis* stipe as compared to blade, as the former has the higher mannitol content. It is also consistent with the generally higher level of diester in *Macrocystis* versus *Ectocarpus* as again the former has a higher reported mannitol content (ca. 600 mM) compared with that of the latter (ca. 160 mM) (Reed et al., 1985).

As the primary photosynthetic product, mannitol accounts for the bulk of translocated metabolites in brown algae such as *Macrocystis* which, although non-vascular, displays the ability for long distance transport of nutrients. Transport velocities between 35-72 cm/hr have been reported (Parker, 1965; Schmitz and Lobban, 1976). The general picture that has emerged is that transport follows a source-sink model with mature blades being the source and the holdfast and the apical growing tips the sink. Using ^{14}C labeling of blades on intact plants, Schmitz and Srivastava have shown that transport of labeled carbon is toward either the apical growing areas or the holdfast depending on the position of the labeled blades and that the majority of the transported

label is found in mannitol (ca. 60%) or amino acids (ca. 30%) (Schmitz and Srivastava, 1979). This model is consistent with a recent transcriptomic study which indicates that photosynthesis of mannitol occurs primarily in the upper canopy while protein synthesis occurs primarily at depth near the holdfast with long distance transport of nutrients between these two sinks.

With the majority of the data presented here it is clear that in *Macrocystis* that most of the boron is likely to be bound to mannitol as a diester complex. The question then is: what is the biological significance, if any, of this complexation? Is boron modulating transport of mannitol or is mannitol modulating boron transport? Alternatively, is boron modulating the role of mannitol as an osmoprotectant? These and other questions concerning the role of boron in brown algae remain under active investigation.

II.4. Methods

II.4.1. Algal Culture

Ectocarpus CCAP 1310/56 was obtained from the Culture Collection of Algae and Protozoa (CCAP) at the Scottish Association for Marine Science and grown axenically in modified Provasoli-enriched (Andersen) Scripps Pier seawater (SPSW) at 15 °C under a 12/12 light/dark photocycle. *Macrocystis* was harvested from the Point Loma kelp forest (32.7 N, 117.3 W) and either used immediately after collection or maintained in modified Provasoli-enriched Scripps Pier seawater (SPSW) at 12 °C under a 14/10 light/dark photocycle.

II.4.2. Time-dependent boron uptake

Ectocarpus filaments and *Macrocystis* fronds were grown under boron-limited conditions for 48 hours followed by incubation with 0.4 mM borate enriched artificial seawater. Fresh algal tissue samples were washed with borate-free artificial seawater and weighed. Samples were placed in a digestion solution containing 3.5% tetramethylammonium hydroxide (Sigma-Aldrich, USA)) and heated to 90 ℃ for 3 hours. Remaining contents were then brought to 7 mL with nanopure water and filtered through 0.2 µm Isopore™ membrane filters (Millipore, USA). The analysis for heavy metals was performed by inductively coupled plasma mass spectroscopy (ICP-MS, Agilent 7500cx, Agilent Technologies, Inc., USA). The instrument was operated using Spectrum Multi Tune under the following operational conditions: Plasma forward power: 1.55 kW, RF matching 1.78 V, carrier gas (Ar) 0.86 L/min and makeup gas (Ar) 0.20 L/min. MicroMist nebulizer was used and the nebulizer pump rate was at 0.1 rps. Agilent ICP-MS ChemStation was used to control operation and record data. All the determinations were performed in triplicate using the external standard calibration method and with ^{9}Be as the internal standard for ^{10}B. All calibration standards were prepared in 0.5% TMAH. Quality assurance/quality control procedures included blanks, spikes, and standard reference materials, and all results were within acceptable limits. To obtain analyte concentration in the solution, calibration with standard solution concentrations of 1, 2, 10, 25, 50, 100, 200, 500, 1000 and 5000 µg/L were prepared from certified reference material (High-Purity Standards, USA). The standard calibration was carried out every single analysis. The ICP-MS method and smart sequences of sample analysis were optimized to eliminate boron memory effects.

II.4.3. Concentration-dependent boron uptake

Ectocarpus filaments and *Macrocystis* fronds were grown under boron-limited conditions for 48 hours followed by incubation with 1, 10, 100, and 1000 μM borate enriched artificial seawater. Fresh algal tissue samples were washed with borate-free artificial seawater and weighed. Samples were placed in a digestion solution containing 3.5% tetramethylammonium hydroxide (Sigma-Aldrich, USA) and heated to 90 ℃ for 3 hours. Remaining contents were then brought to 7 mL with nanopure water and filtered through 0.2 μm Isopore™ membrane filters (Millipore, USA). The analysis for heavy metals was performed by inductively coupled plasma mass spectroscopy (ICP-MS, Agilent 7500cx, Agilent Technologies, Inc., USA). The instrument was operated using Spectrum Multi Tune under the following operational conditions: Plasma forward power: 1.55 kW, RF matching 1.78 V, carrier gas (Ar) 0.86 L/min and makeup gas (Ar) 0.20 L/min. MicroMist nebulizer was used and the nebulizer pump rate was at 0.1 rps. Agilent ICP-MS ChemStation was used to control operation and record data. All the determinations were performed in triplicate using the external standard calibration method and with ^{9}Be as the internal standard for ^{10}B. All calibration standards were prepared in 0.5% TMAH. Quality assurance/quality control procedures included blanks, spikes, and standard reference materials, and all results were within acceptable limits. To obtain analyte concentration in the solution, calibration with standard solution concentrations of 1, 2, 10, 25, 50, 100, 200, 500, 1000 and 5000 μg/L were prepared from certified reference material (High-Purity Standards, USA). The standard calibration was carried out every single analysis. The ICP-MS method and smart sequences of sample

analysis were optimized to eliminate boron memory effects.

II.4.4. B-FITC histochemistry

Algal tissue was cryo-fixed in liquid nitrogen and sectioned with a Leica CM1950 cryostat (Leica Microsystems, Inc., USA). Sections (50 µm thickness) were placed on glass well slides and allowed to thaw. Once thawed, sections were incubated for 2 min with 3-(3-(3',6'-Dihydroxy-3-oxo-3H-spiro[isobenzofuran-1,9'-xanthene]-5-yl)thioureido)phenylboronic acid (B-FITC) prepared as described by (Glüsenkamp et al., 1997). Sections were washed thoroughly with 0.1 M phosphate (pH 8.1) buffer before fluorescence imaging with a Nikon Eclipse TE2000-U inverted microscope (Nikon Imaging, Inc., Japan).

II.4.5. Energy-dispersive X-ray spectroscopy (EDS)

Cells were fixed in a 0.1 M phosphate buffer solution containing 2% (w/v) paraformaldehyde and 1% (w/v) glutaraldehyde for 2 h. Fixed cells were then washed with 0.1 M phosphate buffer and dehydrated in successive ethanol baths of 30, 50, 75, 85, 95, and 100% (x3). The cells were then infiltrated with 1:1 (v/v) ethanol/LR White embedding medium (Electron Microscopy Sciences, USA) for 3 h followed by 100% LR White overnight. Cells were embedded in 100% LR White at 60℃ under vacuum for 6 h. Sections (60 nm thickness) were cut on a Reichert-Jung Ultracut E microtome (Reichert, Austria) and floated onto formvar-coated 100-mesh copper grids (Ted Pella, USA). Grids were placed in a sample holder on a stage which facilitates deployment of a transmitted electron detector in the scanning electron microscope (SEM) chamber. Samples were

analyzed under high vacuum in a Quanta 450 FEG SEM equipped with an INCA (Oxford Instruments, USA) energy-dispersive X-ray microanalysis system. Uncoated samples allowed simultaneous transmitted electron imaging and X-ray analysis with low accelerating voltage (5 – 7 keV).

II.4.5. Raman microspectroscopy

Cryosections of 50 μm thickness were placed on crystalline silicon wafers and lyophilized. Dry sections were imaged with a Thermo Scientific DXR Raman microscope (Thermo Fisher Scientific, USA) and then scanned at 2 μm resolution with a 532 nm laser at 10 mW power. Each spectrum was background-subtracted and relevant peaks were selected for creating maps of a specific Raman shift.

II.4.6. ^{11}B Nuclear magnetic resonance (NMR)

All NMR experiments were carried out on a Varian 500 MHz NMR spectrometer (Varian Inc., USA) using fresh algal material cored with a 3 mm diameter tool and immediately inserted into NMR tubes and placed in the spectrometer maintained at 5 °C. 10000 scans were acquired with standard pulse sequences (50 ms pulse duration, 50 ms relaxation) for the ^{11}B experiments. To eliminate the broad borosilicate background of glass NMR tubes, quartz NMR tubes (Wilmad-Labglass, USA) were used throughout. The remaining borosilicate background from the instrument probe was manually subtracted using the NMR data processing software MestRe-C (MestreLab Research, Spain). Samples were referenced relative to an external standard of BF_3-etherate.

II.4. Acknowledgements

This research was supported by a California State University Council on Ocean Affairs, Science and Technology (COAST) Grant Development Award #GDP-2013-002. The authors are grateful to Dr. Steve Barlow and the SDSU Electron Microscope Facility for expert technical assistance and instrument time. EM has been supported by a California State University Council on Ocean Affairs, Science and Technology (COAST) graduate scholarship.

Chapter II, in full, has been submitted for publication of the material as it may appear in New Phytologist, 2015, Miller, Eric P.; Wu, Youxian; Carrano, Carl J. The dissertation author was the primary investigator and author of this paper.

III. References

Acree T (1973) Chemistry of Sugars in Boric-Acid Solutions. Adv Chem Ser 208–219

Andersen RA (Robert A Algal culturing techniques / edited by Robert A. Andersen. SERBIULA Sist. Libr. 20

Baldauf SL (2003) The deep roots of eukaryotes. Science **300**: 1703–1706

Bauminger ER, Cohen SG, Dickson DP, Levy A, Ofer S, Yariv J (1980a) Mössbauer spectroscopy of Escherichia coli and its iron-storage protein. Biochim Biophys Acta **623**: 237–242

Bauminger ER, Cohen SG, Labenski de Kanter F, Levy A, Ofer S, Kessel M, Rottem S (1980b) Iron storage in Mycoplasma capricolum. J Bacteriol **141**: 378–381

Bishop M, Shahid N, Yang JZ, Barron AR (2004) Determination of the mode and efficacy of the cross-linking of guar by borate using MAS B-11 NMR of borate cross-linked guar in combination with solution B-11 NMR of model systems. Dalton Trans 2621–2634

Böhnke R, Matzanke BF (1995) The mobile ferrous iron pool in Escherichia coli is bound to a phosphorylated sugar derivative. Biometals **8**: 223–230

Böttger LH, Miller EP, Andresen C, Matzanke BF, Küpper FC, Carrano CJ (2012) Atypical iron storage in marine brown algae: a multidisciplinary study of iron transport and storage in Ectocarpus siliculosus. J Exp Bot **63**: 5763–5772

Boughammoura A, Matzanke BF, Böttger L, Reverchon S, Lesuisse E, Expert D, Franza T (2008) Differential Role of Ferritins in Iron Metabolism and Virulence of the Plant-Pathogenic Bacterium Erwinia chrysanthemi 3937. J Bacteriol **190**: 1518–1530

Bruland KW, Donat JR, Hutchins DA (1991) Interactive influences of bioactive trace-metals on biological production in oceanic waters. Limnol Ocean **36**: 1555–1577

Carrano CJ, Schellenberg S, Amin SA, Green DH, Küpper FC (2009) Boron and Marine Life: A New Look at an Enigmatic Bioelement. Mar Biotechnol **11**: 431–440

Charrier B, Coelho SM, Le Bail A, Tonon T, Michel G, Potin P, Kloareg B, Boyen C, Peters AF, Cock JM (2008) Development and physiology of the brown alga Ectocarpus siliculosus: two centuries of research. New Phytol **177**: 319–332

Chase Z, van Geen A, Kosro PM, Marra J, Wheeler PA (2002) Iron, nutrient, and phytoplankton distributions in Oregon coastal waters. J Geophys Res-Oceans. doi: 10.1029/2001JC000987

Chuda Y, Ohnishi-Kameyama M, Nagata T (1997) Identification of the forms of boron in seaweed by 11B NMR. Phytochemistry **46**: 209–213

Cock JM, Sterck L, Rouzé P, Scornet D, Allen AE, Amoutzias G, Anthouard V, Artiguenave F, Aury J-M, Badger JH, et al (2010) The Ectocarpus genome and the independent evolution of multicellularity in the brown algae. Nature **465**: 617–621

Curie C, Briat J-F (2003) Iron transport and signaling in plants. Annu Rev Plant Biol **54**: 183–206

Dassa E, Bouige P (2001) The ABC of ABCs: a phylogenetic and functional classification of ABC systems in living organisms. Res Microbiol **152**: 211–229

Davis TA, Volesky B, Mucci A (2003) A review of the biochemistry of heavy metal biosorption by brown algae. Water Res **37**: 4311–4330

Dziobkowski C, Wrobleski J, Brown D (1981) Magnetic-Properties and Mossbauer-Spectra of Several Iron(iii)-Dicarboxylic Acid Complexes. Inorg Chem **20**: 671–678

La Fontaine S, Quinn JM, Nakamoto SS, Page MD, Göhre V, Moseley JL, Kropat J, Merchant S (2002) Copper-dependent iron assimilation pathway in the model photosynthetic eukaryote Chlamydomonas reinhardtii. Eukaryot Cell **1**: 736–757

Ford GC, Harrison PM, Rice JMA, Smith A, Treffry JL, White JL, Yariv J (1984) Ferritin: design and formation of an iron-storage molecule. Philos Trans R Soc Lond B - Biol Sci **304**: 551–565

Frolow F, Kalb AJ, Yariv J (1994) Structure of a unique twofold symmetrical heme-binding site. Nat Struct Biol **1**: 453–460

Frommer WB, von Wiren N (2002) Plant biology - Ping-pong with boron. Nature **420**: 282–283

Glüsenkamp K-H, Kosegarten H, Mengel K, Grolig F, Esch A, Goldbach HE (1997) A fluorescein boronic acid conjugate as a marker for borate binding sites in the apoplast of growing roots of Zea mays L. and Helianthus annuus L. *In* RW Bell, B Rerkasem, eds, Boron Soils Plants. Springer Netherlands, pp 229–235

Goldbach HE, Rerkasem B, Wimmer MA, Brown PH, Thellier M, Bell RW (2001) Boron in Plant and Animal Nutrition. Kluwer Academic/Plenum Publishers, New York

Halliwell B, Gutteridge JMC (2007) Free Radicals in Biology and Medicine. Oxford University Press, Oxford

Harold G. Weger JL (2009) High stability ferric chelates result in decreased iron uptake by the green alga Chlorella kessleri owing to decreased ferric reductase activity and chelation of ferrous iron. Botany **87**: 922–931

Harrison PM, Lilley TH (1989) Ferritin. *In* TM Loehr, ed, Iron Carriers Iron Proteins. VCH Publishers, New York, pp 123–238

Haug A (1976) The influence of borate and calcium on the gel formation of a sulfated polysaccharide from Ulva lactuca. Acta Chem Scand B **30**: 562–566

Henkel R (1952) Ernährungsphysiologische Untersuchungen an Meeresalgen, insbesondere an Bangia pumila. Kiel Meeresforsch **8**: 192–211

Hudson RJM, Morel FMM (1989) Distinguishing between extracellular and intracellular iron in marine phytoplankton. Limnol Ocean **34**: 1113–1120

Hutchins DA, Wang WX, Schmidt MA, Fisher NS (1999) Dual-labeling techniques for trace metal biogeochemical investigations in aquatic plankton communities. Aquat Microb Ecol **19**: 129–138

Johnson KS, Gordon RM, Coale KH (1997) What controls dissolved iron concentrations in the world ocean? Mar Chem **57**: 137–161

Kato Y, Miwa K, Takano J, Wada M, Fujiwara T (2009) Highly Boron Deficiency-Tolerant Plants Generated by Enhanced Expression of NIP5;1, a Boric Acid Channel. Plant Cell Physiol **50**: 58–66

Kaya A, Karakaya HC, Fomenko DE, Gladyshev VN, Koc A (2009) Identification of a Novel System for Boron Transport: Atr1 Is a Main Boron Exporter in Yeast. Mol Cell Biol **29**: 3665–3674

Kelly LW, Barott KL, Dinsdale E, Friedlander AM, Nosrat B, Obura D, Sala E, Sandin SA, Smith JE, Vermeij MJA, et al (2012) Black reefs: iron-induced phase shifts on coral reefs. Isme J **6**: 638–649

Knoeck J, Taylor J (1969) Aqueous Boric Acid-Borate-Mannitol Equilibria. Anal Chem **41**: 1730–&

Kobayashi M, Matoh T, Azuma J (1996) Two chains of rhamnogalacturonan II are cross-linked by borate-diol ester bonds in higher plant cell walls. Plant Physiol **110**: 1017–1020

Köster W (2001) ABC transporter-mediated uptake of iron, siderophores, heme and vitamin B12. Res Microbiol **152**: 291–301

Kovács K, Kuzmann E, Fodor F, Vértes A, Kamnev AA (2006) Mössbauer study of iron uptake in cucumber root. *In* P-E Lippens, J-C Jumas, J-MR Génin, eds, ICAME 2005. Springer Berlin Heidelberg, pp 289–294

Kovács K, Kuzmann E, Tatár E, Vértes A, Fodor F (2009) Investigation of iron pools in cucumber roots by Mössbauer spectroscopy: direct evidence for the Strategy I iron uptake mechanism. Planta **229**: 271–278

Kranzler C, Lis H, Shaked Y, Keren N (2011) The role of reduction in iron uptake processes in a unicellular, planktonic cyanobacterium. Environ Microbiol **13**: 2990–2999

Kustka AB, Allen AE, Morel FMM (2007) Sequence analysis and transcriptional regulation of iron acquisition genes in two marine diatoms. J Phycol **43**: 715–729

Lanquar V, Lelievre F, Bolte S, Hames C, Alcon C, Neumann D, Vansuyt G, Curie C, Schroder A, Kramer U, et al (2005) Mobilization of vacuolar iron by AtNRAMP3 and AtNRAMP4 is essential for seed germination on low iron. Embo J **24**: 4041–4051

Lawson DM, Artymiuk PJ, Yewdall SJ, Smith JMA, Livingstone JC, Treffry A, Luzzago A, Levi S, Arosio P, Cesareni G, et al (1991) Solving the structure of human H-ferritin by genetically engineering intermolecular crystal contacts. Nature **349**: 541–544

Lewin J (1966a) Boron as a growth requirement for diatoms. J Phycol **2**: 160–163

Lewin J, Chen C (1976) Effects of boron deficiency on the chemical composition of a marie diatom. J Exp Bot **27**: 916–921

Lewin JC (1965) The boron requirement of a marine diatom. Naturwissenschaften **52**: 70

Lewin JC (1966b) Physiological studies of the boron requirement of the diatom, Cylindrotheca fusiformis Reimann and Lewin. J Exp Bot **17**: 473–479

Liu JW, Dong SL, Liu XY, Ma S (2000) Responses of the macroalga Gracilaria tenuistipitata var. liui (Rhodophyta) to iron stress. J Appl Phycol **12**: 605–612

Mabeau S (1987) Isolation and analysis of the cell walls of brown algae: Fucus spiralis, F. ceranoides, F. vesiculosus, F. serratus, Bifurcaria bifurcata and Laminaria digitata. J Exp Bot **38**: 1573–1580

Manley SL (1981) Iron uptake and translocation by Macrocystis pyrifera. Plant Physiol **68**: 914–918

Manley SL (1984) Micronutrient uptake and translocation by Macrocystis pyrifera (Phaeophyta). J Phycol **20**: 192–201

Manley SL (1983) Composition of Sieve Tube Sap from Macrocystis Pyrifera (phaeophyta) with Emphasis on the Inorganic Constituents1. J Phycol **19**: 118–121

Mann S, Williams JM, Treffry A, Harrison PM (1987) Reconstituted and native iron-cores of bacterioferritin and ferritin. J Mol Biol **198**: 405–416

Marchetti A, Parker MS, Moccia LP, Lin EO, Arrieta AL, Ribalet F, Murphy MEP, Maldonado MT, Armbrust EV (2009) Ferritin is used for iron storage in bloom-forming marine pennate diatoms. Nature **457**: 467–470

Martin JH, Fitzwater SE (1988) Iron-deficiency limits phytoplankton growth in the Northeast Subarctic Pacific. Nature **331**: 341–343

Martinoia E, Maeshima M, Neuhaus HE (2007) Vacuolar transporters and their essential role in plant metabolism. J Exp Bot **58**: 83–102

Matsunaga K, Suzuki Y, Kuma K, Kudo I, Nakabayashi S (1991) Uptake rate of iron by macroalgae from the Sea of Japan, Laminaria religiosa and Undaria pinnatifida. Bull Jpn Soc Fish Ocean **55**: 349–353

Matzanke BF, Anemüller S, Schünemann V, Trautwein AX, Hantke K (2004) FhuF, part of a siderophore-reductase system. Biochemistry (Mosc) **43**: 1386–1392

Matzanke BF, Bill E, Trautwein AX, Winkelmann G (1987) Role of siderophores in iron storage in spores of Neurospora crassa and Aspergillus ochraceus. J Bacteriol **169**: 5873–5876

Matzanke BF, Bill E, Trautwein AX, Winkelmann G (1988) Ferricrocin functions as the main intracellular iron-storage compound in mycelia of Neurospora crassa. BioMetals **1**: 18–25

McHugh DJ (1987) Production, properties and uses of alginates. *In* DJ McHugh, ed, Prod. Util. Prod. Commer. Seaweeds. FAO, pp 58–115

McLachlan J (1977) Effects of Nutrients on Growth and Development of Embryos of Fucus-Edentatus-Pyl (Phaeophyceae, Fucales). Phycologia **16**: 329–338

Meguro R, Asano Y, Odagiri S, Li C, Iwatsuki H, Shoumura K (2007) Nonheme-iron histochemistry for fight and electron microscopy: a historical, theoretical and technical review. Arch Histol Cytol **70**: 1–19

Milligan AJ, Mioni CE, Morel FMM (2009) Response of cell surface pH to pCO2 and iron limitation in the marine diatom Thalassiosira weissflogii. Mar Chem **114**: 31–36

Moog PR, Bruggemann W (1994) Iron reductase systems on the plant plasma-membrane - a review. Plant Soil **165**: 241–260

Morrissey J, Guerinot ML (2009) Iron uptake and transport in plants: the good, the bad, and the ionome. Chem Rev **109**: 4553–4567

Mørup S (2011) Magnetic Relaxation Phenomena. Mössbauer Spectrosc. Transit. Met. Chem. Springer Berlin Heidelberg, pp 201–234

Müller DG, Gachon CMM, Küpper FC (2008) Axenic clonal cultures of filamentous brown algae: initiation and maintenance. Cah Biol Mar **49**: 59–65

Naito K, Suzuki M, Mito S, Hasegawa H, Imai I, Sohrin Y, Matsuin M (2001) The pursuit of siderophore secreted by marine phytoplankton R. ovalis. Anal Sci **17**: 817–819

Neame D, Richards G (1972) Elementary Kinetics of Membrane Carrier Transport.

Nölling J, Ishii M, Koch J, Pihl TD, Reeve JN, Thauer RK, Hedderich R (1995) Characterization of a 45-kDa flavoprotein and evidence for a rubredoxin, two proteins that could participate in electron transport from H2 to CO2 in methanogenesis in Methanobacterium thermoautotrophicum. Eur J Biochem FEBS **231**: 628–638

Park M-J, Jung H-S, Kim Y-J, Kwon Y-J, Lee J-K, Park C-M (2014) High-sensitivity fluorescence imaging of iron in plant tissues. Chem Commun **50**: 8547–8549

Parker B (1965) Translocation in Giant Kelp Macrocystis .i. Rates Direction Quantity of C14-Labeled Products and Fluorescein. J Phycol **1**: 41–&

Paz Y, Shimoni E, Weiss M, Pick U (2007) Effects of iron deficiency on iron binding and internalization into acidic vacuoles in Dunaliella salina. Plant Physiol **144**: 1407–1415

Peters AF, Marie D, Scornet D, Kloareg B, Cock JM (2004) Proposal of Ectocarpus siliculosus (Ectocarpales, Phaeophyceae) as a model organism for brown algal genetics and genomics. J Phycol **40**: 1079–1088

Petra Bauer ZB (2003) Gene networks involved in iron acquisition strategies in plants. Agronomie. http://dx.doi.org/101051/agro:2003012. doi: 10.1051/agro:2003012

Ravel B, Newville M (2005) ATHENA, ARTEMIS, HEPHAESTUS: data analysis for X-ray absorption spectroscopy using IFEFFIT. J Synchrotron Radiat **12**: 537–541

Raven JA (1980) Short- and long-distance transport of boric acid in plants. New Phytol **84**: 231–249

Ravet K, Touraine B, Boucherez J, Briat J-F, Gaymard F, Cellier F (2009) Ferritins control interaction between iron homeostasis and oxidative stress in Arabidopsis. Plant J Cell Mol Biol **57**: 400–412

Reed RH, Davison IR, Chudek JA, Foster R (1985) The osmotic role of mannitol in the Phaeophyta: an appraisal. Phycologia **24**: 35–47

Reindel S, Anemüller S, Sawaryn A, Matzanke BF (2002) The DpsA-homologue of the archaeon Halobacterium salinarum is a ferritin. Biochim Biophys Acta **1598**: 140–146

Robinson NJ, Procter CM, Connolly EL, Guerinot ML (1999) A ferric-chelate reductase for iron uptake from soils. Nature **397**: 694–697

Romheld V, Marschner H (1986) Evidence for a specific uptake system for iron phytosiderophores in roots of grasses. Plant Physiol **80**: 175–180

Roschzttardtz H, Conéjéro G, Curie C, Mari S (2009) Identification of the Endodermal Vacuole as the Iron Storage Compartment in the Arabidopsis Embryo. Plant Physiol **151**: 1329–1338

Rubin M, Berman-Frank I, Shaked Y (2011) Dust- and mineral-iron utilization by the marine dinitrogen-fixer Trichodesmium. Nat Geosci **4**: 529–534

Sch?nemann V, Winkler H (2000) Structure and dynamics of biomolecules studied by M?ssbauer spectroscopy. Reports Prog Phys **63**: 263

Schmid T, Messmer A, Yeo B-S, Zhang W, Zenobi R (2008) Towards chemical analysis of nanostructures in biofilms II: tip-enhanced Raman spectroscopy of alginates. Anal Bioanal Chem **391**: 1907–1916

Schmitz K, Lobban C (1976) Survey of Translocation in Laminariales (phaeophyceae). Mar Biol **36**: 207–216

Schmitz K, Srivastava L (1979) Long-Distance Transport in Macrocystis-Integrifolia .1. Translocation of C-14-Labeled Assimilates. Plant Physiol **63**: 995–1002

Semin BK, Davletshina LN, Novakova AA, Kiseleva TY, Lanchinskaya VY, Aleksandrov AY, Seifulina N, Ivanov II, Seibert M, Rubin AB (2003) Accumulation of ferrous iron in Chlamydomonas reinhardtii. Influence of CO2 and anaerobic induction of the reversible hydrogenase. Plant Physiol **131**: 1756–1764

Shaked Y, Kustka AB, Morel FMM (2005) M.: A general kinetic model for iron acquisition by eukaryotic phytoplankton, Limnol. Oceanogr

Sonier MB, Weger HG (2010) Plasma membrane ferric reductase activity of iron-limited algal cells is inhibited by ferric chelators. Biometals Int J Role Met Ions Biol Biochem Med **23**: 1029–1042

Spector WS (ed. . (1956) Handbook of Biological Data. W.B. Saunders Co., Philadelphia, PA

Spivack AJ, You C-F, Smith HJ (1993) Foraminiferal boron isotope ratios as a proxy for surface ocean pH over the past 21 Myr. 363 149-151:

Sutak R, Botebol H, Blaiseau P-L, Leger T, Bouget FY, Camadro JM, Lesuisse E (2012) A comparative study of iron uptake mechanisms in marine micro-algae: iron binding at the cell surface is a critical step. Plant Physiol. doi: 10.1104/pp.112.204156

Sutak R, Slapeta J, San Roman M, Camadro JM, Lesuisse E (2010) Nonreductive Iron Uptake Mechanism in the Marine Alveolate Chromera velia. Plant Physiol **154**: 991–1000

Takano J, Noguchi K, Yasumori M, Kobayashi M, Gajdos Z, Miwa K, Hayashi H, Yoneyama T, Fujiwara T (2002) Arabidopsis boron transporter for xylem loading. Nature **420**: 337–340

Takano J, Wada M, Ludewig U, Schaaf G, von Wiren N, Fujiwara T (2006) The Arabidopsis major intrinsic protein NIP5;1 is essential for efficient boron uptake and plant development under boron limitation. Plant Cell **18**: 1498–1509

Tanaka M, Fujiwara T (2008) Physiological roles and transport mechanisms of boron: perspectives from plants. Pflügers Arch - Eur J Physiol **456**: 671–677

Tanaka M, Wallace IS, Takano J, Roberts DM, Fujiwara T (2008) NIP6;1 Is a Boric Acid Channel for Preferential Transport of Boron to Growing Shoot Tissues in Arabidopsis. Plant Cell **20**: 2860–2875

Tovar-Sanchez A, Sanudo-Wilhelmy SA, Garcia-Vargas M, Weaver RS, Popels LC, Hutchins DA (2003) A trace metal clean reagent to remove surface-bound iron from marine phytoplankton. Mar Chem **82**: 91–99

Trick CG, Andersen RJ, Gillam A, Harrison PJ (1983) Prorocentrin - an extracellular siderophore produced by the marine dinoflagellate Prorocentrum minimum. Science **219**: 306–308

Trikha J, Waldo GS, Lewandowski FA, Ha Y, Theil EC, Weber PC, Allewell NM (1994) Crystallization and structural analysis of bullfrog red cell L-subunit ferritins. Proteins-Struct Funct Genet **18**: 107–118

Vandenberg R, Peters J, Vanbekkum H (1994) The Structure and (local) Stability-Constants of Borate Esters of Monosacchharides and Disaccharides as Studied by B-11 and C-13 Nmr-Spectroscopy. Carbohydr Res **253**: 1–12

Warington K (1923) The effect of boric acid and borax on the broad bean and certain other plants. Ann Bot **27**: 629–672

Wasserfallen A, Huber K, Leisinger T (1995) Purification and structural characterization of a flavoprotein induced by iron limitation in Methanobacterium thermoautotrophicum Marburg. J Bacteriol **177**: 2436–2441

Whitton BA (1999) Phycology, 3rd Edition, edited by Robert Edward Lee. J Appl Phycol **11**: 598–598

Winkelmann G, Carrano CJ (1997) Transition metals in microbial metabolism. Harwood Academic Publishers, Amsterdam

Winkler H, Meyer W, Trautwein AX, Matzanke BF (1994) Mössbauer and EXAFS studies of bacterioferritin fromStreptomyces olivaceus. Hyperfine Interact **91**: 841–846

Yau SK, Nachit MM, Hamblin J, Ryan J (1995) Phenotypic variation in boron-toxicity tolerance at seedling stage in durum wheat (Triticum durum). Euphytica **83**: 185–191